Modeling and Simulation of Closed Low-Pressure Adsorbers for Thermal Energy Storage

A thesis accepted by the Faculty of Energy-, Process- and Bio-Engineering
of the University of Stuttgart to fulfill the requirements
for the degree of Doctor of Engineering Sciences (Dr.-Ing.)

by

Micha Schäfer

born in Chennai, India

Main referee:	Prof. Dr. rer. nat. André Thess
Co-referee:	apl. Prof. Dr.-Ing. Holger Class
Date of oral examination:	25.04.2019

Institute for Building Energetics, Thermotechnology and Energy Storage
of the University of Stuttgart

2019

Erklärung

Hiermit versichere ich, Micha Schäfer, die vorliegende Arbeit ohne Hilfe Dritter und nur mit den angegebenen Quellen und Hilfsmitteln angefertigt zu haben. Alle Stellen, die Quellen entnommen wurden, sind als solche kenntlich gemacht worden. Diese Arbeit hat in gleicher oder ähnlicher Form noch keiner Prüfungsbehörde vorgelegen.
In der abgegebenen Arbeit stimmen die schriftliche und elektronische Fassung überein.

Vorwort

Diese Arbeit entstand zu 87% am Institut für Energiespeicherung sowie zu 13% am Institut für Gebäudeenergetik, Thermotechnik und Energiespeicherung der Universität Stuttgart.[1]

Mein großer Dank gilt Herrn Prof. Dr. André Thess für die Möglichkeit zur Promotion am Institut und die Übernahme des Hauptberichts. Insbesondere bedanke ich mich für das hohe Maß an Freiheit in meiner Forschung sowie für die Einbindung in Lehre und Institutsentwicklung.

Mein großer Dank gilt auch Herrn Prof. Dr. Holger Class für die Übernahme des Mitberichts.

Meinem Kollegen Herrn Mohammad Farahani möchte ich für das anhaltende Interesse und die Diskussionsbereitschaft in den vergangenen Jahren danken.
Meiner Kollegin Frau Hülya Yurttas danke ich für die stets gute Atmosphäre am Institut.

Bei meinen Kollegen und Kolleginnen am DLR bedanke ich mich für die Möglichkeit zur Teilnahme am Peer-Mentoring und Doktorandenseminar sowie für das Interesse am Fortschritt meiner Arbeit.

Besonders bedanken möchte ich mich bei den Herren Martin Karcher, Julian Vogel und Umar Khan für die Durchsicht von Teilen der Arbeit.

Neben dem fachlichen Dank gilt mein tiefer Dank meinen Eltern und meinen Geschwistern.
Und mein herzlichster Dank gilt meiner geliebten Anni!

[1] Monatsanteil entsprechend 44 Monate am Institut für Energiespeicherung und 6,5 Monate am Institut für Gebäudeenergetik, Thermotechnik und Energiespeicherung im Anschluss an die Institutsfusion am 1. Juli 2018.

Zusammenfassung

Geschlossene Niederdruck-Adsorptionssysteme können zur thermischen Energiespeicherung eingesetzt werden. Ihr Betriebsverhalten ist durch die Stoff- und Wärmetransportprozesse im Adsorber bestimmt. Folglich sind genaue Kenntnisse über diese Transportprozesse für die Weiterentwicklung der Speicher erforderlich. Die vorliegende Arbeit leistet hierzu einen Beitrag, indem detaillierte Modelle für geschlossenen Niederdruck-Adsorber bereitgestellt und Simulationen über einen weiten Bereich an Parametern und Konfigurationen durchführt werden.

Der Fokus der Arbeit liegt auf größeren Adsorbern (Länge $L = 0.1 \ldots 1\,\mathrm{m}$) sowie auf dem Entladeprozess. Als Adsorptionspaar wird binderfreier Zeolith 13X mit Wasser untersucht. Die Modellentwicklung erfolgt schrittweise von der Poren- bis zur Speicherskala. Zur numerischen Lösung der Modelle wird die Finite-Differenzen-Methode implementiert. Simulationen werden für definierte Referenzfälle sowie über einen weiten Bereich an Geometrie- und Prozessparametern durchgeführt. Die Referenzfälle werden detailliert analysiert, um ein besseres Verständnis der Transportprozesse zu erlangen. Des Weiteren werden die Ergebnisse bezüglich zwei besonderer Modellierungsaspekte analysiert: den Gleichgewichtsannahmen und den Verdünnungseffekten (z. B. Gleitströmungseffekt). In Bezug auf die Anwendung wird das Entladeverhalten anhand der thermischen Leistung und eines definierten Entladewirkungsgrads analysiert. Sowohl die Adsorber- als auch die Adsorbenskonfiguration werden variiert. Zudem wird der Einfluss der Entladebedingungen evaluiert. Die Arbeit schließt mit der Untersuchung eines beispielhaften Beladeprozesses.

Die detaillierte Analyse der Referenzfälle zeigt, dass die Stoff-, Wärme- und Adsorptionsprozesse stark gekoppelt sind und nur unter Berücksichtigung ihrer Wechselwirkung verstanden werden können. Für eindimensionale Adsorberkonfigurationen (Stoff- und Wärmetransport erfolgen in dieselbe Richtung) wird der Entladeprozess im Allgemeinen durch den Wärmetransport limitiert. Diese Limitierung hat eine unzureichende thermisches Leistung sowie ungeeignete Entladedauern von bis zu einem Jahr zur Folge. Demgegenüber kann der Entladeprozess in zweidimensionalen Adsorberkonfigurationen (Stoff- und Wärmetransport erfolgen senkrecht zu einander) durch den Stofftransport, den Wärmetransport oder die Adsorption limitiert sein. Die Limitierung hängt von der Konfiguration des Adsorbers und Adsorbens ab. Ferner ermöglichen zweidimensionalen Adsorberkonfigurationen die Realisierung ausreichender thermischer Leistung.

Bezüglich der analysierten Modellierungsaspekte zeigen die Ergebnisse, dass die Annahme einer gleichförmigen Druckverteilung nur für eindimensionale Adsorberkonfigurationen anwendbar ist. Demgegenüber lassen sich im Allgemeinen keine Gleichgewichtsannahmen für zweidimensionale Adsorberkonfigurationen anwenden. Allerdings ist es im Falle von pulverförmigem Adsorbens immer zulässig, lokales Adsorptionsgleichgewicht anzunehmen. Hinsichtlich der Verdünnungseffekte zeigt sich, dass der Gleitströmungseffekt für zweidimensionale Adsorberkonfigurationen mit Wabenkörper und Granulat von kleinem Kanal- bzw. Partikeldurchmesser ($d_{\mathrm{c/p}} \leq 1\,\mathrm{mm}$) relevant ist. Im Falle von pulverförmigem Adsorbens ist die Reduktion der effektiven Wärmeleitfähigkeit durch den Verdünnungseffekt relevant.

In Bezug auf die Anwendung zeigen die Ergebnisse, dass die volumetrische thermische Leistung im Allgemeinen mit zunehmender Länge des Adsorbers abnimmt. Ferner sinkt die Leistung mit zunehmendem Abstand zwischen den parallelen Wärmeübertragerblechen. Die Analyse der Adsorbenskonfiguration in zweidimensionalen Adsorberkonfigurationen ergibt, dass die volumetrische thermische Leistung durch Variation des Kanals- bzw. Partikeldurchmessers optimiert werden kann. Interessanterweise sind die optimalen Durchmesser für die Spitzenleistung und die mittlere Leistung nicht identisch. Des Weiteren zeigt sich, dass der Endladewirkungsgrad stark von den Entladebedingungen abhängt. Im Allgemeinen nimmt der Entladewirkungsgrad mit steigender Entladetemperatur ab. In ähnlicher Weise nimmt der Entladewirkungsgrad mit zunehmendem Volumenstrom des Wärmeträgerfluids ab. Die abschließende Analyse eines beispielhaften Beladeprozesses ergibt, dass der Druck im Adsorber aufgrund der Desorption signifikant ansteigen kann ($> 50\%$).

Abstract

Closed low-pressure adsorption systems can be applied for thermal energy storage. Their performance is determined by the mass and heat transport processes in the adsorber. Therefore, thorough knowledge of these transport processes is required for further storage development. The present thesis contributes to this by providing detailed models of closed low-pressure adsorbers and by conducting simulations over a broad range of parameters and configurations.

The focus is on adsorbers of larger scale (length $L = 0.1 \ldots 1\,\mathrm{m}$) and on the discharging process. As the adsorption pair, binderless zeolite 13X with water is examined. The models are developed in a stepwise manner from pore to storage scale. The Finite-Difference-Method is implemented to numerically solve the models. Simulations are conducted for defined reference cases as well as over a broad range of geometric and process parameters. The reference cases are analyzed in detail to gain a better understanding of the transport processes. Furthermore, the results are analyzed with respect to two particular modeling aspects: equilibrium assumptions and rarefaction effects (e. g. slip effect). With respect to the application, the discharging performance is analyzed in terms of thermal power and a defined discharging degree. Both the adsorber and the adsorbent configurations are varied. In addition, the effect of the discharging conditions is evaluated. Finally, one exemplary charging process is examined.

The detailed analysis of the reference cases reveals that the mass and heat transport and the adsorption processes are strongly coupled and can only be understood in their interaction. For one-dimensional adsorber configurations, that is the mass and heat transport are in the same direction, the discharging process is generally limited by the heat transport. This leads to insufficient thermal power and unsuitable discharging durations of up to one year. In contrast, for two-dimensional adsorber configurations, that is the mass and heat transport are in perpendicular directions, the discharging process can be limited either by the mass or heat transport or by the adsorption. The limitation depends on the configuration of the adsorber and adsorbent. Moreover, the two-dimensional adsorber configurations can provide sufficient thermal power.

With respect to the modeling, it is found that the assumption of a uniform pressure distribution is applicable for one-dimensional adsorber configurations. In contrast, for two-dimensional configurations, no equilibrium assumptions can be applied in general. However, for powder adsorbent it is always valid to assume local adsorption equilibrium. Regarding the rarefaction effects in two-dimensional adsorber configurations with honeycombs and granules, the slip effect is relevant for small channel and particle diameters ($d_{\mathrm{c/p}} \leq 1\,\mathrm{mm}$). For adsorbers with powder adsorbent, the reduction of the effective heat conductivity due to the rarefaction effect becomes relevant.

With respect to the application, the variation of the adsorber configuration shows that the volumetric thermal power generally decreases with increasing adsorber length. Furthermore, the power decreases with increasing width between the parallel heat exchanger plates in the adsorber. Regarding the adsorbent configuration in two-dimensional adsorber configurations, it is found that the volumetric thermal power can be optimized by variation of the channel or particle diameter. Interestingly, the optima for peak and mean power do not coincide. In addition, the discharging degree is found to strongly depend on the discharging conditions in terms of discharging temperature and volume flow of the heat transfer fluid extracting the heat from the adsorber. In general, the discharging degree decreases with increasing discharging temperature. Similarly, the discharging degree decreases with increasing volume flow of the heat transfer fluid. Finally, the analysis of an exemplary charging process revealed that the pressure in the adsorber can increase significantly ($> 50\%$) due to the desorption.

Contents

Nomenclature

In the following, the applied definitions of the variables, subscripts and abbreviations are listed. For better comprehensibility, variables, which solely occur in a single formula as well as self-explanatory subscripts, are omitted here. The units are given as SI and SI derived units. For single variables, other units are used in the text and noted in brackets below.

Latin Letters		**Unit**
a	channel height	m
A	surface or cross-section area	m^2
b	channel width	m
c	specific heat capacity at constant volume	J/kg K
c_p	specific heat capacity at constant pressure	J/kg K
d	diameter	m (mm)
D	diffusivity	m^2/s
e	specific internal energy	J/kg
e_{tot}	specific total energy containing internal, kinetic and potential energy	J/kg
E_{a}	characteristic energy of adsorption in Eq. (2.39)	J/kg
f	web thickness of honeycomb	m
G_{P}	Poiseuille coefficient in Eq. (4.24)	-
G_{T}	thermal creep coefficient in Eq. (4.24)	-
h	specific enthalpy	J/kg
h_{htx}	inner gap width of heat exchanger plates	m
Δh_{a}	adsorption enthalpy	J/kg
Δh_{e}	enthalpy of vaporization	J/kg
H	plate distance	m
k_{a}	adsorption kinetics parameter	1/s
$K_{\mathrm{I},1/2}$	controller parameters	diverse
Kn	Knudsen number	-
l_{mol}	free molecular path of molecules	m
L	length of adsorber (length of mass transport path)	m
L_{char}	characteristic length of macroscopic flow domain	m
$\dot{m}$, $\dot{\boldsymbol{m}}$	mass flux	kg/m^2s
M	mass	kg
N	number (of knots)	-
n_{a}	heterogeneity parameter of adsorption in Eq. (2.39)	-
p	vapor pressure	Pa (mbar)
p_{s}	saturation pressure of vapor	Pa
p_{th}	volumetric thermal power	W/m^3

$p_{\mathrm{th,htx}}$	specific thermal power at heat exchanger surface	$\mathrm{W/m^2}$
Pe	Péclet number	-
Pr	Prandtl number	-
$\dot{q}$, $\dot{\boldsymbol{q}}$	heat flux	$\mathrm{W/m^2}$
r	radius; radial coordinate	m
$\bar{R}$	universal gas constant	$\mathrm{J/mol\,K}$
R_{s}	specific gas constant	$\mathrm{J/kg\,K}$
R_{th}	thermal resistance	K/W
Re	Reynolds number	-
t	time	s (h)
$t_{p,10}$	time required for the vapor to reach the closed end of the adsorber	s (h)
t_{tot}	total process duration (discharging duration)	s (h)
$\tilde{t}$	non-dimensional time $\tilde{t} := t/t_{\mathrm{tot}}$	-
T	temperature	K (°C)
u, $\boldsymbol{u}$	velocity	m/s
v	specific volume	$\mathrm{m^3/kg}$
$\dot{v}_{\mathrm{htf}}$	specific volume flow of heat transfer fluid through adsorber	$\mathrm{m^3/s\,m^3}$
V	volume	$\mathrm{m^3}$
W	honeycomb width and distance between parallel heat exchanger plates	m
x, y, z	Cartesian coordinates	m
X	water uptake	kg/kg
X_{eq}	water uptake at adsorption equilibrium	kg/kg
Y, $\boldsymbol{Y}$	general dependent variable	diverse

Greek Letters		**Unit**
α_{htf}	convective heat transfer coefficient of heat transfer fluid	$\mathrm{W/m^2K}$
α_{p}	empirical weighing factor for effective heat conductivity of zeolite adsorbent in Eq. (4.30)	-
α_T	thermal accommodation coefficient in Eq. (2.34)	-
β_{a}	thermal expansion coefficient of the adsorbate at 20°C	1/K
γ	aspect ratio of outer to inner channel diameters, heights or widths	m/m
Γ	relative error of the non-dimensional mass flow	%
δ	rarefaction parameter	-
ε	porosity	$\mathrm{m^3/m^3}$
ϵ	emission coefficient of thermal radiation	-
ζ_i	fitting parameters for slip Poiseuille coefficient in Eq. (4.46)	-
η_{dc}	discharging degree	%
κ, $\boldsymbol{\kappa}$	permeability (tensor)	$\mathrm{m^2}$
λ, $\boldsymbol{\lambda}$	heat conductivity (tensor)	$\mathrm{W/m\,K}$
μ	shear viscosity (of vapor)	Pa s
ξ_i	fitting parameters for thermal creep coefficient in Eq. (4.47)	-

ρ	density	kg/m^3
σ_e	volumetric energy source term	J/m^3s
σ_m	volumetric mass source term	kg/m^3s
σ_P	dimensionless slip coefficient	-
τ	tortuosity	-
$\boldsymbol{\tau}$	stress tensor	N/m^2
φ	empirical fitting parameter in ZBS model Eq. (2.37) to account for finite contact area of neighboring particles	-
Φ	Knudsen permeability correction factor	-
Ψ	Knudsen heat conductivity correction factor	-

Subscripts

0	initial state or continuum regime
a	adsorbate
b	bulk of adsorbent
av	adsorptive (vapor)
c	channel
cpl	coupling
CK	Carman-Kozeny
dc	discharge
eff	effective
f	fluid
hc	honeycomb
htf	heat transfer fluid
htx	heat exchanger
hydr	hydraulic
i	counting index
i	inner
in	in, inlet
max	maximum
min	minimum
mp	macro pore
n	normal direction
o	outer
out	out, outlet
p	particle
pb	packed bed
ref	reference state
s	saturation
v	vapor
z	zeolite (adsorbent)

Abbreviations

AMR	Adaptive Mesh Refinement
CDA	Central Difference Approximation
DSMC	Direct Simulation Monte Carlo
FDM	Finite Difference Method
GCM	General Continuum Model
HTX	Heat Exchanger
LDF	Linear Driving Force approximation
MCM	Multi Channel Model
ODE	Ordinary Differential Equation
PDE	Partial Differential Equation
PTFE	Polytetrafluoroethylene
SCM	Single Channel Model
TES	Thermal Energy Storage
ZBS	Zehner-Bauer-Schlünder model

1. Introduction

Closed low-pressure adsorption systems can be applied for thermal energy storage. Their performance is determined by the mass and heat transport processes in the adsorber. Therefore, thorough knowledge of these transport processes is required for further storage development. The present thesis contributes to this by providing detailed models of closed low-pressure adsorbers and conducting simulations over a broad range of parameters and configurations.

1.1. Motivation

The broad framework and general motivation of this thesis is the energy transition, see Fig. 1.1. The energy transition denotes the transition of the energy supply from fossil energy sources to the energy supply from renewable energy sources, e. g. [1]. Main objectives of the energy transition are: sustainability, climate neutrality, environmental conservation, human safety, independence of supply and long-term cost reduction.

The energy transition requires research and development in the fields of energy generation, energy transformation, energy transfer and last but not least in the field of energy storage [2]. The necessity to store energy follows from the fluctuation of the energy supply from renewable energy sources such as wind or solar, e. g. [3]. Due to the fluctuation, the energy supply may at one point in time exceed demand, while at another time it might not cover demand. Therefore, energy storage is essential to balance the excess energy in order to match supply and demand.

Energy storage is required for both electrical and thermal energy. With respect to electrical energy storage of large capacity, transformation and storage of the energy in thermal energy storage (TES) allows for an increase of the storage efficiency as well as for a reduction of the storage costs. Examples for such energy storage systems are adiabatic compressed air energy storage and pumped heat electrical storage, e. g. [4, 5]. Besides large-capacity electrical energy storage, TES is required for the direct storage of thermal energy in industrial and domestic applications, e. g. [6].

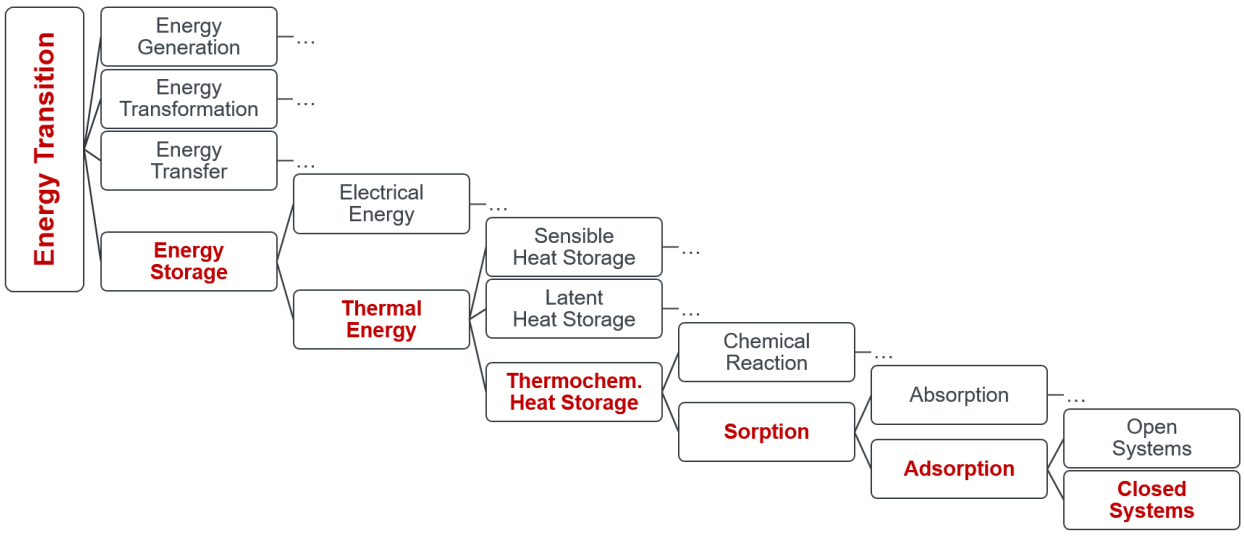

Figure 1.1.: Thematic overview: broad framework and general motivation is the energy transition.

In general, TES is distinguished into three groups by its physical storage principle: sensible, latent and thermochemical heat storage [7]. In sensible heat storage, thermal energy is stored by lifting the temperature of the storage medium. In latent heat storage, thermal energy is stored by thermally changing the phase of the storage medium. In thermochemical heat storage, thermal energy is stored by separating the chemical components of the storage medium. Specific advantages of the thermochemical heat storage in comparison with the other two groups of heat storage are the high energy storage density, the low relative thermal losses, the on-demand discharge and the possibility to utilize the thermochemical heat storage as a heat pump [8].

The group of thermochemical heat storage includes both chemical reactions as well as sorption. It should be noted that on a molecular level, sorption is not a chemical process in most cases, but the macroscopic phenomenon is similar to a chemical reaction. Sorption can be further distinguished into ab- and adsorption. While the first denotes the uptake of molecules of or in a fluid into a solid or another fluid, the latter denotes the accumulation at the surface of a solid. For TES based on adsorption, the adsorption of gas and especially of vapor is particularly important, e. g. [9].

Finally, TES based on adsorption can be distinguished by the process design into open and closed systems, e. g. [9]. In open systems, the adsorptive gas is transported by an additional carrier gas. The carrier gas is applied as the heat transfer fluid and is in direct contact with the adsorbent. As the carrier gas is often ambient air, the pressure in open systems is around 1 bar. In contrast, no additional carrier gas is required in closed systems. However, the absence of the carrier gas necessitates the integration of a heat exchanger into the adsorbent bulk. Furthermore, for closed vapor systems, the typical operating pressures are generally low: $p < 100\,\mathrm{mbar}$, e. g. [10].

As an example, consider the application of TES based on closed adsorption systems in the building sector. The distribution of the final energy consumption to different sectors in Germany for the year 2016 is shown in Fig. 1.2 (a). The figure reveals that approximately one third of the final energy consumption can be attributed to the building sector. From that share more than 90% of the energy is finally consumed as heat in the temperature range of 10 . . . 100°C. The heat demand can be further distinguished into demand for hot water (13%) and demand for heating (78%). The hot water demand fluctuates on a daily basis but is otherwise almost constant throughout the year. In contrast, the heating demand varies over the period of one year, see Fig. 1.2 (b). In theory, both heat demands can be covered from solar energy by storing the solar energy. The daily fluctuations of the hot water demand are usually buffered by hot water tanks. However, the seasonal fluctuations of the heating demand cannot be compensated by common hot water tanks in general for two reasons. First, the heating demand corresponds to large amounts of thermal energy that need to be stored, thus requiring large storage capacity. Second, the thermal energy has to be stored for a long duration, thus requiring low heat loss rate. In this context, TES based on closed adsorption might be a solution as they offer high energy storage density and are practically free of thermal losses over long storage durations, see e. g. [13].

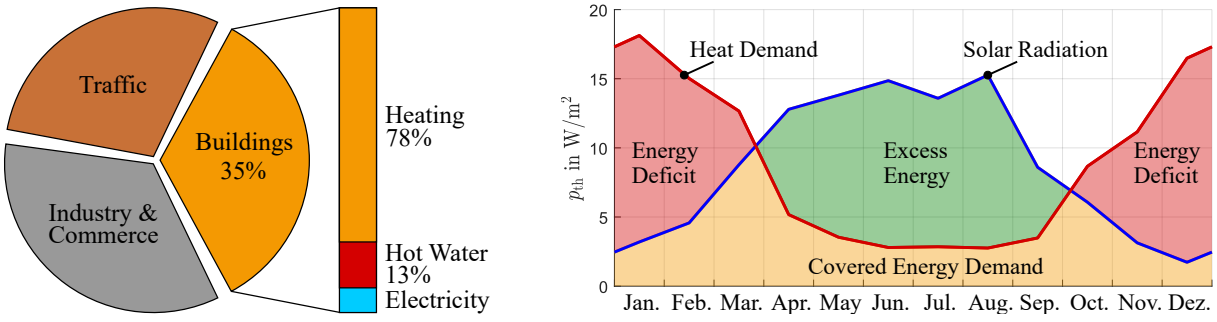

(a) Final energy consumption, data from [11].

(b) Heat demand and solar radiation, data from [12].

Figure 1.2.: Distribution of final energy consumption in Germany in 2016 and evolution of heat demand and solar radiation for an apartment building in Germany over one year.

1.2. Subject Matter

The subject matter of this thesis is closed low-pressure adsorbers for TES application. The scheme and storage principle of a closed adsorption system is shown in Fig. 1.3. The system consists of two main vessels: a water vessel with a condenser-evaporator unit and a zeolite adsorber with an internal heat exchanger. Both vessels are connected vacuum-tight via a pipe and are initially evacuated. During the charging process, heat at high temperature is supplied to the adsorber, desorbing the adsorbed water. The emerging vapor flows to the water vessel and condensates, releasing the heat of condensation at a low temperature level. Over the storage period, the two vessels are simply closed and separated by a valve. To discharge the storage, the process is reversed. The water in the water vessel is evaporated by heat at low temperature. The arising vapor flows to the adsorber where it is adsorbed, releasing the heat of adsorption at a high temperature level, compare e. g. [14]. The focus of this thesis is on the discharging process of the adsorber, see dashed box in Fig. 1.3.

Since closed low-pressure adsorbers of larger scale (length $L = 0.1 \ldots 1\,\mathrm{m}$) are mainly discussed for seasonal storage of solar energy in buildings, e. g. [15, 14, 9], the operating conditions are defined in accordance with Ref. [13]. Nevertheless, the model developed in this thesis is not limited to this application and operating conditions. During charging, heat is supplied at 180°C to the adsorber while the condenser is kept at a temperature of 17°C, corresponding to a vapor pressure of 20 mbar. Thus, at the end of the charging process, the relative water content in the adsorber is decreased to around $X = 0.1\,\mathrm{kg/kg}$. The sensible heat in the adsorber after charging is either dissipated or discharged while the valve of the adsorber is kept closed. Therefore, the remaining vapor in the adsorber is readsorbed resulting in a very low pressure in the adsorber of $0.001 \ldots 0.1\,\mathrm{mbar}$ at the beginning of the discharging process. During discharging, the evaporator temperatures lie in the range of $5 \ldots 25$°C, yielding an adsorber inlet pressure in the range of $10 \ldots 30\,\mathrm{mbar}$. For this pressure range, the maximum achievable adsorber temperatures lie in the range of $135 \ldots 160$°C. Due to the heat transport limitations in the adsorber, the effective discharging temperatures are even lower. Thus, the discharging temperature is generally lower than the charging temperature.

With respect to the adsorbent material, binderless zeolite 13X is assumed in this thesis as it is often studied in the context of domestic heating, e. g. [16, 17, 18, 13]. The zeolite adsorbent is available in three configurations: powder, granules and honeycomb, see Fig. 1.4. All three adsorbent configurations are examined in this thesis. In general, the powder is used as raw material to manufacture granules and honeycombs [19]. Therefore, it is the least expensive adsorbent

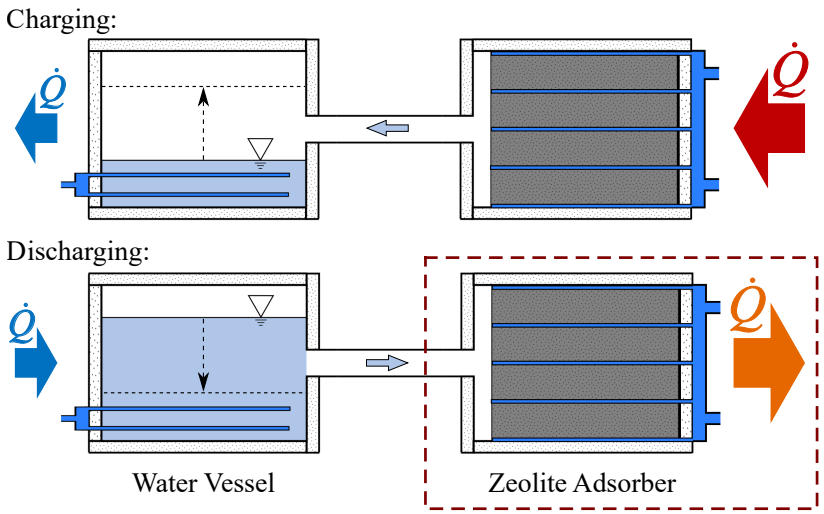

Figure 1.3.: Scheme and storage principle of a closed low-pressure adsorption system. The focus of this thesis is on the discharging process of the adsorber (dashed box).

Figure 1.4.: Examined adsorbent configurations of binderless zeolite 13X. The depicted adsorbents are manufactured by Chemiewerk Bad Köstritz GmbH, Germany.

configuration. However, granules are the most studied and applied adsorbent configuration and commercially available [10]. For the honeycomb adsorbent, lower pressure loss and thus a higher storage efficiency is predicted [20]. On the downside, honeycomb adsorbents are more expensive. Typical particle diameters of the powder and granules adsorbent lie in the range of $5 \ldots 100\,\mu$m and $0.5 \ldots 5\,$mm respectively. For the honeycombs, the channel size lies in the range of $0.5 \ldots 5\,$mm and the web thickness is in the range of $0.1 \ldots 5\,$mm.

1.3. Objectives

The main objective of this thesis is to contribute to a better understanding of the dynamic mass and heat transport as well as adsorption processes in closed low-pressure adsorbers for thermal energy storage. Moreover, the thesis aims to provide insight into the effect of the adsorber configuration (main dimensions, vapor supply and heat extraction) as well as the adsorbent configuration (macroscopic adsorbent dimensions and structure, see Fig. 1.4). For this purpose, a stepwise development of three adsorber models from pore to storage scale is conducted. The stepwise model development allows for an accurate description of the underlying physical processes. Special emphasis is put on the rarefaction effects (e. g. slip effect) on the mass and heat transport resulting from the low pressure. The three developed models are denoted as Single Channel Model (SCM), Multi Channel Model (MCM) and General Continuum Model (GCM). While the SCM and MCM are only applicable to honeycomb adsorbers, the GCM can be applied for all three examined adsorbent configurations. The three models are numerically implemented in Matlab and extensive simulation studies are carried out over a broad range of parameters and configurations.
More specifically, the following questions regarding the modeling and the application are analyzed:

Modeling:

- Is it valid to apply equilibrium assumptions (e. g. uniform pressure assumption)?
- Is it required to take rarefaction effects (e. g. slip effect) due to the low pressure into account?

Application:

- How does the adsorber configuration (e. g. adsorber length) influence the discharging?
- How does the adsorbent configuration (e. g. particle diameter) influence the discharging?
- How does the discharging condition (e. g. discharging temperature) influence the discharging?

With respect to the application, the discharging performance is evaluated by the important parameters of volumetric thermal power and a defined discharging degree.

The thesis is organized as follows: First, an overview on the fundamentals and the state of research is given in chapters 2 and 3. Then, the three models SCM, MCM and GCM are described in detail in Chapter 4. A compact discussion on the numerical implementation follows in Chapter 5. Subsequently, the simulation results are presented and discussed in Chapter 6. Finally, the thesis is concluded with a summary and outlook in Chapter 7.

2. Fundamentals

2.1. Conservation and Continuity

Conservation is a fundamental physical principle and mathematically expressed by the conservation laws, e. g. [21]. The general conservation law states that a physical quantity in an isolated system does not change over time. However, as fluxes of the physical quantity over the system boundary occur, the physical quantity can change. In addition, changes of the physical quantity can result from internal sources within the system. This is described by the continuity equation, e. g. [22]. For a fixed volume V of the system the general continuity equation reads

$$\frac{\partial}{\partial t}\int\limits_V \phi \,\mathrm{d}V = -\oint\limits_A (\boldsymbol{j}\cdot\boldsymbol{n})\,\mathrm{d}A + \int\limits_V \sigma \,\mathrm{d}V, \tag{2.1}$$

where ϕ denotes the volumetric physical quantity, $\boldsymbol{j}$ the flux vector of the physical quantity and $\boldsymbol{n}$ the normal unit vector of the system boundary surface A. Thus, $(\boldsymbol{j}\cdot\boldsymbol{n})$ denotes the flux of the physical quantity over the system boundary. The volumetric source of the physical quantity in the volume of the system is given by σ.

For material systems, the physical quantity can be determined from the mass density ρ and the specific physical quantity per unit mass ϕ_m by $\phi = \rho\phi_m$. Furthermore, part of the fluxes of the physical quantity can result from the movement of the matter, and thus are connected to the mass flux $\dot{\boldsymbol{m}}$. Considering an infinite small control volume as the system volume and applying Leibniz integral rule and Gauss's flux theorem, the continuity Eq. (2.1) takes the local differential form

$$\frac{\partial}{\partial t}\Big(\rho\phi_m\Big) = -\nabla\cdot\Big(\dot{\boldsymbol{m}}\phi_m + \boldsymbol{j}^*\Big) + \sigma, \tag{2.2}$$

where ∇ denotes the nabla operator and $\boldsymbol{j}^*$ refers to the fluxes independent of the mass flux.

The general continuity Eq. (2.2) can be applied to different physical quantities. In the field of fluid- and thermodynamics relevant physical quantities are the mass, the linear and angular momentum, the energy, the chemical potential and the entropy, e. g. [23, 24]. In this context, the continuity equations are also referred to as balance equations.

Mass Balance Equation

Applying the continuity Eq. (2.2) to the mass ($\phi_m \equiv 1$, $\boldsymbol{j}^* \equiv 0$), the mass balance equation

$$\frac{\partial\rho}{\partial t} = -\nabla\cdot\dot{\boldsymbol{m}} + \sigma_m \tag{2.3}$$

is derived. Note that in single-phase systems without chemical reaction or phase transition no mass source term σ_m exists, that is $\sigma_m \equiv 0$.

For the special case of a porous medium with one fluid phase (index f) and one solid phase (index s) the mass balance equation of the fluid phase reads

$$\frac{\partial}{\partial t}\Big(\varepsilon\rho_\mathrm{f}\Big) = -\nabla\cdot\dot{\boldsymbol{m}}_\mathrm{f} + \sigma_{m,\mathrm{s,f}}, \tag{2.4}$$

where ε denotes the porosity, which is defined as the volume fraction of the fluid phase

$$\varepsilon := \frac{\mathrm{d}V_\mathrm{f}}{\mathrm{d}V}. \tag{2.5}$$

Momentum Balance Equation

Applying the continuity Eq. (2.2) to the linear momentum ($\phi_m = \boldsymbol{u}$, $\boldsymbol{j}^* = -\boldsymbol{\tau}$) yields the momentum balance equation (also referred to as the Cauchy momentum equation)

$$\frac{\partial}{\partial t}\Big(\rho \boldsymbol{u}\Big) = -\nabla \cdot \Big(\dot{\boldsymbol{m}} \otimes \boldsymbol{u} - \boldsymbol{\tau}\Big) + \boldsymbol{\sigma}_u, \tag{2.6}$$

where $\boldsymbol{u}$ denotes the velocity and $\boldsymbol{\tau}$ the stress tensor, describing the forces acting on the boundary surface of the control volume. The source term $\boldsymbol{\sigma}_u$ includes internal forces, such as the gravity.

For the special case of a compressible, viscous Newton fluid the stress tensor can be specified and the momentum balance Eq. (2.6) yields the Navier-Stokes equation

$$\frac{\partial}{\partial t}\Big(\rho \boldsymbol{u}\Big) + \nabla \cdot \Big(\dot{\boldsymbol{m}} \otimes \boldsymbol{u}\Big) = -\nabla p + \nabla\Big(\zeta \nabla \cdot \boldsymbol{u}\Big) + 2\nabla \cdot \left(\mu \left(\frac{1}{2}\left(\nabla \boldsymbol{u} + \nabla \boldsymbol{u}^T\right) - \frac{1}{3}\left(\nabla \cdot \boldsymbol{u}\right)\boldsymbol{I}\right)\right) + \rho \boldsymbol{f}. \tag{2.7}$$

Here, ζ denotes the volume viscosity, $\boldsymbol{I}$ the identity matrix and $\boldsymbol{f}$ the internal forces. Further, p denotes the pressure and μ the shear viscosity. The mass flux is related to the velocity by $\dot{\boldsymbol{m}} = \rho \boldsymbol{u}$.

Under the assumption of a constant and uniform fluid density ($\nabla \cdot \boldsymbol{u} \equiv 0$), the Navier-Stokes Eq. (2.7) can be simplified. Moreover, assuming creeping flow, that is low Reynolds number $Re \ll 1$, it can be shown that the inertia forces (left side of Eq. (2.7)) are negligible. Finally, neglecting the internal forces and assuming a constant shear viscosity, the derived equation reads

$$0 = -\nabla p + \mu \nabla^2 \boldsymbol{u}, \tag{2.8}$$

where ∇^2 denotes the Laplace operator. The equation is also referred to as Stokes flow equation.

Energy Balance Equation

Applying the continuity Eq. (2.2) to the energy ($\phi_m = e_{\text{tot}}$, $\boldsymbol{j}^* \equiv \dot{\boldsymbol{q}} - \boldsymbol{u} \cdot \boldsymbol{\tau}$) yields the energy balance equation

$$\frac{\partial}{\partial t}\Big(\rho e_{\text{tot}}\Big) = -\nabla \cdot \Big(\dot{\boldsymbol{m}} e_{\text{tot}} + \dot{\boldsymbol{q}} - \boldsymbol{u} \cdot \boldsymbol{\tau}\Big) + \sigma_e, \tag{2.9}$$

where e_{tot} denotes the total energy, containing the internal energy as well as the kinetic and potential energy. Further, $\dot{\boldsymbol{q}}$ denotes the energy transported by thermal conduction, while $\boldsymbol{u} \cdot \boldsymbol{\tau}$ refers to the power of the forces, acting on the boundary surface of the control volume. The internal energy sources are given by σ_e and account for example for absorbed thermal radiation.

Neglecting the kinetic and potential energy, the total energy reduces to the internal energy e. Furthermore, neglecting the viscous dissipation, the stress tensor reduces to $\boldsymbol{\tau} = -p\boldsymbol{I}$. Finally, with the definition of the enthalpy $h := e + p/\rho$, the energy balance Eq. (2.9) can be simplified to

$$\frac{\partial}{\partial t}\Big(\rho e\Big) = -\nabla \cdot \Big(\dot{\boldsymbol{m}} h + \dot{\boldsymbol{q}}\Big) + \sigma_e. \tag{2.10}$$

For both an ideal gas and an incompressible medium, the internal energy is related to the specific heat capacity at constant volume c by the reduced caloric state equation $\mathrm{d}e = c\,\mathrm{d}T$. Similarly, the enthalpy is related to the specific heat capacity at constant pressure c_p by $\mathrm{d}h = c_p\,\mathrm{d}T$. Thus, the internal energy and the enthalpy can be determined by integration

$$e = \int_{T_{\text{ref}}}^{T} c\left(\tilde{T}\right)\mathrm{d}\tilde{T} + e_{\text{ref}}, \qquad h = \int_{T_{\text{ref}}}^{T} c_p\left(\tilde{T}\right)\mathrm{d}\tilde{T} + h_{\text{ref}}, \tag{2.11}$$

where e_{ref} and h_{ref} denote the internal energy and the enthalpy at the reference temperature T_{ref}.

Finally, for a constant density, the simplified energy balance Eq. (2.10) with Eq. (2.11) yields

$$\rho c \frac{\partial T}{\partial t} = -\dot{\boldsymbol{m}} c_p \cdot \nabla T - \nabla \cdot \dot{\boldsymbol{q}} + \sigma_e. \tag{2.12}$$

Here, the first term on the right side corresponds to the convective heat transport.

2.2. Transport Phenomena

Systems described by the mass and energy balance Eq. (2.3) and (2.10) need to be closed by transport equations for the mass and heat flux $\dot{\boldsymbol{m}}$ and $\dot{\boldsymbol{q}}$. In this thesis, "transport equations" solely denotes the equations for mass and heat flux and does not refer to balance or convection-diffusion equations. An overview and extensive discussion of transport phenomena is given in [25].

2.2.1. Mass Transport

The mass flux is related to the velocity by

$$\dot{\boldsymbol{m}} = \rho \boldsymbol{u}. \tag{2.13}$$

Therefore, the mass flux can be determined by solving the momentum balance Eq. (2.6) for the velocity. However, as the momentum balance equation is a non-linear partial differential equation, it is difficult or even impossible to derive analytical solutions. Furthermore, the momentum balance equation is generally coupled with the mass and energy balance equation. Thus, the single balance equations of the closed system have to be solved together.

Nevertheless, for particular simple or simplified cases the momentum balance equation can be solved independently as well as analytically. In the previous section, the general momentum balance Eq. (2.6) was first specified for a compressible Newton fluid and then further simplified for creeping flow ($Re \ll 1$), assuming constant density and viscosity. Although the derived Stokes flow Eq. (2.8) is linear, further dimension reduction is required to allow for analytical solutions.

Circular Channel Flow

One particular simple but relevant case of reduced dimension is given by the axially symmetric flow in a straight pipe or circular channel respectively with a constant channel diameter. This flow is referred to as Hagen-Poiseuille flow, e. g. [23]. For the Hagen-Poiseuille flow, the dimensionally reduced Stokes flow equation in cylindrical coordinates reads

$$-\frac{\partial p}{\partial z} + \mu \frac{1}{r} \frac{\partial}{\partial r} \left(r \frac{\partial u_z}{\partial r} \right) = 0, \tag{2.14}$$

where r denotes the radial direction and u_z refers to the velocity component in flow direction.

Applying the common no-slip boundary condition at the channel wall $u_z(r = r_\mathrm{c}) = 0$ and the symmetry boundary condition at the symmetry line $\partial_r u_z(r = 0) = 0$, the well-known parabolic velocity profile is derived, see Fig. 2.1 (a). The solution reads

$$u_z(r) = -\frac{r_\mathrm{c}^2 - r^2}{4\mu} \frac{\partial p}{\partial z}, \tag{2.15}$$

where r_c denotes the radius of the circular channel. With this, the mean mass flux can be determined by averaging the velocity over the channel cross-section, yielding

$$\dot{m}_z = -\rho \frac{d_\mathrm{c}^2}{32\mu} \frac{\partial p}{\partial z}, \tag{2.16}$$

where $d_\mathrm{c} = 2r_\mathrm{c}$ denotes the diameter of the circular channel.

The derived solutions (2.15) and (2.16) are strictly valid only for flows with constant fluid density. However, for channel flows with large aspect ratio $L/d_\mathrm{c} \gg 1$ it can be shown that the solution also applies to flows of compressible fluids [26]. Assuming the compressible fluid as an ideal gas with the specific gas constant R_s, the ideal gas law

$$\rho = \frac{p}{R_\mathrm{s} T} \tag{2.17}$$

can be applied to Eq. (2.16). This yields the differential equation for the longitudinal pressure distribution in the channel

$$\dot{m}_z = -\frac{p}{R_s T}\frac{d_c^2}{32\mu}\frac{\partial p}{\partial z}. \tag{2.18}$$

For a stationary ($\dot{m}_z$ = const.) and isothermal (T_s = const., μ = const.) flow through a circular channel of length L with a defined inlet and outlet pressure p_{in} and p_{out} the differential equation (2.18) can be integrated, yielding

$$p(z) = \sqrt{p_{in}^2 - \left(R_s T \frac{32\mu}{d_c^2}\dot{m}_z\right) z} \qquad \text{with } \dot{m}_z = -\frac{d_c^2}{R_s T 32\mu}\frac{p_{out}^2 - p_{in}^2}{L} = -2\bar{\rho}\frac{d_c^2}{32\mu}\frac{p_{out} - p_{in}}{L}, \tag{2.19}$$

where $\bar{\rho}$ denotes the arithmetic mean of the gas density at the in- and outlet. Substituting the mass flux into the pressure solution leads to

$$p(z) = \sqrt{p_{in}^2 + \left(\frac{p_{out}^2 - p_{in}^2}{L}\right) z}. \tag{2.20}$$

The result reveals that for this particular channel flow case, the pressure distribution along the channel is independent from the channel diameter, fluid properties and temperature. The pressure curve $p(z)$ for two different aspect ratios of the in- and outlet pressure p_{in}/p_{out} is shown in Fig. 2.1 (b). The figure shows that the pressure curves deviate increasingly from the linear pressure curves of the incompressible flow with increasing aspect ratio of the in- and outlet pressure. Moreover, the pressure curves for the flow of the compressible ideal gas are of concave shape, e. g. [27]. As the pressure decreases along the channel, the vapor density also decreases, and thus, according to Eq. (2.16), an increased pressure gradient is required to remain a constant mass flux.

The discussion so far has been limited to the flow of a continuum. The fluid can be considered as a continuum as long as the molecular fluctuations are negligible on the macroscopic length scale of the examined flow problem, e. g. [28]. However, with decreasing fluid density as well as with decreasing macroscopic length scale, the fluid can no longer be considered as a continuum. This effect is also referred to as rarefaction effect. The divergence from the continuum properties is characterized by the non-dimensional Knudsen number Kn. The Knudsen number is defined as the ratio of the free molecular path l_{mol} and the characteristic length of macroscopic flow domain L_{char}. For the discussed flow through a circular channel, the characteristic length is usually defined

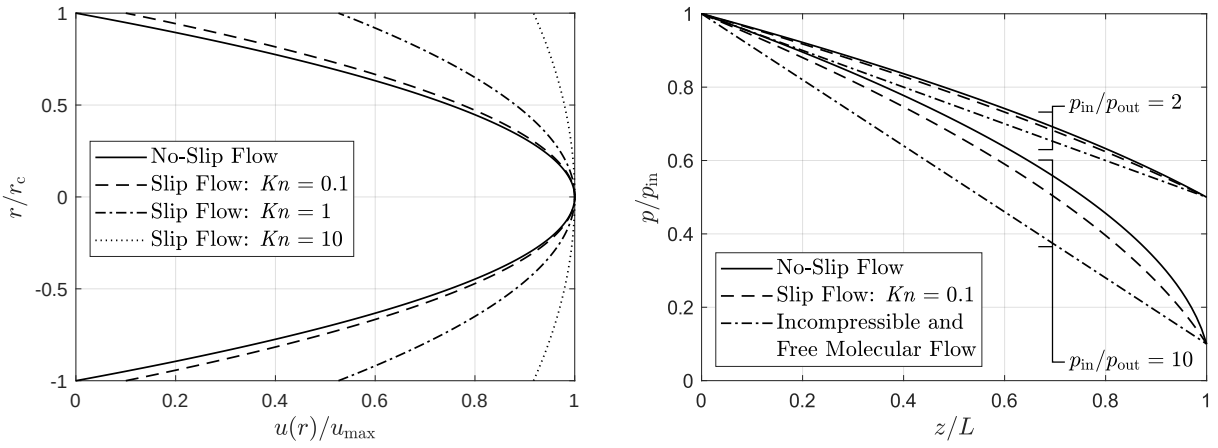

(a) Radial velocity distribution.

(b) Longitudinal pressure distribution.

Figure 2.1.: Velocity and pressure distribution in a circular channel for creeping flow ($Re \ll 1$).

as the channel radius $L_{\mathrm{char}} := r_{\mathrm{c}} = d_{\mathrm{c}}/2$. Relating the free molecular path to the macroscopic fluid properties, the Knudsen number can be calculated from

$$Kn := \frac{l_{\mathrm{mol}}}{L_{\mathrm{char}}} \approx \sqrt{\frac{\pi}{2}} \frac{2\mu}{d_{\mathrm{c}}} \frac{\sqrt{R_{\mathrm{s}} T}}{p}. \tag{2.21}$$

With the Knudsen number, different flow regimes are defined, see Tab. 2.1. For $Kn \leq 0.01$ the continuum assumption together with the no-slip boundary condition is valid. In the subsequent Knudsen range of $0.01 \leq Kn \leq 0.1$ the continuum assumption holds up, but the boundary condition has to be modified. In this so-called slip regime, the boundary condition allows for a slip velocity. In the Knudsen range of $0.1 \leq Kn \leq 10$, the flow transits from a continuum flow to a free molecular flow. With respect to the velocity profile, the profile transforms from a parabolic profile to a uniform velocity distribution over the channel cross-section. Finally, for $10 \leq Kn$ the interactions between the fluid molecules become negligible and the flow is primarily determined by the interaction of the fluid molecules with the boundaries.

Considering the circular channel flow again, it is possible to derive an analytical solution for the slip regime, e. g. [29]. Applying Maxwell's first-order slip boundary condition [30], the slip velocity u_{slip} at the channel wall in the slip regime reads

$$u_z(r = r_{\mathrm{c}}) = u_{\mathrm{slip}} = \frac{d_{\mathrm{c}} \sigma_{\mathrm{P}}}{\sqrt{\pi}} Kn \left. \frac{\partial u_z}{\partial r} \right|_{r=r_{\mathrm{c}}}, \tag{2.22}$$

where σ_{P} denotes the dimensionless slip coefficient. The slip coefficient depends on the molecular accommodation at the wall and is well approximated by $\sigma_{\mathrm{P}} = 0.985 \approx 1$.

Applying the slip boundary condition (2.22) to the Stokes flow equation of a circular channel (2.14) yields the velocity solution

$$u_z(r) = -\left(\frac{r_{\mathrm{c}}^2 - r^2}{4\mu} + \frac{r_{\mathrm{c}}^2 \sigma_{\mathrm{P}}}{2\sqrt{\pi}} Kn \right) \frac{\partial p}{\partial z}. \tag{2.23}$$

The corresponding velocity profile is shown for different values of the Knudsen number in Fig. 2.1 (a). For $Kn \to 0$, the solution converges to the Hagen-Poiseuille solution (2.15). Thus, at the beginning of the slip regime with $Kn = 0.01$, the solution is almost identical with the no-slip solution. At the end of the slip regime with $Kn = 0.1$, the slip solution predicts a slip velocity at the boundary of 10% of the maximum velocity. Additionally, the velocity profiles of the slip solution for higher values of the Knudsen number are depicted. While the slip solution is not strictly valid for $0.1 \leq Kn$, it still gives a representation of the velocity profile change with increasing Knudsen number.

Averaging the velocity over the channel cross-section, the mean mass flux can be determined to

$$\dot{m}_z = -\rho \frac{d_{\mathrm{c}}^2}{32\mu} \left(1 + \frac{8\sigma_{\mathrm{P}}}{\sqrt{\pi}} Kn \right) \frac{\partial p}{\partial z}. \tag{2.24}$$

Hence, the mean mass flux results from the superposition of the mean mass flux of the no-slip solution and the mass flux induced by the velocity slip.

Table 2.1.: Flow regimes defined by the Knudsen number according to Eq. (2.21).

Regime	Kn-Range	Characteristics
no-slip	$Kn \leq 0.01$	continuum flow with no-slip boundary condition
slip	$0.01 \leq Kn \leq 0.1$	continuum flow with slip boundary condition
transition	$0.1 \leq Kn \leq 10$	transitional flow with decreasing continuum properties
molecular	$10 \leq Kn$	free molecular flow with negligible molecular interaction

Again, as described for the continuum flow, Eq. (2.24) can be integrated for a stationary ($\dot{m}_z = \text{const.}$) and isothermal ($T_\text{s} = \text{const.}$, $\mu = \text{const.}$) flow of an ideal gas through a circular channel of length L with a defined inlet and outlet pressure p_in and p_out . This yields

$$p(z) = \sqrt{p_\text{in}^2 + \left(\frac{p_\text{out}^2 - p_\text{in}^2}{L}\right) z + p_\text{in}^2 \frac{8\sigma_\text{P}}{\sqrt{\pi}} Kn_\text{in} \left(\frac{p_\text{out} - p_\text{in}}{p_\text{in}} \frac{z}{L} + \frac{2\sigma_\text{P}}{\sqrt{\pi}} Kn_\text{in} + 1\right)} - \frac{1}{2} \frac{8\sigma_\text{P}}{\sqrt{\pi}} Kn_\text{in} p_\text{in}. \quad (2.25)$$

The first part of the result is identical to the solution of the continuum no-slip flow, see Eq. (2.20). The other terms result from the slip effect and vanish for $Kn_\text{in} \to 0$. The pressure curve $p(z)$ for an inlet Knudsen number of $Kn_\text{in} = 0.1$ and two different aspect ratios of the in- and outlet pressure p_in/p_out is shown in Fig. 2.1 (b). The slip effect reduces the convexity of the pressure curve. For $Kn \to \infty$ the pressure curve becomes linear, as is the case for the flow of a incompressible fluid.

Porous Media Flow

The mass transport in a porous medium is briefly described in the following section. For laminar groundwater flow H. Darcy empirically found the well-known Darcy's law [31]

$$\dot{\boldsymbol{m}} = -\boldsymbol{\kappa} \frac{\rho}{\mu} \nabla p, \quad (2.26)$$

where $\boldsymbol{\kappa}$ denotes the permeability tensor. Nevertheless, it is possible to derive Darcy's law analytically through volume averaging and homogenization of the momentum balance equations on the pore scale, e. g. [32, 33]. Darcy's law is valid for laminar flow with $Re \leq 1$ of a viscous Newton fluid. Comparison of Darcy's law (2.26) with the mean mass flux determined for a creeping flow in a circular channel by Eq. (2.16) reveals the same mathematical structure. This indicates that the permeability solely depends on the geometric structure of the porous medium. Furthermore, the local applicability of the Poiseuille Eq. (2.16) to channel flows with large aspect ratio $L/d_\text{c} \gg 1$ has been proved [26]. Thus, it can be assumed that Darcy's law can also be applied locally for the creeping flow of a compressible fluid as long as the aspect ratio of the length of the porous domain to the hydraulic diameter of the porous medium d_hydr is large: $L/d_\text{hydr} \gg 1$.

For a packed bed of spherical particles J. Kozeny and C. Carman developed an equation for the permeability by applying a simple model of the porous medium [34, 35]. The interstitial pore space is considered as a parallel arrangement of straight circular channels. With this, the permeability of a packed bed of spheres is determined to

$$\kappa_\text{CK} = \frac{1}{36\phi} \frac{\varepsilon^3}{\tau^2 (1-\varepsilon)^2} d_\text{p}^2 = \frac{1}{180} \frac{\varepsilon^3}{(1-\varepsilon)^2} d_\text{p}^2. \quad (2.27)$$

Here, ϕ is an empirical fitting parameter. Further, τ denotes the tortuosity. The tortuosity takes into account that the fluid cannot flow through the porous medium of length L on a straight path but has to travel a longer path τL. For packed bed of spheres, the tortuosity is well approximated by $\tau = \sqrt{2}$ and the empirical fitting parameter is determined to $\phi = 2.5$, e. g. [33]

Based on the fundamentals of slip flow in a circular channel described above, L. J. Klinkenberg derived a permeability correction factor for creeping flow through a porous medium in the slip flow regime [36]. With this, Darcy's law (2.26) can be rewritten as

$$\dot{\boldsymbol{m}} = -\boldsymbol{\kappa} \left(1 + \frac{b}{p}\right) \frac{\rho}{\mu} \nabla p. \quad (2.28)$$

Here, b is a semi-empirical parameter which was determined experimentally by L. J. Klinkenberg. However, since the Knudsen number is inverse to the pressure, b/p is proportional to the Knudsen number. Comparison of the modified Darcy's law with the Klinkenberg permeability correction factor (2.28) to the mean mass flux determined for a creeping flow in the slip regime in a circular channel, see Eq. (2.24), reveals the same mathematical structure.

2.2.2. Heat Transport

The heat flux $\dot{\boldsymbol{q}}$ in the energy balance Eq. (2.9) results from thermal conduction. Thermal conduction is based on molecular transport mechanisms such as molecular vibrations and collisions. On the macroscopic scale thermal conduction can be described by Fourier's law [37]

$$\dot{\boldsymbol{q}} = -\boldsymbol{\lambda} \cdot \nabla T, \tag{2.29}$$

where $\boldsymbol{\lambda}$ denotes the thermal or heat conductivity tensor. Comparison with the channel flow Eq. (2.16) and Darcy's law (2.26) reveals the same mathematically structure. In contrast, in this local form of Fourier's law, the heat conductivity solely depends on the material and not on geometry parameters such as the channel or particle diameter.

For the special case of a stationary, resting medium ($\dot{\boldsymbol{m}} \equiv 0$) with constant heat conductivity, the energy balance Eq. (2.10) reduces with Fourier's law (2.29) to the heat equation

$$0 = -\boldsymbol{\lambda} \nabla^2 T + \sigma_e. \tag{2.30}$$

Note that the heat Eq. (2.30) has the same mathematical structure as the Stokes flow Eq. (2.8). Thus, reduction of the dimension allows for a straightforward analytical solution.

Parallel Plate Conduction

One particular simple but relevant case of reduced dimension is given by the thermal conduction between two parallel plates with constant, uniform surface temperatures and a plate distance H. In the absence of internal sources ($\sigma_e \equiv 0$), the heat Eq. (2.30) yields a linear temperature profile between the parallel plates, e. g. [38]. Thus, the total heat flow $\dot{Q}$ can be determined by

$$\dot{Q} = A \frac{\lambda}{H} \Delta T, \tag{2.31}$$

where A denotes the surface area of the parallel plates. Since the derived equation is analog to Ohm's law for electric circuits, it is convenient to define a thermal resistance $R_{\mathrm{th}} := H/(A\lambda)$. With this, the rules for serial and parallel arrangements of layers of different heat conductivity, layer height and cross-section area can be applied. The rules read

$$R_{\mathrm{th,serial}} = \sum_i R_{\mathrm{th},i}, \qquad \frac{1}{R_{\mathrm{th,parallel}}} = \sum_i \frac{1}{R_{\mathrm{th},i}}. \tag{2.32}$$

Finally, with the total thermal resistance $R_{\mathrm{th,tot}}$ the effective heat conductivity is defined as

$$\lambda_{\mathrm{eff}} := \frac{H_{\mathrm{tot}}}{A_{\mathrm{tot}}} R_{\mathrm{th,tot}}, \tag{2.33}$$

where H_{tot} and A_{tot} denote the total height and cross-section area of the arrangement.

As discussed before for the mass transport, the heat transport can also be effected by rarefaction. With increasing Knudsen numbers, the heat conductivity of a fluid deviates from the heat conductivity in the continuum regime. This rarefaction effect on the heat transport is referred to as Smoluchowski effect, e. g. [39]. The Knudsen dependent heat conductivity of a fluid between two parallel plates obeys the equation

$$\lambda_{\mathrm{f}}(Kn) = \lambda_{\mathrm{f},0} \left(1 + \frac{2 - \alpha_T}{\alpha_T} Kn \right)^{-1}, \tag{2.34}$$

where $\lambda_{\mathrm{f},0}$ denotes the heat conductivity in the continuum regime and α_T denotes the thermal accommodation coefficient. Here, the Knudsen number is calculated according to Eq. (2.21) while the characteristic length is defined as the distance of the parallel plates $L_{\mathrm{char}} := H$. According to [40], the thermal accommodation coefficient can be determined from

$$\log\left(\frac{1}{\alpha_T} - 1 \right) = 0.6 - \frac{(1000\,\mathrm{K}/T) + 1}{C}. \tag{2.35}$$

Here, C depends on the molar mass of the fluid. For water vapor, C takes the value $C = 3.6$.

Porous Media Conduction

In general, the heat transport in a porous medium is calculated by

$$\dot{\boldsymbol{q}} = -\boldsymbol{\lambda}_{\text{eff}} \nabla T, \tag{2.36}$$

where $\boldsymbol{\lambda}_{\text{eff}}$ denotes the effective heat conductivity tensor. In comparison to Darcy's law (2.26), the effective heat conductivity cannot be separated into a product of solely geometry and material dependent parameters. Nevertheless, similar to the approach by J. Kozeny and C. Carman to determine the permeability, see Eq. (2.27), abstract models of the porous medium are applied, consisting of serial and parallel arrangements of the different phases. These abstract models allow for the straightforward determination of the thermal resistance by applying Eq. (2.32). The effective heat conductivity is then calculated from Eq. (2.33). An overview of the numerous model approaches in literature is given in [41] and [42].

The rarefaction effect on the effective heat conductivity in porous media is rarely considered. However, the Smoluchowski effect can be relevant especially for packed beds of distinct particles. This is explained by the fact that in packed beds the single particles are only in point or line contact, which significantly limits the heat transfer between the single particles through the solid phase. As a consequence, the thermal conduction through the fluid phase becomes important. Furthermore, the heat transfer from one particle to another is dominated by the heat transfer through the contact region close around the contact point or line, since the heat transport path through the fluid phase is very small in this region. The small gap size in the contact region leads to a locally increased Knudsen number, and thus, according to Eq. (2.34), locally results in the Smoluchowski effect.

One often applied model to determine the effective heat conductivity of packed beds is the Zehner-Bauer-Schlünder model (ZBS). The model was first developed under negligence of rarefaction effects as well as thermal radiation [43]. Later, the model was extended to account for these effects [44]. In general, the model derives the effective heat conductivity by the examination of two representative particle halves in point contact. The particles are considered as axially symmetric particles around the centerline which connects the particle centers. The curvature of the particle surface is adapted to account for different particle shapes and thus contact conditions. Generally, the particle shape in the model is not identical with the real particle shape. To determine the effective heat conductivity, the model is split in cylindrical shells, neglecting radial thermal conduction. Thus, each shell is a serial arrangement of thermal resistances and the shell resistance can be determined from Eq. (2.32). The total thermal resistance is determined from the parallel arrangement of shells by Eq. (2.32) and with that, the effective heat conductivity is derived according to Eq. (2.33). The final equation for the effective heat conductivity is an extensive function of the form

$$\lambda_{\text{eff}} = \text{fct}\left(\lambda_{\text{f}}(Kn), \lambda_{\text{s}}, \varepsilon, d_{\text{p}}, \varphi, T, \epsilon\right), \tag{2.37}$$

where λ_{f} denotes a mean Knudsen dependent heat conductivity of the fluid phase and is derived from integration of Eq. (2.34) over the contact region. The heat conductivity of the solid phase is denoted by λ_{s}. The parameter φ refers to an empirical fitting parameter to account for the finite contact area of the particles and ϵ is the emission coefficient for thermal radiation of the solid phase. The full set of equations is also described in [41, 40].

Finally, the ZBS model was extended to account for a distribution of the particle diameter as well as for the influence of the flow of the interstitial fluid [45]. However, it has been shown that the explicit consideration of the particle distribution does not increase the model accuracy significantly and it is sufficient to apply a mean particle diameter instead [40]. Moreover, for creeping flow of gases ($Re \ll 1$, $Pr < 1$) the advection induced by the flow can be neglected as the Péclet number is also low: $Pe = RePr \ll 1$.

2.3. Adsorption

The adsorption phenomenon has been studied for a long time. An early quantitative study on adsorption was conducted by the Swedish chemist C. W. Scheele in 1773. The term "adsorption" was introduced by the German physicist H. Kayser in 1881 and is derived from the Latin "adsorpio", meaning "suction". A detailed review on the development of the adsorption science is given in [46]. The fundamentals of adsorption are described in many textbooks, e. g. [47, 48, 49, 50].

Adsorption is the accumulation or concentration of molecules of a fluid phase (adsorptive) at the surface of a solid (adsorbent). The accumulated molecules (adsorbate) are bound to the surface of the solid by adhesive forces. Depending on the type of the adhesive forces, adsorption can be distinguished into physisorption (van der Waals forces) and chemisorption (covalent bonding). Usually, the term adsorption refers to physisorption. As adsorption leads to a reduction of the surface energy of the fluid phase, energy is being released in the form of thermal energy during adsorption, referred to as heat of adsorption. Vice versa, thermal energy input releases the adsorbate to the fluid phase, which is denoted as desorption.

While the effects of adsorption are mostly negligible for solids with a low aspect ratio of surface area to volume, the effects become considerable for solids with a high aspect ratio. Typical materials with a very high aspect ratio of surface area to volume are zeolites (up to $\approx 10^6\,\mathrm{m^2/m^3}$). Zeolites are micro-porous, aluminosilicate minerals (Al_2SiO_5). The high surface area of zeolites results from the numerous inner nano-pores with pore diameters in the range of $1 \ldots 1000\,\mathrm{nm}$. The micro-pores ($< 2\,\mathrm{nm}$) yield the adsorption-selective properties of the zeolites, which are therefore also referred to as molecular sieves. Further, the micro-pores depend on the structure and doping with cations (e. g. Li^+, Na^+, Ca^{2+}) of the aluminosilicate crystal. The meso-pores ($2 \ldots 50\,\mathrm{nm}$) and macro-pores ($> 50\,\mathrm{nm}$) result as a secondary structure from compacting of the primary zeolite crystals (size $1 \ldots 10\,\mu\mathrm{m}$) to bigger agglomerates (size up to several mm).

As mentioned in Sect. 1.2, the adsorption pair of binderless zeolite 13X and water is examined in this thesis. Thus, the following discussion of the adsorption equilibrium, enthalpy and kinetics focuses on adsorption in zeolites and especially on the adsorption pair zeolite 13X and water. The material properties of binderless zeolite 13X are listed in the App. B.

2.3.1. Adsorption Equilibrium

The relative amount of adsorbate in the adsorbent, referred to as (water) uptake, is defined as

$$X := \frac{M_\mathrm{a}}{M_\mathrm{z}}, \tag{2.38}$$

where M_a and M_z denote the mass of the adsorbate and the fully desorbed dry zeolite adsorbent. For a given pressure and temperature, a defined uptake exists for which the ad- and desorption are in equilibrium. Similar to the equilibrium of condensation and evaporation, increasing pressure leads to adsorption while increasing temperature leads to desorption.

As numerous types of zeolites (>200) and other adsorbents exist, many models have been developed to describe the adsorption equilibrium (e. g. Langumir, Freundlich). For the adsorption pair of zeolite 13X and water, the theory of Dubinin-Astakhov can be applied, e. g. [16]. The model is based on the potential theory of Polanyi, which defines an adsorption potential in the micro-pores [51]. The final Dubinin-Astakhov equation for the water uptake at equilibrium reads

$$X_\mathrm{eq}(p,T) = \rho_\mathrm{a} v_\mathrm{a,max} \exp\left[-\left(R_\mathrm{s} T \ln\left(\frac{p_\mathrm{s}}{p}\right)\frac{1}{E_\mathrm{a}}\right)^{n_\mathrm{a}}\right], \tag{2.39}$$

where ρ_a denotes the density of the adsorbate, $v_\mathrm{a,max}$ corresponds to the maximum specific volume of the adsorbate, p_s denotes the saturation pressure of the vapor, E_a is the characteristic energy and n_a the heterogeneity parameter of the adsorption. The parameter values for the adsorption pair zeolite 13X and water are determined in [16] and listed in the App. B. Finally, for this adsorption pair, the adsorption equilibrium is shown in terms of adsorption isotherms in Fig. 2.2 (a).

2.3.2. Adsorption Enthalpy

Thermal energy is released during adsorption. This energy is referred to as heat of adsorption. If the adsorption occurs under constant pressure, the released heat of adsorption is equivalent to the adsorption enthalpy. The adsorption enthalpy Δh_a is derived from the van't Hoff equation

$$\frac{\Delta h_\mathrm{a}}{\bar{R}T} = -\left(\frac{\partial \ln p}{\partial T}\right)_{X_\mathrm{eq}}, \tag{2.40}$$

where $\bar{R}$ denotes the universal gas constant. Incorporating the Dubinin-Astakhov Eq. (2.39) for the adsorption equilibrium as well as the Clausius-Clapeyron equation for the saturation pressure into the van't Hoff equation (2.40) yields [47]

$$\Delta h_\mathrm{a}(X) = \Delta h_\mathrm{e} + E_\mathrm{a} \ln\left(\frac{\rho_\mathrm{a} v_\mathrm{a,max}}{X}\right)^{1/n_\mathrm{a}} + E_\mathrm{a}\beta_\mathrm{a}\frac{T}{n_\mathrm{a}} \ln\left(\frac{\rho_\mathrm{a} v_\mathrm{a,max}}{X}\right)^{(1-n_\mathrm{a})/n_\mathrm{a}}, \tag{2.41}$$

where Δh_e denotes the enthalpy of vaporization and β_a the thermal expansion coefficient of the adsorbate at 20°C. The adsorption enthalpy results from the superposition of the constant enthalpy of vaporization and an enthalpy resulting from the surface bonding. It is found that the adsorption enthalpy is hardly effected by the temperature. For the adsorption pair zeolite 13X and water, the adsorption enthalpy versus the water uptake is shown in Fig. 2.2 (b).

2.3.3. Adsorption Kinetics

The adsorption kinetics describe the limitation of the uptake rate. The uptake rate is limited by the mass transport processes, that is the diffusion in the micro-porous zeolite, e.g. [52]. Assuming an isothermal state in the adsorbent, approximating the pressure by a parabolic distribution and applying linear adsorption isotherms, the mass balance equation of the adsorbate can be integrated. This approach yields the well-known Linear Driving Force approximation (LDF) [53]

$$\frac{\partial X}{\partial t} = k_\mathrm{a}\left(X_\mathrm{eq} - X\right), \tag{2.42}$$

where k_a denotes the adsorption kinetics parameter.

The underlying assumptions of the LDF approximation are not strictly valid for any adsorption pair. For example, the adsorption isotherms are not linear for the adsorption pair of zeolite 13X and water, see Fig. 2.2 (a). In this case, a more accurate description of the uptake process is

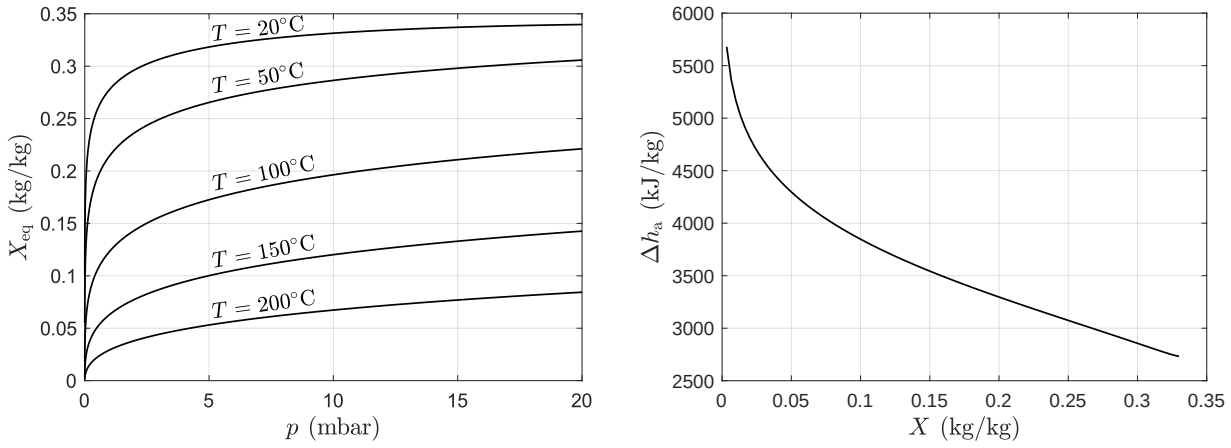

(a) Adsorption equilibrium X_eq according to Eq. (2.39). (b) Adsorption enthalpy Δh_a according to Eq. (2.41).

Figure 2.2.: Adsorption equilibrium and enthalpy for the adsorption pair zeolite 13X and water.

derived by explicitly solving the Fickian diffusion in the micro-porous adsorbent phase and locally applying the exact equations for the adsorption equilibrium and enthalpy. As an example, this procedure is applied for a single adsorbent particle in [54]. Nevertheless, it has been shown that the LDF Eq. (2.42) still provides a good approximation and is successfully applied even in cases where the underlying assumptions are not strictly met [55]. Furthermore, the LDF approximation provides low computational costs in comparison to the more accurate approach.

To apply the LDF Eq. (2.42), the adsorption kinetics parameter has to be determined. The parameter depends on the effective diffusivity of the adsorbate D_{eff} and on the macroscopic geometry of the adsorbent. For a spherical adsorbent particle, the adsorption kinetics parameter reads

$$k_{\mathrm{a}} = D_{\mathrm{eff}} \frac{60}{d_{\mathrm{p}}^2}. \tag{2.43}$$

The effective diffusivity of the adsorbate D_{eff} is related to the diffusivity of the adsorptive D_{av} in the nano-pores of the adsorbent by

$$D_{\mathrm{eff}} = \frac{D_{\mathrm{av}}}{\tau_{\mathrm{z}} \left(1 + \zeta\right)}, \tag{2.44}$$

where τ_{z} refers to the mean tortuosity of the zeolite adsorbent. Here, ζ is a non-linear function of the pressure and temperature. In general, the diffusivity of the adsorptive D_{av} is determined from

$$D_{\mathrm{av}} = D_{Kn} + D_{\mathrm{vis}}, \tag{2.45}$$

where D_{Kn} denotes the Knudsen diffusivity and D_{vis} is the viscous diffusivity in the continuum regime. Under low pressure conditions as examined in this thesis ($p \leq 20\,\mathrm{mbar}$) and considering the little diameter of the macro-pores in the micro-porous zeolite ($d_{\mathrm{mp}} < 1\,\mu\mathrm{m}$), the Knudsen number according to Eq. (2.21) is always $Kn > 1$. In this case, the diffusion mainly results from the Knudsen diffusion ($D_{Kn} \gg D_{\mathrm{vis}}$) and the diffusivity of the adsorptive is well approximated by $D_{\mathrm{av}} = D_{Kn}$. The Knudsen diffusivity is derived as

$$D_{Kn} = \frac{4}{3} d_{\mathrm{mp}} \sqrt{\frac{R_{\mathrm{s}} T}{2\pi}}. \tag{2.46}$$

Finally, this yields the effective diffusivity of the adsorbate

$$D_{\mathrm{eff}} = \frac{\frac{4}{3} d_{\mathrm{mp}} \sqrt{\frac{R_{\mathrm{s}} T}{2\pi}}}{\tau_{\mathrm{z}} \left(1 + \frac{\rho_{\mathrm{z}}}{\varepsilon\left(X\right)} R_{\mathrm{s}} T \frac{\partial X_{\mathrm{eq}}}{\partial p}\right)}. \tag{2.47}$$

3. State of Research

Thermal energy storage (TES) has been applied in buildings for a long time and the first industrial applications date back to the 19th century. Early examples for industrial TES are regenerators for heat recovery and steam storages (e. g. Ruth's storage). It might be a surprise that thermochemical heat storages were already applied in the 1880s for transport purposes (e. g. exhaust free Honigmann locomotive). Around the same time, C. Benz introduced the modern automobile with a combustion engine. After almost a century, TES gained new attention in the 1970s due to increasing oil prices during the energy crisis. Research and development were intensified in the fields of solar power generation as well as domestic and district heating. Many TES concepts studied today have already been proposed or even studied in the 70s, including thermochemical energy storages. [56]

The research on TES had a revival in the late 1990s due to the again increasing oil prices as well as the growing awareness of the climate change and its consequences. The research results of the past decades are summarized in [7] and a topical overview on TES research over a broad range of applications is given in [6]. Available technologies for seasonal TES are reviewed in [57]. A more specific review with the focus on thermochemical heat storage for building applications is given in [58]. Finally, the research on TES based on adsorption is reviewed e. g. in [15, 14, 59, 9] and an overview on the studied adsorbent materials can be found in [60].

3.1. Modeling and Simulation of Closed Low-Pressure Adsorbers

As mentioned in the introduction, closed low-pressure adsorbers are mainly studied in the context of heat pump application. The applied models are reviewed in [61, 62] and classified into three groups of model types: thermodynamic, lumped parameter and spatially resolved continuum models. An extensive and topical review on the modeling of thermochemical heat storages and transformers is given in [63]. The review focuses on spatially resolved continuum models and separately discusses the models for TES based on adsorption, absorption and chemical reactions. Yet, most quoted references focus on heat pump application with adsorbers of a small scale (length of mass transport path $L < 0.1\,\mathrm{m}$). In the following, only the most relevant publications related to the present thesis are discussed. The focus is on spatially resolved continuum models for closed low-pressure adsorbers. Special attention is given to adsorbers of larger scale (length of mass transport path $L = 0.1 \ldots 1\,\mathrm{m}$) and to adsorbers with zeolite adsorbent, both particularly suitable for TES.

To the author's knowledge, only a few publications on the modeling of closed low-pressure adsorbers of a large scale exist. In [64], a cylindrical silica-gel adsorber with radial vapor mass flow (radial adsorber) is modeled. The diameter is $d = L = 0.15\,\mathrm{m}$. Similarly, a radial zeolite adsorber is modeled in [65]. However, in both studies, the adsorber is modeled by a lumped parameter model. Thus, the models have to be calibrated by adjusting model parameters so that the numerical results fit to experimental data. As an advantage, the lumped parameter models provide low computational times, and thus allow for system simulations. As a drawback, the model results are limited to the particular experimental setup applied for calibration. What is more, the lumped parameter models cannot provide insight into the internal mass and heat transport processes in the adsorbent bulk. Hence, no conclusions for an optimization of the adsorber design can be derived directly. In contrast, spatially resolved models are developed in this thesis, allowing for a detailed analysis of the transport processes in closed low-pressure adsorbers, both for small- and large-scale adsorbers.

The first spatially resolved continuum models for closed low-pressure adsorbers (in the following only referred to as "models") were published in the mid-1990s. In [66] a model for a cylindrical adsorber with integrated spiral heat exchanger is presented. However, the model only considers the heat transport and neglects the mass transport limitations in the adsorber. One of the first models for a zeolite 13X adsorber is described in [67]. The model already considers the mass transport by applying Darcy's law, however, the model is limited to a one-dimensional cylindrical adsorber configuration and neglects the radial dependencies. Furthermore, local adsorption equilibrium and constant thermophysical parameters are assumed. Compared to early models, the present thesis provides two-dimensional models for the mass and heat transport including the local deviation from adsorption equilibrium, that is the limitation by the internal mass transport resistance in the zeolite adsorbent is considered. Additionally, both the temperature and the water uptake dependencies of the thermophysical parameters are accounted for.

One of the first two-dimensional models for a zeolite adsorber is presented in [68]. The model considers the mass as well as the heat transport and is applied to examine the adsorption into a thin zeolite layer ($L = 1 \ldots 3\,\mathrm{mm}$) on a heat exchanger plate. A more sophisticated two-dimensional model for a zeolite adsorber is established in [69]. The model considers the mass and heat transport, the local deviation from adsorption equilibrium (limitation by internal mass transport resistance in zeolite adsorbent) as well as the dependency of most thermophysical parameters. Moreover, the rarefaction effect on the mass transport due to the low pressure (slip effect, see Sect. 2.2.1) is considered. However, the applied model approach to account for the rarefaction effect is arguable. In addition, the study is limited to a radial adsorber with a thin adsorbent layer. Further models of similar approach and adsorber configuration are discussed in the aforementioned reviews [61, 62, 63]. More recent studies examine the effect of the porosity of the adsorbent bulk [70], account for the local deviation from thermal equilibrium [71], apply more advanced numerical schemes [72], or even consider the heat and mass transfer in the single adsorbent particles [73]. While all these studies focus on small-scale adsorbers (length of mass transport path L is only a few centimeters) for heat pump applications, the present thesis considers adsorber configurations of a larger scale ($L = 0.1 \ldots 1\,\mathrm{m}$) suitable for TES. Furthermore, the rarefaction effects on both the mass and heat transport are thoroughly analyzed and accurately modeled in the present thesis.

To date, the relevance of the mass and heat transport processes in closed low-pressure adsorbers remain under discussion [74]. As the discussion is mainly related to small-scale adsorbers for heat pump application, the central point of discussion is whether the mass transport limitations are negligible, that is whether it is valid to assume a uniform pressure throughout the adsorber. In [75] an order of magnitude analysis is conducted to derive criteria for conduction dominance and negligible mass transport resistance. To evaluate the criteria, numerical simulations are conducted. Similarly, in [74], radial packed bed adsorbers are simulated to study the relevance of the mass transport limitation. Both studies show that the mass transport limitations increase with increasing length of the mass transport path L in the adsorber. However, the studies are limited to radial adsorbers of a small scale, that is the mass transport path is short ($L = 0.01 \ldots 0.04\,\mathrm{m}$). Again, in comparison, the present thesis thoroughly evaluates the mass and heat transport processes of closed low-pressure adsorbers of larger scale ($L = 0.1 \ldots 1\,\mathrm{m}$).

With respect to the adsorbent configuration (see Fig. 1.4), mainly packed bed adsorbers with granules and powder adsorbent are examined in literature. A review on the influence of the particle diameter of the adsorbent particles in packed bed adsorbers is given in [10]. The authors conclude that the particle diameter strongly effects the adsorber performance. Further, it is concluded that the optimum range of the particle diameter is $0.2 \ldots 0.6\,\mathrm{mm}$. The same conclusions are found by numerical simulations in [74]. In addition, an optimum particle diameter is determined for minimum adsorption duration and explained by inter- and intraparticle mass transport limitations. However, the conclusions are derived only for small-scale adsorbers. The present thesis completes this analysis by examining the influence of the particle diameter and evaluating the optimum particle diameters for closed low-pressure adsorbers of larger scale.

In comparison to packed bed adsorbers, honeycomb adsorbers for TES application are only considered in few studies. In [76], the performance of a packed bed adsorber is compared to a honeycomb adsorber by lab-scale experiments and simplified simulations. A more detailed model is established in [77] and applied to a heat recovery system of a paint-drying system. The model approach is similar to the model approach of the one-dimensional SCM developed in this thesis. However, both studies examine open adsorption systems and no compressibility and rarefaction effects are considered. Therefore, the results cannot be transferred to closed low-pressure adsorbers.

With respect to the modeling of the adsorption, that is the adsorption equilibrium, enthalpy and kinetics, validated models are available. The adsorption equilibrium of water in binderless zeolite 13X is experimentally studied and the applicability of the Dubinin-Astakhov Eq. (2.39) is validated, e. g. [78, 16, 79]. The adsorption enthalpy for the same adsorption pair is typically calculated from Eq. (2.41) and validated with experimental data from [51] in [16]. The adsorption kinetics is typically modeled by the LDF approximation, see Eq. (2.42), and validated for the uptake of water into zeolite 13X in [16]. Finally, the pore structure of binderless zeolite 13X is examined in [80] and the hydrothermal stability is confirmed in [81]. In summary, all model equations required for the description of the adsorption process in the examined zeolite 13X adsorber are available and validated and can be applied in the present thesis.

3.2. Mass and Heat Transport under Low-Pressure Conditions

As emphasized above, the rarefaction effects on both the mass and heat transport are thoroughly analyzed and accurately modeled in the present thesis. The related fundamental research and the adopted models are reviewed in the following sections. The models are separately discussed for mass and heat transport and distinguished into models for regular porous media (honeycombs) and random porous media (packed beds of granules and powder).

Mass Transport:

The rarefaction effects on the mass transport in regular porous media (honeycombs) are mainly studied in the field of micro and nano fluidics. An extensive overview on the field is given in [82]. The introduction of the first-order slip boundary condition for the slip regime is commonly attributed to J. C. Maxwell [30]. The mass transport in the free molecular regime was described by M. Knudsen [83]. To extend the applicability of the continuum equations (Navier-Stokes Eq. (2.7)) into the transition regime, slip approaches of higher order have been developed and are reviewed in [84]. However, no analytical solution covering all flow regimes can be derived. Instead, different numerical methods are applied [82]. An early numerical study deploying the Bubnov-Galerkin method to examine the rarefied flow in a circular channel over a broad Knudsen range is presented in [85]. From the 1990s on, the Direct-Simulation-Monte-Carlo method (DSMC, developed by G. A. Bird [86]) is applied to derive numerical solutions of the Boltzmann equation for any Knudsen number, e. g. [87, 88, 89]. The results have been validated in several experiments, e. g. [90, 91]. Finally, the numerical results for the different flow regimes have been condensed into an analytical fitting curve for the non-dimensional mass flow (so-called Poiseuille coefficient) over the whole Knudsen range by Sharipov et al. [92]. This fitting curve is applied in the present thesis, thus implicitly incorporating the results from sophisticated DSMC simulations.

The rarefaction effects on the mass transport in random porous media (packed beds of granules and powder) are mainly studied in the field of shale and tight gas reservoirs. A review on the applied model approaches and simulation methods is given in [93]. Darcy's law was first extended by L. J. Klinkenberg to account for the slip effect [36]. In [94] an analytical expression for the empirical factor of the Klinkenberg correlation is derived from a simple model of the porous medium. The porous medium is modeled as a parallel arrangement of straight channels. A similar but more general model approach is applied in [95]. The porous medium is modeled as an arrangement of

cylindrical, tortuous channels and the dependency of the permeability on the Knudsen number is derived by incorporating a slightly modified flow condition function from Beskok et al. [26]. Similarly, the so-called Knudsen permeability correction factor is derived in [96] and validated against experimental data over the whole Knudsen range. In the present thesis, a similar model approach is applied to derive the Knudsen permeability correction factor. However, instead of the flow condition function from Beskok et al. [26], the aforementioned Poiseuille coefficient from Sharipov et al. [92] is incorporated.

Heat Transport:

The rarefaction effects on the heat transport in regular porous media (honeycombs) mainly occur in the gaseous phase in the channels. A review on the convective heat transfer in the slip flow regime is given in [97]. In contrast to the models presented in the review, no temperature jump at the gas-solid boundary is considered in the present thesis. Additionally, the radial dependency of the vapor temperature in the honeycomb channel is neglected. Therefore, no Nusselt correlations are required. With respect to the effective heat conductivity of honeycombs, the rarefaction effects are usually negligible since the heat conductivity of the solid phase is higher by several orders of magnitude compared to the heat conductivity of the rarefied gas phase. Nevertheless, the effective heat conductivity can be determined by thermal resistance models as presented e. g. in [98]. Similarly, a simple thermal resistance model is applied in the present thesis.

The rarefaction effects on the heat transport in random porous media (packed beds of granules and powder), are relevant in diverse applications such as nuclear reactors, vacuum insulation and solar receivers. In general, the rarefaction effects are considered in the effective heat conductivity of the packed beds. A broad overview on the existing models for the effective heat conductivity is given in [41, 42]. An often applied model is the ZBS model [43, 44], see fundamentals Sect. 2.2.2. The model accounts for the rarefaction effect on the heat conductivity of the interstitial gas in the packed bed. A similar model was developed independently in [99]. However, the model is limited to packed beds with a regular packing structure. The ZBS model has been extended to account for particle distribution and gas flow [45] and for very high conductivity ratios of solid and gas phase [100]. Today, rarefaction effects on the effective heat conductivity are also examined by numerical simulations with the Discrete-Element-Method, e. g. [101]. Nevertheless, a recent study proved once again that the ZBS model in its original form [44] describes the heat transport under rarefied conditions very well [102]. Therefore, the ZBS model is also applied in the present thesis.

In a very recent study, the effective heat conductivity of packed beds of zeolite granules in closed low-pressure adsorbers has been examined by experiments and compared to an analytical model [103]. The applied model is based on a thermal resistance model presented in [104], which is similar to the ZBS model. The model is modified by incorporating the water uptake dependency of the heat conductivity of the adsorbent particle. The uptake dependency is determined by the Bruggeman's volume averaging method. An alternative approach to describe the uptake dependency of the zeolite heat conductivity is presented in [105]. The approach determines the heat conductivity from a parallel arrangement of the thermal resistances of the adsorbent and adsorbate phase. However, it is suspected that the two approaches over- and underestimate respectively the uptake dependency of the heat conductivity of the adsorbent particle. Another generic approach is given in [106]. This approach is based on sub-models of parallel and serial arrangements of thermal resistances for the different phases in a wet particle. However, the model is not directly applicable to low-pressure systems. Therefore, a modified version of the model is implemented in this thesis.

4. Model Description

As outlined in the introduction in Sect. 1.3, a stepwise development of three adsorber models from pore to storage scale is conducted in this work. In this thesis, "pore scale" refers to the interstitial volume in the adsorbent bulk (e. g. the honeycomb channels), while "storage scale" denotes a representative section of the whole adsorber. The stepwise model development contributes to a better understanding and thus mathematical description of the underlying physical processes. For this purpose, a one-dimensional Single Channel Model (SCM) is derived at first. The SCM resolves the adsorber on the pore scale, allowing for a separate description of the physical processes in the gas and adsorbent phase. However, the SCM is limited to one-dimensional adsorber configurations. To overcome this limitation, the SCM is extended to a Multi Channel Model (MCM) by thermally coupling multiple parallel adsorbent channels, each described by the SCM. With the MCM it is possible to study two-dimensional adsorber configurations of higher practical relevance. Still, the MCM is limited to one-dimensional gas flow in the parallel adsorbent channels, and thus can only be applied to honeycomb adsorbents. Finally, a General Continuum Model (GCM) is developed for the general description of closed low-pressure adsorbers with varying adsorbent configurations, that is powder, granules and honeycomb adsorbents, see Fig. 1.4 in Sect. 1.2.
The descriptions of the SCM, MCM and GCM are included in part in:

[107] M. Schaefer and A. Thess. One-dimensional model of a closed low-pressure adsorber for thermal energy storage. *International Journal of Heat and Mass Transfer*, 2018.

[108] M. Schaefer and A. Thess. Simulation of a closed low-pressure honeycomb adsorber for thermal energy storage. *International Journal of Heat and Mass Transfer*, 2018.

[109] M. Schaefer and A. Thess. Modeling and simulation of closed low-pressure zeolite adsorbers for thermal energy storage. *International Journal of Heat and Mass Transfer*, 2019.

4.1. Single Channel Model

4.1.1. Approach and Assumptions

The general scheme and storage principle of a closed adsorption system has been described in the introduction in Sect. 1.2. The focus is on the adsorber during discharging. The closed low-pressure adsorber configuration examined by the SCM is shown in Fig. 4.1.

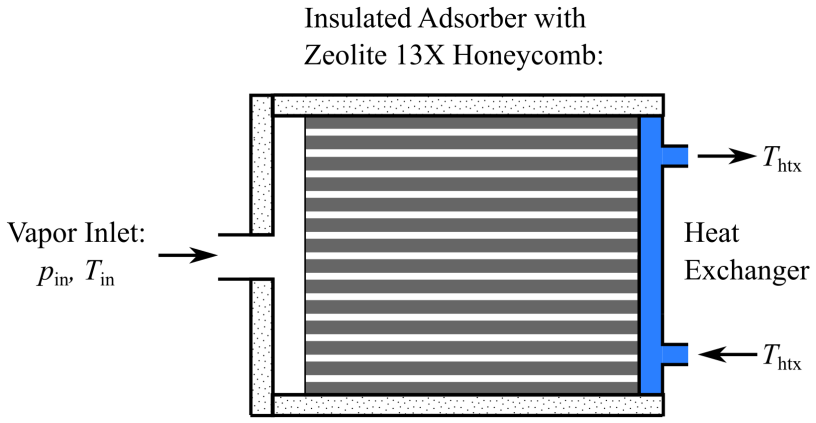

Figure 4.1.: Closed low-pressure adsorber configuration examined by the SCM. Arrangement of honeycomb adsorbent blocks with heat extraction at the closed end of the adsorber.

The adsorber is box-shaped and ideal thermal insulation is assumed. Water vapor is supplied through a single inlet at one side of the adsorber while heat is extracted by a heat exchanger at the opposite closed end. Regarding the adsorbent, binderless zeolite 13X is studied. Nevertheless, the model is applicable to other adsorption pairs in general. With respect to the adsorbent configuration, honeycomb adsorbents are considered. The adsorbent properties are assumed uniform throughout the adsorber. Further, the adsorbent channels are square-shaped and characterized by a constant channel width and web thickness. The web thickness is defined here as the thickness of the adsorbent layer of a single adsorbent channel.

During the discharging process, that is the adsorption process, vapor flows into the adsorber by the vapor inlet. The inlet pressure p_{in} is assumed constant throughout the process. This assumption implies that the evaporator is not effected by the adsorption process and no evaporator limitations occur. Further, the temperature of the inflowing vapor T_{in} is assumed to be equal to the saturation temperature. Given enough void space at the adsorber inlet, the inflowing vapor distributes uniformly over the honeycomb arrangement. Hence, the vapor advances equally into the honeycomb channels. As mentioned above, the released heat of adsorption is extracted by a heat exchanger at the closed end of the honeycomb arrangement. It is assumed that the surface temperature of the heat exchanger T_{htx} is uniform and constant over the whole closed end. Hence, no limitations by the heat exchanger are considered.

It can be concluded that for the adsorber configuration studied by the SCM, the mass and heat transport processes are in parallel direction, and thus the problem is one-dimensional. Furthermore, the transport processes in the single channels of the honeycomb arrangement are identical for the examined adsorber system and no mass and heat transfer occurs between the channels. Thus, the analysis of a single channel from the honeycomb arrangement is sufficient. The reduced problem of a single adsorbent is shown in Fig. 4.2. For simplification and dimensions reduction, the square adsorbent channel is approximated by a circular adsorbent channel with an inner channel diameter $d_{\mathrm{c,i}}$, an outer diameter $d_{\mathrm{c,o}}$ and a length L. The aspect ratio of the diameters is defined as a parameter and relates to the porosity of the adsorbent channel

$$\gamma := \frac{d_{\mathrm{c,o}}}{d_{\mathrm{c,i}}}, \qquad \varepsilon = \frac{1}{\gamma^2}. \tag{4.1}$$

Although the SCM is one-dimensional on the storage scale, it includes two-dimensional aspects on the pore scale such as the parabolic velocity profile of the vapor in the channel as well as the radial profile of the pressure and water uptake in the adsorbent.

Regarding the mass transfer, the left boundary condition at the vapor channel inlet is

$$p(z = 0) = p_{\mathrm{in}}, \tag{4.2}$$

where z denotes the coordinate in the longitudinal direction. At the opposite closed end of the channel the boundary condition reads

$$\dot{m}(z = L) = 0, \tag{4.3}$$

where $\dot{m}$ denotes the mass flux of the vapor. For the derivation of the SCM it is further required to take the boundary condition $\dot{m} = 0$ at the lateral surface of the adsorbent channel into account.

With respect to the heat transfer, the right boundary condition at the heat exchanger is

$$T(z = L) = T_{\mathrm{htx}}, \tag{4.4}$$

while at the left boundary the boundary condition

$$\dot{q}(z = 0) = 0 \tag{4.5}$$

is applied, where $\dot{q}$ denotes the heat flux. Again, for the derivation of the SCM it is further required to take the boundary condition $\dot{q} = 0$ at the lateral surface of the adsorbent channel into account.

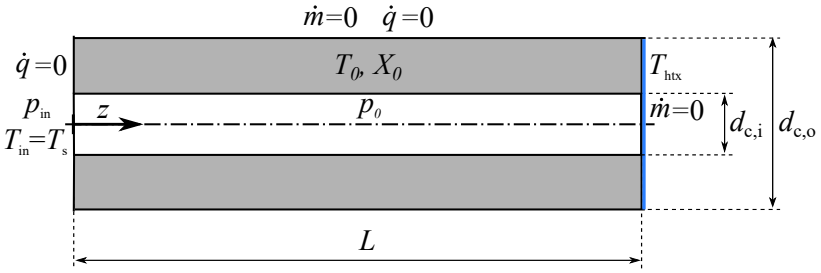

Figure 4.2.: Reduced problem of a single adsorbent channel with boundary and initial conditions. For simplification and dimensions reduction, the square adsorbent channel is approximated by a circular adsorbent channel.

Finally, no boundary conditions are required for the water uptake X since the derived equation for the water uptake is an initial value problem. This is further discussed in the subsequent Sect. 4.1.2.

The initial conditions are set to an uniform state of equilibrium

$$p(t=0) = p_0, \qquad T(t=0) = T_0, \qquad X(t=0) = X_{\mathrm{eq}}\left(p_0, T_0\right), \tag{4.6}$$

with the water uptake being defined as

$$X\left(z,t\right) := \frac{M_{\mathrm{a}}}{M_{\mathrm{z}}}, \tag{4.7}$$

where M_{a} and M_{z} denote the mass of the adsorbate, that is the adsorbed vapor, and the fully desorbed dry zeolite adsorbent. X_{eq} is the water uptake at equilibrium.

In summary, given the boundary conditions (4.2) to (4.5) as well as the initial conditions (4.6), the three dependent variables pressure $p\left(z,t\right)$, temperature $T\left(z,t\right)$ and water uptake $X\left(z,t\right)$ are computed.

Besides the aforementioned assumptions regarding the examined adsorber configuration, the discharging process and the reduced problem, several assumptions about the underlying physical processes are applied. The main physical assumptions are:

- The vapor behaves as an ideal gas.
- The vapor behaves as a viscous Newton-fluid.
- The vapor flow is a creeping flow ($Re \ll 1$).
- The kinetic and potential energy of the vapor is negligible.
- Due to the low pressure, rarefaction effects on the mass and heat transport are considered.
- Local thermal equilibrium is assumed between the gas and the adsorbent phase.
- The heat conduction in the adsorbent is well described by Fourier's law.
- The adsorption process can be described by the Linear Driving Force approximation (LDF).
- The adsorption equilibrium is well approximated by the Dubinin-Astakhov equation.
- The adsorption enthalpy depends on the water uptake.
- The adsorbent and adsorbate is incompressible.
- The temperature and water uptake dependencies of the material parameters (e. g. density, porosity, viscosity, heat capacity, thermal conductivity) are accounted for.

The relevance of the mentioned assumptions for the governing equations as well as further assumptions are discussed in the following sections.

4.1.2. Balance Equations

To derive the governing equations for the pressure and temperature, the mass balance equation for the compressible vapor as well as the energy balance equation for the vapor and the adsorbent are to be formulated. Since local thermal equilibrium is assumed, it is sufficient to formulate one energy balance equation for the three phases: vapor, adsorbent and adsorbate. Only at the vapor inlet, the vapor temperature is distinguished from the adsorbent temperature to account for convective cooling by the inflowing vapor. With respect to the momentum balance, the explicit evaluation of the momentum balance equation is not required since the vapor flow is assumed as a viscous, creeping flow. Instead, the available solutions of the momentum balance equation for the mass flux are considered. The system of mass and energy balance equations is closed by incorporation of the transport equations[1] for the mass and heat flux.

To derive the governing equation for the water uptake, the LDF approximation is applied. The LDF approximation itself is derived from the mass balance equation for the adsorbate in the adsorbent, and thus can be referred to as an adsorption balance equation.

Mass Balance Equation

The evaluation of the general mass balance equation, see Eq. (2.4) in Sect. 2.1, for the compressible vapor in the channel as well as in the inner pores of the zeolite adsorbent yields

$$\frac{\partial}{\partial t}\left(\varepsilon\rho_{\mathrm{v}} + (1-\varepsilon)\,\varepsilon_{\mathrm{z}}\,(X)\,\bar{\rho}_{\mathrm{v,z}}\right) = -\frac{\partial}{\partial z}\left(\varepsilon\dot{m}_{\mathrm{c}}\right) - \sigma_{m,\mathrm{v,z}}, \tag{4.8}$$

where ε denotes the porosity of the adsorbent channel, which is related to the cross-section areas of the vapor channel and of the zeolite adsorbent A_{c} and A_{z} by

$$\varepsilon = \frac{A_{\mathrm{c}}}{A_{\mathrm{z}} + A_{\mathrm{c}}}, \qquad (1-\varepsilon) = \frac{A_{\mathrm{z}}}{A_{\mathrm{z}} + A_{\mathrm{c}}}. \tag{4.9}$$

The porosity $\varepsilon_{\mathrm{z}}(X)$ refers to the inner porosity of the micro-porous zeolite adsorbent, which depends on the local water uptake. Moreover, ρ_{v} and $\bar{\rho}_{\mathrm{v,z}}$ denote the density of the vapor in the channel and the mean density of the vapor in the inner pores of the zeolite adsorbent. On the right side of the equation, $\dot{m}_{\mathrm{c}}$ denotes the mean mass flux of the vapor in the longitudinal direction over the cross-section of the vapor channel. Finally, $\sigma_{m,\mathrm{v,z}}$ represents the volumetric mass sink of the vapor in the zeolite adsorbent due to the adsorption. Note that in [107] the mass balance is formulated separately for the vapor in the vapor channel and in the inner pores of the zeolite adsorbent. Here, for consistency and better comparability of the three models (SCM, MCM, GCM), one mass balance equation is formulated for both vapor domains together. Nevertheless, the final forms of the mass balance equations are identical.

The adsorption mass sink $\sigma_{m,\mathrm{v,z}}$ can be determined from the definition of the water uptake according to Eq. (4.7), see App. A.1, resulting in

$$\sigma_{m,\mathrm{v,z}} = (1-\varepsilon)\,\rho_{\mathrm{z}}\frac{\partial X}{\partial t}, \tag{4.10}$$

where ρ_{z} denotes the density of the zeolite adsorbent, including the inner pores, and $\partial X/\partial t$ refers to the adsorption rate. With the specified adsorption mass sink term Eq. (4.10) and considering that the porosity ε is a constant, the mass balance Eq. (4.8) can be rewritten as

$$\varepsilon\frac{\partial\rho_{\mathrm{v}}}{\partial t} + (1-\varepsilon)\left(\rho_{\mathrm{z}}\frac{\partial X}{\partial t} + \frac{\partial}{\partial t}\left(\varepsilon_{\mathrm{z}}\,(X)\,\bar{\rho}_{\mathrm{v,z}}\right)\right) = -\varepsilon\frac{\partial\dot{m}_{\mathrm{c}}}{\partial z}. \tag{4.11}$$

It can be shown that the vapor accumulation in the inner pores of the zeolite adsorbent (term related to $\bar{\rho}_{\mathrm{v,z}}$) can be neglected, see App. A.2.

[1] In this thesis, "transport equations" solely denotes the equations for the mass and heat flux.

Regarding the vapor density, the ideal gas law

$$\rho_\mathrm{v} = \frac{p}{R_\mathrm{s} T} \tag{4.12}$$

can be applied due to the low vapor pressure, where R_s denotes the specific gas constant of the vapor. Applying the product rule to the time derivative of the vapor density, the mass balance equation finally reduces to

$$\frac{\varepsilon}{R_\mathrm{s}} \frac{1}{T} \frac{\partial p}{\partial t} - \frac{\varepsilon}{R_\mathrm{s}} \frac{p}{T^2} \frac{\partial T}{\partial t} + (1-\varepsilon)\, \rho_\mathrm{z} \frac{\partial X}{\partial t} = -\varepsilon \frac{\partial \dot{m}_\mathrm{c}}{\partial z}. \tag{4.13}$$

The second term on the left side describes the effect of the temperature on the pressure by thermal expansion of the vapor. Furthermore, the pressure is effected by the adsorption mass sink and by the local expansion or compression of the vapor.

Energy Balance Equation

Under the assumption of local thermal equilibrium between the vapor and the zeolite adsorbent and neglecting the kinetic and potential energy of the vapor, the evaluation of the general energy balance equation, see Eq. (2.9) in Sect. 2.1, for the vapor, adsorbent and adsorbate yields

$$\frac{\partial}{\partial t}\Big((1-\varepsilon)\, \rho_\mathrm{z} e_\mathrm{z} + (1-\varepsilon)\, \rho_\mathrm{z} X e_\mathrm{a} + \Big(\varepsilon \rho_\mathrm{v} + (1-\varepsilon)\, \varepsilon_\mathrm{z}\,(X)\, \bar{\rho}_\mathrm{v,z} \Big) e_\mathrm{v} \Big) = -\frac{\partial \dot{q}}{\partial z} - \frac{\partial}{\partial z}\Big(\varepsilon \dot{m}_\mathrm{c} h_\mathrm{v} \Big), \tag{4.14}$$

where e_z, e_a and e_v denote the specific internal energy of the zeolite adsorbent, the adsorbate and the vapor. On the right side, $\dot{q}$ denotes the heat flux due to thermal conduction in the longitudinal direction through all three phases and h_v refers to the specific enthalpy of the vapor in the channel. The equilibrium assumption can be assumed valid, since the length of the zeolite adsorbent is much higher than the thickness and the volumetric heat capacity of the rarefied vapor is very low.

Since the zeolite adsorbent and the adsorbate can be assumed as incompressible and the vapor is assumed as an ideal gas, the internal energies can be determined by integration of the fundamental relation $\mathrm{d}e = c(T)\mathrm{d}T$, see Eq. (2.11) in Sect. 2.1. Similarly, the enthalpy of the vapor can be determined from $\mathrm{d}h = c_{p,\mathrm{v}} dT$. In addition, the internal energy of the adsorbate can be related to the internal energy of the vapor e_v and to the adsorption enthalpy Δh_a, see App. A.3,

$$e_\mathrm{a} = e_\mathrm{v} + R_\mathrm{s} T - \Delta h_\mathrm{a}. \tag{4.15}$$

Additionally, the enthalpy of the vapor is related to its internal energy and temperature by

$$h_\mathrm{v} = e_\mathrm{v} + R_\mathrm{s} T. \tag{4.16}$$

With this, the product rule is applied to the time derivative on the left side of the energy balance equation and the time derivatives of the internal energies are substituted while considering the Leibniz integral rule. On the right side, the product rule is also applied to the enthalpy flux. Considering that the porosity ε is a constant and taking the Eq. (4.15) and (4.16) into account, this procedure yields

$$\begin{aligned}
&\Big((1-\varepsilon)\, \rho_\mathrm{z} c_\mathrm{z} + (1-\varepsilon)\, \rho_\mathrm{z} X c_\mathrm{a} + \Big(\varepsilon \rho_\mathrm{v} + (1-\varepsilon)\, \varepsilon_\mathrm{z}\,(X)\, \bar{\rho}_\mathrm{v,z} \Big) c_\mathrm{v} \Big) \frac{\partial T}{\partial t} - (1-\varepsilon)\, \rho_\mathrm{z} \Big(\Delta h_\mathrm{a} - R_\mathrm{s} T \Big) \frac{\partial X}{\partial t} \\
&= -\frac{\partial \dot{q}}{\partial z} - \varepsilon \dot{m}_\mathrm{c} c_{p,\mathrm{v}} \frac{\partial T}{\partial z} - \varepsilon R_\mathrm{s} T \frac{\partial \dot{m}_\mathrm{c}}{\partial z} + e_\mathrm{v} \left[-\varepsilon \frac{\partial \dot{m}_\mathrm{c}}{\partial z} - \varepsilon \frac{\partial \rho_\mathrm{v}}{\partial t} - (1-\varepsilon) \left(\rho_\mathrm{z} \frac{\partial X}{\partial t} + \frac{\partial}{\partial t} \Big(\varepsilon_\mathrm{z}\,(X)\, \bar{\rho}_\mathrm{v,z} \Big) \right) \right],
\end{aligned} \tag{4.17}$$

where c_z, c_a and c_v denote the specific heat capacity of the zeolite adsorbent, adsorbate and vapor.

Due to the low vapor pressure, the vapor density is lower by several orders of magnitude compared to the zeolite adsorbent and the adsorbate while the specific heat capacities are of same order. Thus, the heat capacity term of the vapor on the left side is negligible. On the right side, the term in square brackets is identical with the implicit form of the vapor mass balance Eq. (4.11), and thus equal to zero. This allows for the elimination of the generally unknown internal energy of the vapor e_v. Finally, the energy balance equation reads

$$(1-\varepsilon)\,\rho_\mathrm{z}\Big(c_\mathrm{z}+Xc_\mathrm{a}\Big)\frac{\partial T}{\partial t}-(1-\varepsilon)\,\rho_\mathrm{z}\Big(\Delta h_\mathrm{a}-R_\mathrm{s}T\Big)\frac{\partial X}{\partial t}=-\frac{\partial \dot{q}}{\partial z}-\varepsilon\dot{m}_\mathrm{c}c_{p,\mathrm{v}}\frac{\partial T}{\partial z}-\varepsilon R_\mathrm{s}T\frac{\partial \dot{m}_\mathrm{c}}{\partial z}. \quad (4.18)$$

The reduction of the adsorption enthalpy by $R_\mathrm{s}T$ results from the vapor sink in the zeolite adsorbent. This effect is generally not considered in literature and also neglected in [107] and [108]. On the right side, the second term accounts for the convective heat transport by the vapor, while the last term describes the change of temperature due to expansion or compression of the vapor.

Adsorption Balance Equation

The LDF approximation is applied to describe the adsorption process. This approximation is derived from the mass balance equation of the adsorbate in the adsorbent, see Sect. 2.3.3. At a set longitudinal position z in a cylindrical adsorbent, the mass balance equation reads [110]

$$\frac{\partial}{\partial t}\Big(\rho_\mathrm{z}X\Big)=\frac{1}{r}\left[\frac{\partial}{\partial r}\left(rD_\mathrm{eff}\frac{\partial}{\partial r}\Big(\rho_\mathrm{z}X\Big)\right)\right], \quad (4.19)$$

where r denotes the radial coordinate and D_eff denotes the effective diffusivity of the adsorbate in the adsorbent. This mass balance equation is valid as long as the longitudinal diffusion of the adsorbate in the adsorbent is negligible compared to the radial diffusion. Since the vapor diffuses radially from the inner vapor channel into the adsorbent, the gradient of pressure and thus the gradient of the adsorbate is mainly in radial direction.

With the assumption of radial thermal equilibrium in the adsorbent and thus an approximately constant effective diffusivity in radial direction, the mass balance equation can be integrated. Furthermore, the pressure profile is approximated by a parabolic approach and the boundary conditions are implemented [110]. This procedure yields the well-known LDF equation

$$\frac{\partial X}{\partial t}=k_\mathrm{a}\,(X_\mathrm{eq}-X) \quad (4.20)$$

where k_a denotes the adsorption kinetics parameter incorporating material and geometry properties.

System of Balance Equations

Finally, the balance equations (4.13), (4.18) and (4.20) form a system of coupled partial differential equations (PDEs) which can be written as

$$\begin{pmatrix} \dfrac{\varepsilon}{R_\mathrm{s}}\dfrac{1}{T} & -\dfrac{\varepsilon}{R_\mathrm{s}}\dfrac{p}{T^2} & \rho_\mathrm{c} \\ 0 & \rho_\mathrm{c}\Big(c_\mathrm{z}+Xc_\mathrm{a}\Big) & -\rho_\mathrm{c}\Big(\Delta h_\mathrm{a}-R_\mathrm{s}T\Big) \\ 0 & 0 & 1 \end{pmatrix} \cdot \begin{pmatrix} \dfrac{\partial p}{\partial t} \\ \dfrac{\partial T}{\partial t} \\ \dfrac{\partial X}{\partial t} \end{pmatrix} = \begin{pmatrix} -\varepsilon\dfrac{\partial \dot{m}_\mathrm{c}}{\partial z} \\ -\dfrac{\partial \dot{q}}{\partial z}-\varepsilon\dot{m}_\mathrm{c}c_{p,\mathrm{v}}\dfrac{\partial T}{\partial z}-\varepsilon R_\mathrm{s}T\dfrac{\partial \dot{m}_\mathrm{c}}{\partial z} \\ k_\mathrm{a}\,(X_\mathrm{eq}-X) \end{pmatrix} \quad (4.21)$$

with the adsorbent channel density ρ_c definition

$$\rho_\mathrm{c}=(1-\varepsilon)\,\rho_\mathrm{z}. \quad (4.22)$$

To close the system, further equations are required and discussed in the following sections.

4.1.3. Transport Equations

To close the system of balance equations (4.21), transport equations for the mass flux $\dot{m}_\mathrm{c}$ and the heat flux $\dot{q}$ are required. In this thesis, "transport equations" solely denotes the equations for mass and heat flux. These transport equations are derived below.

Mass Transport

The mean mass flux in the vapor channel $\dot{m}_\mathrm{c}$ is related to the mean velocity in the channel u_c by

$$\dot{m}_\mathrm{c} = \rho_\mathrm{v} u_\mathrm{c}. \tag{4.23}$$

In general, the mean velocity is determined by averaging the velocity profile in the vapor channel. Considering the vapor as a viscous Newton-fluid and assuming creeping flow (Stokes flow, $Re \ll 1$), the velocity profile of a circular channel flow in the continuum regime is described by the Hagen-Poiseuille equation. However, with decreasing vapor pressure or decreasing channel diameter the velocity profile deviates from the continuum solution. The degree of this so-called rarefaction effect is characterized by the non-dimensional Knudsen number Kn, see Eq. (2.21). Up to the slip regime ($Kn < 0.1$), it is possible to derive an analytical solution, see Sect. 2.2.1.

However, no analytical solution covering all flow regimes has yet been derived. Nevertheless, the transition regime ($0.1 < Kn < 10$) and the molecular regime ($10 < Kn$) have been studied numerically by DSMC methods, see Sect. 3.2. With the numerical results, the mean vapor velocity in the vapor channel can be described by

$$u_\mathrm{c} = \frac{d_\mathrm{c,i}}{2\rho_\mathrm{v}\sqrt{2R_\mathrm{s}T}} \left(-G_\mathrm{P}\left(Kn\right) \frac{\partial p}{\partial z} + G_\mathrm{T}\left(Kn\right) \frac{p}{T} \frac{\partial T}{\partial z} \right), \tag{4.24}$$

where $G_\mathrm{P}(Kn)$ and $G_\mathrm{T}(Kn)$ denote the Poiseuille and thermal creep coefficient respectively [92]. The simulation results are incorporated into these coefficient functions by non-linear regression over the numerical data.

The Poiseuille coefficient $G_\mathrm{P}(Kn)$ can be understood as a pressure-induced non-dimensional mass flux and accounts for the slip effect, but is not limited to the slip regime. An analytical expression of the Poiseuille coefficient for a circular channel is given in [92] and reads

$$G_\mathrm{P}(\delta(Kn)) = \frac{1.505 + 0.0524\delta^{0.75}\ln\left(\delta\right)}{1 + 0.738\delta^{0.78}} + \left(\frac{\delta}{4} + 1.018\right) \frac{\delta}{1.0738 + \delta}, \tag{4.25}$$

where $\delta(Kn)$ denotes the rarefaction parameter which is related to the Knudsen number by

$$\delta(Kn) = \frac{\sqrt{\pi}}{2} \frac{1}{Kn}. \tag{4.26}$$

The evolution of the Poiseuille coefficient G_P over the Knudsen number Kn is shown in Fig. 4.3 (a). The figure reveals the so-called Knudsen paradox, that is a minimum exists for the Poiseuille coefficient. Additionally, the Poiseuille coefficients corresponding to the slip and no-slip approach are plotted. The slip approach approximates the Poiseuille coefficient of Eq. (4.25) well in the slip regime and reaches a maximum deviation of 33% in the molecular regime. The no-slip approach however, underestimates the Poiseuille coefficient of Eq. (4.25) already in the slip regime with up to 50% and declines to zero in the molecular regime.

The thermal creep coefficient $G_\mathrm{T}(Kn)$ accounts for the thermal creep effect, that is a temperature gradient induced mass flow. The effect is mostly negligible in the presence of a pressure gradient. Nevertheless, the effect is included in the SCM and the relevance is discussed with the simulation results. Note that the thermal creep effect was not included in [107]. Besides the numerical data, no analytic expression for the thermal creep coefficient valid over the whole Knudsen range is given in the literature. It is found that numerical data from [89] is well approximated by the function

$$G_\mathrm{T}(\delta(Kn)) = \left(0.7473\delta + \frac{3.478 + 18.5\delta}{2.538 + 9.69\delta}\right)^{-1}. \tag{4.27}$$

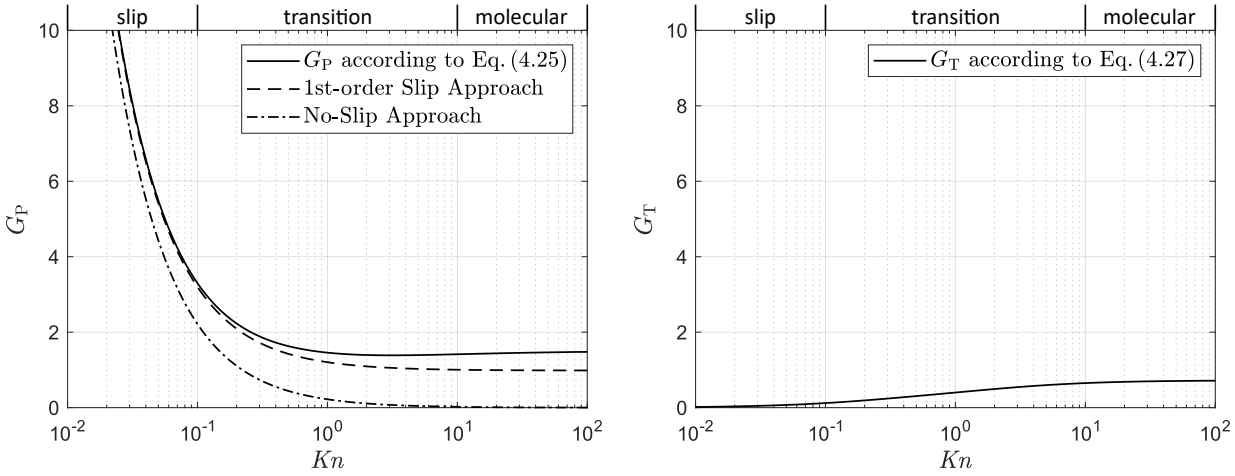

(a) Poiseuille coefficient G_P (b) Thermal creep coefficient G_T

Figure 4.3.: Poiseuille coefficient G_P and thermal creep coefficient G_T versus Knudsen number Kn.

The evolution of the Poiseuille coefficient G_T over the Knudsen number Kn is shown in Fig. 4.3 (b). It is obvious that the effect is negligible in the continuum regime ($Kn < 0.1$). Moreover, the comparison with the Poiseuille coefficient G_P shown in Fig. 4.3 (a) confirms that the effect is only of relevance in the presence of small pressure gradients.

Finally, considering the Eq. (4.25) and (4.27) for the Poiseuille and thermal creep coefficient in the mean vapor velocity Eq. (4.24), the mean mass flux according to Eq. (4.23) in the vapor channel can be determined for any Knudsen number. Since the implemented coefficient functions are based on the work of Sharipov et al., the mass transport model is referred to as the Sharipov Model here.

Heat Transport

The heat flux $\dot{q}$ accounts for the thermal conduction in the longitudinal direction through the three phases vapor, zeolite adsorbent and adsorbate, and can be determined by Fourier's law

$$\dot{q} = -\lambda_{\text{eff}} \frac{\partial T}{\partial z}, \tag{4.28}$$

where λ_{eff} denotes the effective heat conductivity of the adsorbent channel in the longitudinal direction. Since the heat flow through the vapor channel and through the adsorbent is parallel, the effective heat conductivity is calculated according to

$$\lambda_{\text{eff}} = (1-\varepsilon)\lambda_{\text{z,eff}}(X) + \varepsilon\lambda_{\text{v}}, \tag{4.29}$$

where $\lambda_{\text{z,eff}}(X)$ refers to the effective heat conductivity of the zeolite adsorbent with the adsorbate and the vapor in the inner pores and λ_{v} to the heat conductivity of the vapor in the channel.

Since the amount of the adsorbate in the zeolite adsorbent can vary, the effective heat conductivity of the zeolite adsorbent depends on the water uptake. To the author's knowledge, only sparse experimental data zeolite 13X adsorbent is available in literature. For binderless zeolite 13X granules, a mean value of $\lambda_{\text{z,eff}} = 0.4\,\text{W/(mK)}$ is indirectly determined by calibration of a numerical model with measured temperature fields in [16]. For zeolite 13X honeycombs, a value of $\lambda_{\text{z,eff}} = 0.15\,\text{W/(mK)}$ is measured at a water uptake of $X = 0.25\,\text{kg/kg}$ in [111]. However, this measurement is for zeolite 13X with a PTFE binder of low heat conductivity. Thus, for honeycombs consisting of binderless zeolite 13X higher effective heat conductivity values of the adsorbent can be expected. Since no other data is available, the effective heat conductivity of a honeycomb adsorbent consisting of binderless zeolite 13X is assumed as the arithmetic mean of the binderless zeolite 13X granules and the zeolite 13X honeycomb adsorbent with PTFE binder.

To determine the water uptake dependency of the effective heat conductivity of the zeolite adsorbent, a modified version of a model presented in [106] is applied. The model derives the effective heat conductivity from a serial arrangement of two sub-models, containing a parallel and a serial arrangement of the different phases, see Sect. 2.2.2. However, the original form of the model is not applicable for low vapor pressures since the heat conductivity of the interstitial vapor decreases with the pressure and thus unrealistically reduces the effective heat conductivity of the zeolite adsorbent. To overcome this model restriction, the two sub-models are simply arranged in a parallel instead of a serial arrangement. Hence, the effective heat conductivity of the zeolite adsorbent is calculated as a weighted average of the parallel and serial sub-models

$$\lambda_{\mathrm{z,eff}}(X) = (1-\alpha_{\mathrm{p}})\,\lambda_{\mathrm{z,eff,parallel}} + \alpha_{\mathrm{p}}\lambda_{\mathrm{z,eff,serial}} \tag{4.30}$$

where α_{p} denotes an empirical weighing factor.

The weighing factor is determined by fitting the model to the sparse experimental data. For the binderless zeolite 13X granules, the weighing factor is determined to $\alpha_{\mathrm{p}} = 0.227$, while for the zeolite 13X honeycomb adsorbent with PTFE binder a value of $\alpha_{\mathrm{p}} = 0.734$ is found. As mentioned above, for the binderless zeolite 13X honeycomb adsorbent the arithmetic value of these two cases is applied. The resulting dependency of the effective heat conductivity of the zeolite adsorbent $\lambda_{\mathrm{z,eff}}$ on the water uptake X is shown in Fig. 4.4. The effective heat conductivity of the binderless zeolite 13X honeycomb adsorbent varies ±25% around a mean value of $\lambda_{\mathrm{z,eff}} = 0.27\,\mathrm{W/(mK)}$.

Finally, the heat conductivity of the vapor in the vapor channel has to be determined. In general, the heat conductivity in the continuum regime only depends on the temperature. However, with decreasing vapor pressure or decreasing channel diameter the heat conductivity deviates from the value of the continuum regime (Smoluchowski effect). The degree of this rarefaction effect is characterized by the Knudsen number. To determine the Knudsen dependency of the heat conductivity of the vapor in the channel, the equation for a gas between two parallel plates, see fundamentals in Sect. 2.2.2, is applied

$$\lambda_{\mathrm{v}}(Kn) = \lambda_{\mathrm{v},0}\left(1 + \frac{2-\alpha_T}{\alpha_T}Kn\right)^{-1}, \tag{4.31}$$

where $\lambda_{\mathrm{v},0}$ denotes the heat conductivity of the vapor in the continuum regime and α_T denotes the thermal accommodation coefficient. The latter is calculated according to Eq. (2.35) in Sect. 2.2.2. Since the heat conductivity of the vapor is significantly lower than that of the zeolite adsorbent, the rarefaction effect on the effective heat conductivity of a honeycomb adsorbent is generally marginal.

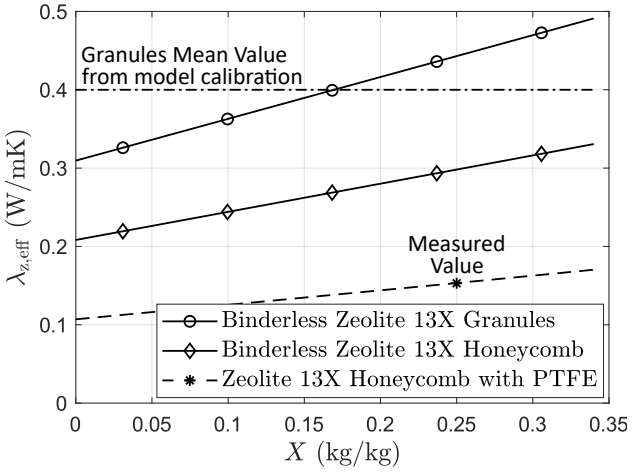

Figure 4.4.: Dependency of the effective heat conductivity of the zeolite adsorbent $\lambda_{\mathrm{z,eff}}$ on the water uptake X for different adsorbent configurations.

In conclusion, the heat flux the adsorbent channel can be determined according to Eq. (4.28) and Eq. (4.29) by considering the Eq. (4.30) and (4.31) for effective heat conductivity of the zeolite adsorbent and the heat conductivity of the vapor in the vapor channel. Note that a simpler version of the model for the effective heat conductivity of the adsorbent channel has been applied in [107] and [108].

4.1.4. Adsorption Equations

To close the system of balance equations (4.21), adsorption equations for the adsorption equilibrium X_{eq}, the adsorption enthalpy Δh_{a} and the adsorption kinetics parameter k_{a} are required. The equations are introduced in the fundamentals in Sect. 2.3. Nevertheless, the equations are briefly summarized in the following sections again.

Adsorption Equilibrium

It is shown in the experimental study [16] that the adsorption equilibrium of the adsorption pair binderless zeolite 13X and water can be described by the Dubinin-Astakhov equation

$$X_{\mathrm{eq}} = \rho_{\mathrm{a}} v_{\mathrm{a,max}} \exp\left[-\left(R_{\mathrm{s}} T \ln\left(\frac{p_{\mathrm{s}}}{p}\right)\frac{1}{E_{\mathrm{a}}}\right)^{n_{\mathrm{a}}}\right], \tag{4.32}$$

where ρ_{a} denotes the density of the adsorbate, $v_{\mathrm{a,max}}$ corresponds to the maximum specific volume of the adsorbate, p_{s} denotes the saturation pressure of the vapor, E_{a} is the characteristic energy and n_{a} the heterogeneity parameter of the adsorption. In accordance with [16], the density of the adsorbate is calculated from

$$\rho_{\mathrm{a}} = \frac{\rho_{\mathrm{a,20°C}}}{1 + \beta_{\mathrm{a}}\left(T - 293.15\,\mathrm{K}\right)}, \tag{4.33}$$

with $\rho_{\mathrm{a,20°C}}$ as the density and β_{a} as the thermal expansion coefficient of the adsorbate at 20°C.

Adsorption Enthalpy

The adsorption enthalpy can be determined from the vant-Hoff equation, see [47], and reads

$$\Delta h_{\mathrm{a}}(X) = \Delta h_{\mathrm{e}} + E_{\mathrm{a}} \ln\left(\frac{\rho_{\mathrm{a}} v_{\mathrm{a,max}}}{X}\right)^{1/n_{\mathrm{a}}} + E_{\mathrm{a}}\beta_{\mathrm{a}}\frac{T}{n_{\mathrm{a}}} \ln\left(\frac{\rho_{\mathrm{a}} v_{\mathrm{a,max}}}{X}\right)^{(1-n_{\mathrm{a}})/n_{\mathrm{a}}}, \tag{4.34}$$

where Δh_{e} denotes the enthalpy of vaporization of the adsorbate. Comparison of the equation to experimental data shows good agreement [16].

Adsorption Kinetics

The adsorption kinetics parameter of a circular adsorbent channel is derived in [110] and reads

$$k_{\mathrm{a}} = 4 D_{\mathrm{eff}} \left(\frac{\frac{5}{6}\gamma^4 - 2\gamma^3 + \gamma^2 + \frac{2}{3}\gamma - \frac{1}{2}}{\gamma - 1}\frac{d_{\mathrm{c,i}}^2}{4}\right)^{-1}, \tag{4.35}$$

where γ is defined as the aspect ratio of the outer and inner channel diameters according to Eq. (4.1).

Due to the low vapor pressure the Knudsen number in the inner pores of the zeolite adsorbent is generally $Kn > 1$. Hence, the effective diffusivity can be determined from

$$D_{\mathrm{eff}} = \frac{D_{Kn}}{\tau_{\mathrm{a}}\left(1 + \zeta\right)} = \left(\frac{4}{3} d_{\mathrm{mp}} \sqrt{\frac{R_{\mathrm{s}} T}{2\pi}}\right)\left(\tau_{\mathrm{z}}\left(1 + \frac{\rho_{\mathrm{z}}}{\varepsilon\left(X\right)} R_{\mathrm{s}} T \frac{\partial X_{\mathrm{eq}}}{\partial p}\right)\right)^{-1} \tag{4.36}$$

where D_{Kn} denotes the Knudsen diffusivity, d_{mp} refers to the mean macro pore diameter and τ_{z} to the mean tortuosity of the zeolite adsorbent.

4.1.5. Constitutive Equations

To evaluate the system of balance equations (4.21), the model parameters must be defined. The applied values of the constant model parameters are summarized in App. B.

The temperature dependency is considered for the following parameters: vapor viscosity μ (required for the calculation of the Knudsen number), specific heat capacity of the vapor at constant pressure $c_{p,\mathrm{v}}$, heat conductivity of the adsorbate λ_{a} (assumed equivalent to water), heat conductivity of the vapor in the continuum regime $\lambda_{0,\mathrm{v}}$ and saturation pressure p_{s}. These parameters are calculated by polynomial correlation functions given in the VDI Heat Atlas [112] and summarized in App. B. Note that simpler but similarly accurate approaches were applied in [107] and [108].

With respect to the specific heat capacity of the adsorbate, it is shown in [113] that the temperature dependency should be considered. The specific heat capacity of adsorbed water increases from 1000 to 4000 J/(kg K) in the range of 0°C to 125°C. Hence, the approximation

$$c_{\mathrm{a}} = c_{\mathrm{a,min}} + \int_{T_{\mathrm{min}}}^{T} \alpha_1 \exp\left[-\alpha_2 \left(\tilde{T} - T_{\mathrm{ref}}\right)^2\right] \mathrm{d}\tilde{T} \tag{4.37}$$

suggested in [113] is applied. Here, $c_{\mathrm{a,min}}$ refers to the minimum of the specific heat capacity of the adsorbate at the temperature T_{min} while α_1 and α_2 are fitting parameters.

Finally, the dependency of the inner porosity of the zeolite adsorbent $\varepsilon_{\mathrm{z}}(X)$ on the water uptake is considered. The variable porosity is determined by simply subtracting the varying volume of the adsorbate from the maximum volume of the inner pores of the adsorbent, yielding

$$\varepsilon_{\mathrm{z}}(X) = \varepsilon_{\mathrm{z,max}} - \frac{\rho_{\mathrm{z}}}{\rho_{\mathrm{a}}} X, \tag{4.38}$$

where $\varepsilon_{\mathrm{z,max}}$ refers to the maximum inner porosity of the fully desorbed dry zeolite adsorbent.

4.2. Multi Channel Model

4.2.1. Approach and Assumptions

The closed low-pressure adsorber configuration examined by the MCM is shown in Fig. 4.5. Except for the heat exchanger, the adsorber configuration is identical to the configuration examined by the SCM and described in Sect. 4.1.1. Here, the heat exchanger is integrated into the adsorber by heat exchanger plates between the stacked layers of honeycomb blocks. In general, the modified

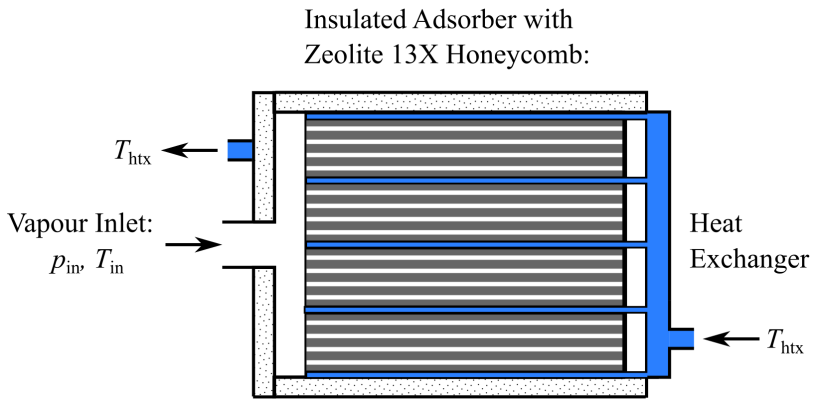

Figure 4.5.: Closed low-pressure adsorber configuration examined by the MCM. The heat exchanger is integrated into the adsorber by heat exchanger plates between the honeycomb blocks.

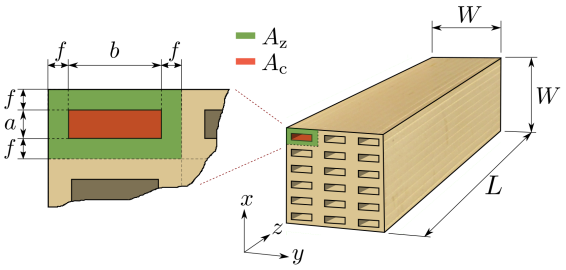

(a) Geometry of the honeycomb blocks: honeycomb length L, honeycomb width W, channel height a, channel width b, web thickness f, cross-section area of zeolite adsorbent A_z and vapor channel A_c.

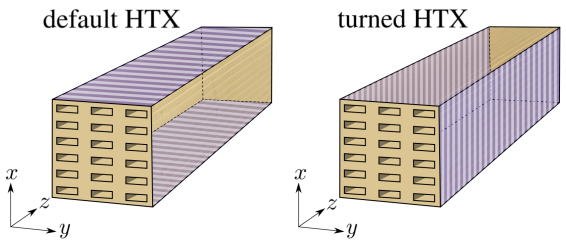

(b) Two possible heat exchanger orientations: default and turned heat exchanger (HTX). The heat exchanger boundaries are striped and shaded.

Figure 4.6.: Honeycomb geometry and heat exchanger orientations.

adsorber configuration enhances the heat transfer from the adsorbent to the heat exchanger by reducing the length of the heat transport path in the adsorbent. Thus, the thermal performance of the adsorber is improved.

The discharging process is analog to the discharging process described for SCM, only that the heat is extracted along the sides of the honeycomb blocks by the internal heat exchanger. Again, the surface temperature of the heat exchanger is assumed uniform and constant over the heat exchanger plates. In addition, the inlet pressure can now be varied over time to control the thermal power of the adsorber. Thus, the model has to be extended by a controller equation.

With respect to the honeycomb adsorbent, rectangular channels are considered. The geometry of the honeycomb blocks is shown in Fig. 4.6 (a). The aspect ratio of the outer height or width of a single adsorbent channel to the vapor channel height or width is defined as

$$\gamma_a := \frac{a+2f}{a}, \qquad \gamma_b := \frac{b+2f}{b}, \qquad \varepsilon = \frac{1}{\gamma_a \gamma_b}. \tag{4.39}$$

For the general case of rectangular channels with $a \neq b$, the effective heat conductivity of the honeycomb adsorbent is non-isotropic $\lambda_{\mathrm{eff},x} \neq \lambda_{\mathrm{eff},y}$. Hence, the orientation of the heat exchanger plates to the honeycomb blocks is of relevance for honeycomb blocks with non-square channels. The two possible heat exchanger orientations are given in Fig. 4.6 (b).

Following from the description above, it can be concluded that the transport processes in the single honeycomb blocks separated by the heat exchanger plates are identical. Furthermore, the examined adsorber configuration leads to planar temperature and pressure fields in the single honeycomb blocks. Assuming that the solution has the same symmetry as the geometry and the boundary conditions, the problem can be reduced to the analysis of one half-section of a honeycomb block. The reduced problem for the default orientation of the heat exchanger is depicted in Fig. 4.7.

Regarding the mass transfer, the boundary conditions read

$$p(z=0) = p_{\mathrm{in}}(t), \qquad \dot{m}(z=L) = 0. \tag{4.40}$$

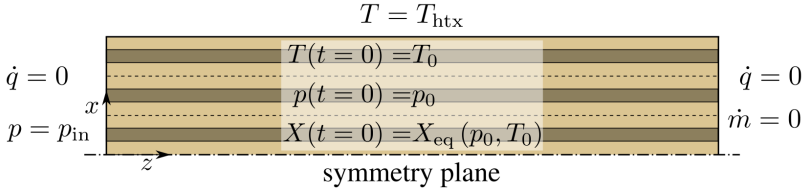

Figure 4.7.: Reduced problem: Half-section of a single honeycomb block with boundary and initial conditions. Since the vapor in the channels can only flow in the longitudinal direction, no boundary condition for the mass transfer at the heat exchanger boundary is required.

As mentioned above, the inlet pressure is either held constant or varied over time to control the thermal power output. Since the vapor in the channels can only flow in the longitudinal direction, no boundary condition for the mass transfer at the heat exchanger boundary is required.

With respect to the heat transfer, the boundary conditions are

$$T(x = W/2) = T_{\mathrm{htx}}, \qquad \dot{q}(z = 0) = 0, \qquad \dot{q}(z = L) = 0. \tag{4.41}$$

The initial conditions are set to a uniform state of equilibrium

$$p(t = 0) = p_0, \qquad T(t = 0) = T_0, \qquad X(t = 0) = X_{\mathrm{eq}}\left(p_0, T_0\right). \tag{4.42}$$

In summary, given the boundary conditions (4.40) and (4.41) as well as the initial conditions (4.42) the three dependent variables pressure $p\left(\boldsymbol{x}, t\right)$, temperature $T\left(\boldsymbol{x}, t\right)$ and water uptake $X\left(\boldsymbol{x}, t\right)$ are computed, with $\boldsymbol{x} = (z, x)$ or $\boldsymbol{x} = (z, y)$, depending on the heat exchanger orientation. Finally, the assumptions listed for the SCM at the end of Sect. 4.1.1 are also applied to the MCM.

4.2.2. Balance Equations

The MCM is derived by thermally coupling multiple parallel adsorbent channels, each described by the SCM. Therefore, the system of balance equations for the single channels of the honeycomb is identical to the system of balance equations (4.21) except for a source/sink term $\sigma_{e,\mathrm{c}}$ which is added to the energy balance equation. Hence, the honeycomb is modeled as a continuum in the longitudinal direction, whereas the model is discrete in the transversal direction. The total system of coupled PDEs can be written as

$$\begin{pmatrix} \frac{\varepsilon}{R_{\mathrm{s}}}\frac{1}{T} & -\frac{\varepsilon}{R_{\mathrm{s}}}\frac{p}{T^2} & \rho_{\mathrm{c}} \\ 0 & \rho_{\mathrm{c}}\Big(c_{\mathrm{z}} + X c_{\mathrm{a}}\Big) & -\rho_{\mathrm{c}}\Big(\Delta h_{\mathrm{a}} - R_{\mathrm{s}} T\Big) \\ 0 & 0 & 1 \end{pmatrix}_i \cdot \begin{pmatrix} \frac{\partial p}{\partial t} \\ \frac{\partial T}{\partial t} \\ \frac{\partial X}{\partial t} \end{pmatrix}_i = \begin{pmatrix} -\varepsilon\frac{\partial \dot{m}_{\mathrm{c}}}{\partial z} \\ -\frac{\partial \dot{q}}{\partial z} - \varepsilon \dot{m}_{\mathrm{c}} c_{p,\mathrm{v}}\frac{\partial T}{\partial z} - \varepsilon R_{\mathrm{s}} T\frac{\partial \dot{m}_{\mathrm{c}}}{\partial z} + \sigma_{e,\mathrm{c}} \\ k_{\mathrm{a}}\left(X_{\mathrm{eq}} - X\right) \end{pmatrix}_i \tag{4.43}$$

with

$$i = 1 \ldots \frac{N_{\mathrm{c}}}{2}, \tag{4.44}$$

where i indicates the channel, starting from the channel at the heat exchanger boundary, and N_{c} denotes the numbers of channels in the longitudinal section of the honeycomb block.

4.2.3. Transport Equations

Mass Transport

The mean mass flux in a single vapor channel of the honeycomb $\dot{m}_{\mathrm{c}}$ is generally calculated as described for the SCM in Sect. 4.1.3, applying Eq. (4.23) and (4.24). Note that the Knudsen number for the circular channel is defined with half the channel diameter as the characteristic length, while for the rectangular channel the Knudsen number is defined with the full channel height. Thus, the inner channel diameter $d_{\mathrm{c,i}}$ has to be substituted by twice the channel height a in Eq. (2.21). Additionally, the rectangular adsorbent channels are no longer approximated by circular adsorbent channels. This increases the model accuracy especially for rectangular channels with $a \neq b$. Consequently, the Poiseuille and thermal creep coefficients G_{P} and G_{T} have to be modified for rectangular channels.

Table 4.1.: Fitting parameters of Poiseuille and thermal creep coefficient G_P and G_T for rectangular channels with aspect ratio b/a according to Eq. (4.46) and (4.47).

b/a	ζ_1	ζ_2	ξ_1	ξ_2	ξ_3	ξ_4	ξ_5
1	0.0703	0.5713	0.837	4.989	31.92	2.088	9.904
2	0.1143	0.7607	0.8473	6.2	48.32	3.541	19.79
4	0.1404	0.8872	0.8567	2.09	17.03	1.546	7.864
10	0.1562	0.9645	0.872	3.784	44.32	3.711	21.59

The Poiseuille coefficients for different aspect ratios of channel width to height b/a are determined by fitting functions to the numerical data given in [114]. In general, it is possible to use the same form of Eq. (4.25) as a fitting function. For the case of a square channel, this yields

$$G_\mathrm{P}(\delta((Kn)) = \frac{0.8372 - 0.1021\delta^{0.8747}\ln(\delta)}{1 + 3.032\delta^{0.9376}} + \left(\frac{\delta}{14.227} + 0.7036\right)\frac{\delta}{0.3652 + \delta}, \tag{4.45}$$

with δ according to Eq. (4.26). For the general case of a rectangular channel with $a \neq b$ similar functions were determined. However, in anticipation of the simulation results discussed in Sect. 6.2 it is sufficient to apply the substantially shorter fitting function

$$G_\mathrm{P}(\delta((Kn)) = \zeta_1\delta + \zeta_2, \tag{4.46}$$

where ζ_1 and ζ_2 denote the fitting parameters. The form of the fitting function is equivalent to the Poiseuille coefficient of the first order slip approach. The values of the parameters ζ_i for different aspect ratios b/a of a rectangular channel are summarized in Tab. 4.1.

Regarding the thermal creep coefficient G_T, a fitting function of the form

$$G_\mathrm{T}(\delta((Kn)) = \left(\xi_1\delta + \frac{\xi_2 + \xi_3\delta}{\xi_4 + \xi_5\delta}\right)^{-1}, \tag{4.47}$$

with ξ_i as fitting parameters is found to fit the numerical data from [114] well. The form of the fitting function is equivalent to Eq. (4.27). The values of the parameters ξ_i for different aspect ratios b/a of a rectangular channel are summarized in Tab. 4.1.

Heat Transport

The heat flux $\dot{q}$ in the longitudinal direction in the single channels of the honeycomb is calculated as described for the SCM in Sect. 4.1.3, applying Eq. (4.28) and (4.29).

To couple the single channels thermally, a source/sink term $\sigma_{e,\mathrm{c}}$ has been added to the energy balance equation, see Eq. (4.43). The term accounts for the heat exchange between the channels due to thermal conduction and is determined by

$$\sigma_{e,\mathrm{c},i} = \frac{1}{a + 2f} \cdot \left(\dot{q}_{\mathrm{cpl},i,i+1} - \dot{q}_{\mathrm{cpl},i,i-1}\right), \tag{4.48}$$

where $\dot{q}_{\mathrm{cpl},i,i+1}$ and $\dot{q}_{\mathrm{cpl},i,i-1}$ are calculated as heat fluxes analog to Fourier's law. For $\dot{q}_{\mathrm{cpl},i,i+1}$ this approach yields

$$\dot{q}_{\mathrm{cpl},i,i+1} = \frac{\lambda_{\mathrm{eff},x,i+1} + \lambda_{\mathrm{eff},x,i}}{2}\frac{T_{i+1} - T_i}{a + 2f}. \tag{4.49}$$

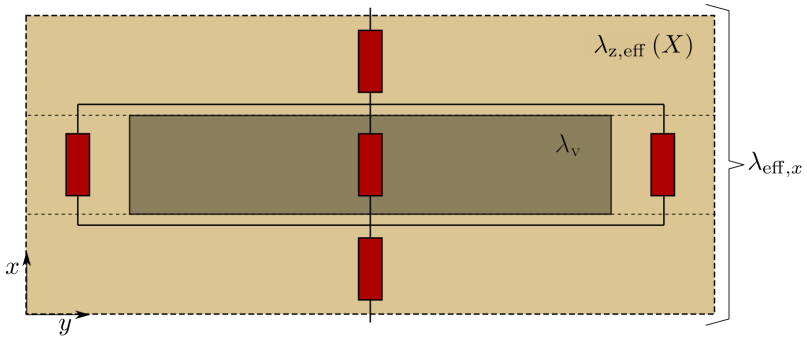

Figure 4.8.: Thermal resistance model to determine the effective heat conductivity $\lambda_{\mathrm{eff},x}$ of a single adsorbent channel. For the geometry parameters see Fig. 4.6 (a).

For $\dot{q}_{\mathrm{cpl},i,i-1}$ the indices in Eq. (4.49) simply have to be reduced by one. To increase the model accuracy, the heat flux at the heat exchanger boundary $\dot{q}_{\mathrm{cpl,htx}} = \dot{q}_{\mathrm{cpl},1,0}$ is modeled analogue to a one-sided finite difference approximation of second order, see e. g. [115], which leads to

$$\dot{q}_{\mathrm{cpl,htx}} = \lambda_{\mathrm{eff},x,1} \frac{-T_2 + 9T_1 - 8T_{\mathrm{htx}}}{3\,(a + 2f)}. \tag{4.50}$$

For the case of the turned heat exchanger, the channel width b simply has to be substituted for the channel height a and vice versa and the transversal coordinate x has to be exchanged with y in Eq. (4.48), (4.49) and (4.50).

The effective heat conductivity $\lambda_{\mathrm{eff},x}$ of each adsorbent channel is derived from a simple thermal resistance model, see Fig. 4.8. The analysis of the thermal resistance model yields

$$\lambda_{\mathrm{eff},x} = \lambda_{\mathrm{z,eff}}(X) \frac{\gamma_a}{(\gamma_a - 1) + \gamma_b \left((\gamma_b - 1) + \dfrac{\lambda_{\mathrm{v}}}{\lambda_{\mathrm{z,eff}}(X)} \right)^{-1}}, \tag{4.51}$$

with γ_a and γ_b as defined in Eq. (4.39) and the effective heat conductivity of the zeolite adsorbent $\lambda_{\mathrm{z,eff}}(X)$ according to Eq. (4.30). Again, for the case of the turned heat exchanger, the channel height a has to be substituted for the channel width b and vice versa in Eq.(4.51) to determine the effective heat conductivity $\lambda_{\mathrm{eff},y}$.

4.2.4. Adsorption Equations

The adsorption equilibrium X_{eq}, the adsorption enthalpy Δh_{a} and the adsorption kinetics parameter k_{a} are calculated by the equations given for the SCM in Sect. 4.1.4. However, to evaluate Eq. (4.35) for the adsorption kinetics parameter, the equivalent inner and outer diameters $d_{\mathrm{c,i}}$ and $d_{\mathrm{c,o}}$ have to be determined first. For this purpose, the transformation relations

$$d_{\mathrm{c,i}} = \frac{1}{\pi}(a + b), \qquad d_{\mathrm{c,o}} = 2\sqrt{\frac{2f}{\pi}\,(2f + (a + b)) + \left(\frac{4}{\pi}a\right)^2}, \tag{4.52}$$

from [110] are applied. It can be shown that with increasing aspect ratio b/a the kinetics parameter converges to the kinetics parameter of a plane adsorbent sheet, see App. A.4. This confirms the validity of the approach also for rectangular channels of higher aspect ratio.

4.2.5. Constitutive Equations

The parameter values and functions of the MCM are identical with the parameters of the SCM discussed in Sect. 4.1.5 and summarized in App. B.

4.2.6. Controller Equation

As mentioned in Sect. 4.2.1, the thermal power of the adsorber can be controlled by varying the inlet pressure over time. For this purpose, a controller equation is required. The implementation of a standard proportional-integral-derivative controller (PID-controller, e. g. [116]) would be suited. However, restrictions by the time-integration solver applied in this thesis do not allow for the implementation of a PID-controller, see Sect. 5.2.1. Nevertheless, the implementation of an integral controller (I-controller) is straightforward. To overcome the usual dynamics limitation of an I-controller, an adaptive I-controller is designed. The controller equation reads

$$\frac{\partial p_{\mathrm{in}}}{\partial t} = \min\Big(K_{\mathrm{I},1}\left(p_{\mathrm{in,max}} - p_{\mathrm{in}}\left(t\right)\right); K_{\mathrm{I},2}\left(p_{\mathrm{th,set}} - p_{\mathrm{th}}\left(t\right)\right)\Big), \tag{4.53}$$

where $K_{\mathrm{I},1}$ and $K_{\mathrm{I},1}$ denote the controller parameters, $p_{\mathrm{in,max}}$ is the maximum inlet pressure, p_{th} denotes the volumetric thermal power output of the adsorber and $p_{\mathrm{th,set}}$ refers to the set point value of the volumetric thermal power.

The controller contains two controller equations. The first equation defines a pressure regulated controller and the second equation defines a power regulated controller. Initially, the pressure regulated controller is effective, leading to a fast increase of the inlet pressure. As soon as the thermal power is close to the set point value $p_{\mathrm{th,set}}$, the power regulated controller applies, strongly reducing the increase rate of the pressure, and thus avoiding a significant overshoot of the controlled power. The controller is found to be robust and only of low sensitivity to variation of the controller parameters. As suitable controller parameters the values $K_{\mathrm{I},1} = 10^{-4}\,1/\mathrm{s}$ and $K_{\mathrm{I},2} = 10^{-1}\,(\mathrm{m}^3\,\mathrm{Pa})/(\mathrm{W\,s})$ are identified.

4.3. General Continuum Model

4.3.1. Approach and Assumptions

The closed low-pressure adsorber configuration examined by the GCM is is shown in Fig. 4.9. Except for the adsorbent configuration, the adsorber configuration is identical to the configuration examined by the MCM and described in Sect. 4.2.1. Here, besides honeycomb adsorbents, granules and powder adsorbents are also considered between the heat exchanger plates, see Fig. 1.4 in Sect. 1.2. In addition, the heat-up of the heat transfer fluid in the heat exchanger plates is now considered. The width of the inner gap of the heat exchanger plates is h_{htx} and the heat transfer fluid is assumed to be water.

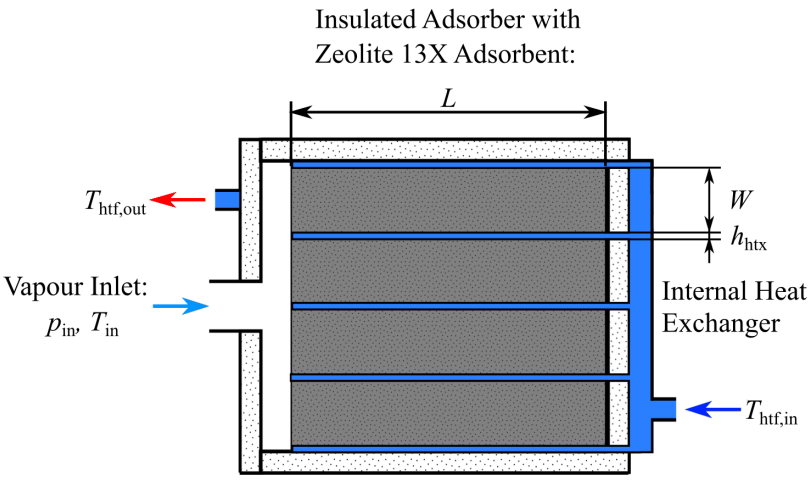

Figure 4.9.: Closed low-pressure adsorber configuration examined by the GCM. Honeycomb, granules or powder adsorbents are filled in between the parallel heat exchanger plates.

The discharging process is as described for the MCM, only that the heat-up of the heat transfer fluid in the heat exchanger plates is considered. Therefore, the surface temperature of the heat exchanger plates is no longer assumed uniform and constant. Instead, it is assumed that the heat transfer fluid distributes equally into the heat exchanger plates, flowing in the opposite direction to the vapor in the adsorbent bulk between the heat exchanger plates. While flowing through the heat exchanger plates, the heat transfer fluid heats up from an inlet temperature $T_{\mathrm{htf,in}}$ to an outlet temperature $T_{\mathrm{htf,out}}$, resulting in an increase of the surface temperature of the heat exchanger T_{htx} along the heat exchanger plates. Finally, to include this effect, the model has to be extended by a heat exchanger equation, that is the energy balance of the heat transfer fluid.

In the case of powder adsorbent, preliminary studies revealed that the high mass transport resistance in the powder bed limits the achievable temperature lift of the heat transfer fluid to $\Delta T_{\mathrm{htf}} < 10\,\mathrm{K}$. Therefore, only for this case, the adsorber configuration is slightly modified: plain vapor channels are integrated at the symmetry plane between the heat exchanger plates, allowing for an instant vapor supply along the whole length L of the adsorbent bed. By this modification, the maximum mass transport path is reduced from L to $W/2$, thus enhancing the thermal performance of the storage.

Following from the description above, it can be concluded that the mass and heat transport in each domain of adsorbent bulk between the heat exchanger plates are identical. Furthermore, the examined adsorber configuration leads to planar temperature and pressure fields. Assuming that the solution has the same symmetry as the geometry and the boundary conditions, the problem can be reduced to the analysis of one half-section of the adsorbent bulk between two parallel heat exchanger plates. The reduced problem is depicted in Fig. 4.10.

Regarding the mass transfer, the left boundary condition at the vapor inlet is

$$p(z=0) = p_{\mathrm{in}}(t). \tag{4.54}$$

For the modified adsorber configuration of the powder case as described above, the boundary condition (4.54) has to be applied to the symmetry plane instead of the left boundary. At all other boundaries the boundary condition for the mass transfer reads

$$\dot{m}_n = 0, \tag{4.55}$$

where $\dot{m}_n$ denotes the mass flux of the vapor normal to the boundary surface.

Regarding the heat transfer, a coupling condition at the heat exchanger plate couples the adsorbent with the heat transfer fluid. Since the thermal diffusivity of the metal casing of the heat exchanger plates (often copper) is higher by several orders of magnitude compared to both the adsorbent and the heat transfer fluid, the metal casing of the heat exchanger plate can be neglected. Hence, the local surface temperature is computed from the coupling condition

$$\dot{q}_{\mathrm{z},n}|_{\mathrm{htx}} = \dot{q}_{\mathrm{htf},n}|_{\mathrm{htx}}\,, \tag{4.56}$$

where $\dot{q}_{\mathrm{z},n}|_{\mathrm{htx}}$ and $\dot{q}_{\mathrm{htf},n}|_{\mathrm{htx}}$ denote the heat flux normal to the heat exchanger surface in the zeolite adsorbent bulk and in the heat transfer fluid. Applying Fourier's law to the heat flux in the

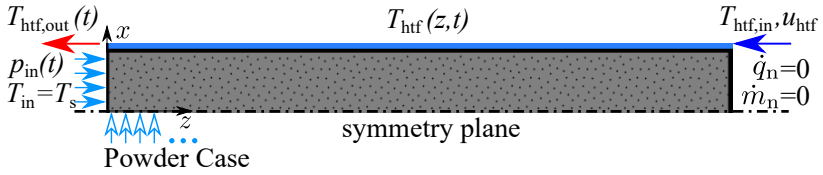

Figure 4.10.: Reduced problem: Half-section of the adsorbent bulk between two parallel heat exchanger plates with boundary conditions. The heat exchanger surface temperature T_{htx} is not constant but depends on the local temperature of the heat transfer fluid $T_{\mathrm{htf}}(z,t)$ in the heat exchanger plate.

adsorbent bulk and the equation for convective heat transfer to the heat flux in the heat transfer fluid, the coupling condition (4.56) yields

$$-\lambda_{\mathrm{eff},x}\frac{\partial T}{\partial x}\bigg|_{\mathrm{htx}} = \alpha_{\mathrm{htf}}\left(T_{\mathrm{htx}} - T_{\mathrm{htf}}\right), \tag{4.57}$$

with the effective heat conductivity $\lambda_{\mathrm{eff},x}$ of the adsorbent bulk in x-direction and α_{htf} as the convective heat transfer coefficient for the heat transfer fluid. At all other boundaries the boundary condition for the heat transfer reads

$$\dot{q}_n = 0, \tag{4.58}$$

where $\dot{q}_n$ denotes the heat flux normal to the boundary surface.

Finally, the temperature of the heat transfer fluid at the heat exchanger entrance is

$$T_{\mathrm{htf}}(z = L) = T_{\mathrm{htf,in}}, \tag{4.59}$$

while the mean velocity of the heat transfer fluid is set to u_{htf}.

The initial conditions for the adsorbent bulk and the heat transfer fluid are set to a uniform state of equilibrium

$$p(t=0) = p_0, \qquad T(t=0) = T_0, \qquad X(t=0) = X_{\mathrm{eq}}\left(p_0,\, T_0\right), \qquad T_{\mathrm{htf}}(t=0) = T_0. \tag{4.60}$$

In summary, given the boundary conditions by Eq. (4.54) to Eq. (4.59) as well as the initial conditions (4.60), the three dependent variables pressure $p\left(\boldsymbol{x}, t\right)$, temperature $T\left(\boldsymbol{x}, t\right)$ and water uptake $X\left(\boldsymbol{x}, t\right)$ are computed for the adsorbent bulk, where $\boldsymbol{x} = (z, x)$ denotes the vector of the coordinates. In comparison to the MCM, the temperature of the heat transfer fluid $T_{\mathrm{htf}}(z, t)$ along the heat exchanger plate is also computed. Finally, the assumptions listed for the SCM at the end of Sect. 4.1.1 are also applied to the GCM.

4.3.2. Balance Equations

As described for the SCM in Sect. 4.1.1, the governing equations for the pressure and temperature are derived from the mass balance equation for the compressible vapor as well as from the energy balance equation for the vapor, the adsorbent and the adsorbate. However, the balance equations are now formulated for an infinitesimal volume of the adsorbent bulk in three-dimensional space. Note that at this state no specification of the adsorbent configuration is required. To close the system of balance equations, transport equations for the mass and heat flux $\dot{\boldsymbol{m}}$ and $\dot{\boldsymbol{q}}$ discussed in the subsequent Sect. 4.3.3 are incorporated. Again, to derive the governing equation for the water uptake the LDF approximation is applied. Finally, applying the same procedure as described for the SCM, the balance equations yield a system of coupled PDEs which can be written as

$$\begin{pmatrix} \dfrac{\varepsilon}{R_{\mathrm{s}}}\dfrac{1}{T} & -\dfrac{\varepsilon}{R_{\mathrm{s}}}\dfrac{p}{T^2} & \rho_{\mathrm{b}} \\ 0 & \rho_{\mathrm{b}}\Big(c_{\mathrm{z}} + X c_{\mathrm{a}}\Big) & -\rho_{\mathrm{b}}\Big(\Delta h_{\mathrm{a}} - R_{\mathrm{s}} T\Big) \\ 0 & 0 & 1 \end{pmatrix} \cdot \begin{pmatrix} \dfrac{\partial p}{\partial t} \\ \dfrac{\partial T}{\partial t} \\ \dfrac{\partial X}{\partial t} \end{pmatrix} = \begin{pmatrix} -\nabla \cdot \dot{\boldsymbol{m}} \\ -\nabla \cdot \dot{\boldsymbol{q}} - \dot{\boldsymbol{m}} c_{p,\mathrm{v}} \cdot \nabla T - R_{\mathrm{s}} T \nabla \cdot \dot{\boldsymbol{m}} \\ k_{\mathrm{a}}\left(X_{\mathrm{eq}} - X\right) \end{pmatrix}, \tag{4.61}$$

where ∇ denotes the nabla operator and ρ_{b} defines the adsorbent bulk density as

$$\rho_{\mathrm{b}} = (1 - \varepsilon)\,\rho_{\mathrm{z}}. \tag{4.62}$$

Note that in [109] the system of balance equations is presented in a slightly different form. However, by incorporating the mass balance equation into the energy balance equation, the two systems can be transformed to each other and therefore are equivalent.

4.3.3. Transport Equations

Mass Transport

Considering the vapor as a viscous Newton-fluid and assuming creeping flow in the adsorbent bulk (Stokes flow, $Re \ll 1$), Darcy's law can be applied to determine the mass flux, both for packed bed and honeycomb adsorbents. The local form of Darcy's law reads

$$\dot{\boldsymbol{m}} = -\boldsymbol{\kappa} \cdot \frac{\rho_\mathrm{v}}{\mu} \nabla p, \tag{4.63}$$

where $\boldsymbol{\kappa}$ denotes the permeability tensor. As described in the fundamentals in Sect. 2.2.1 the permeability becomes dependent on the Knudsen number with decreasing pressure or decreasing pore size of the porous medium.

To derive the Knudsen dependency of the permeability, an abstract but simple model for a porous medium is applied as e. g. in [95]. In this model, the porous medium is considered as a medium with cylindrical, tortuous channels of diameter d_c representing the pore space of the porous medium. Therefore, the same modeling approach for the channel flow as in the SCM, see Sect. 4.1.3, can be applied. Neglecting the thermal creep effect and introducing the Knudsen number and dynamic viscosity to Eq. (4.24), the mean velocity in a representative cylindrical channel at any Knudsen number can be calculated from

$$u_\mathrm{c} = -\frac{d_\mathrm{c}^2}{32} \frac{1}{\mu} \frac{1}{\tau} \frac{\partial p}{\partial z} \Phi(Kn), \tag{4.64}$$

with

$$\Phi(Kn) := \frac{8}{\sqrt{\pi}} Kn G_\mathrm{P}(Kn), \tag{4.65}$$

where τ denotes the tortuosity of the porous medium, see Sect. 2.2.1. The defined function $\Phi(Kn)$ describes the Knudsen dependency through the Poiseuille coefficient G_P given by Eq. (4.25). For $Kn \to 0$ it follows $\Phi(Kn) \to 1$ and Eq. (4.64) reduces to the Hagen-Poiseuille Eq. (2.15).

With the mean velocity in the representative channels the mass flux can be determined from

$$\dot{m} = \frac{\varepsilon}{\tau} \rho_\mathrm{v} u_\mathrm{c}. \tag{4.66}$$

Comparison with Darcy's law (4.63) for the one-dimensional case yields

$$\kappa_z = \frac{\varepsilon}{\tau^2} \frac{d_\mathrm{c}^2}{32} \Phi(Kn) = \kappa_0 \Phi(Kn). \tag{4.67}$$

Again, for $Kn \to 0$ it follows $\Phi(Kn) \to 1$. Hence, κ_0 denotes the permeability in the continuum regime, while $\Phi(Kn)$ can be defined as the non-dimensional Knudsen permeability correction factor describing the Knudsen dependency of the permeability, compare e. g. [96].

For the case of a honeycomb adsorbent with straight square channels the tortuosity is $\tau = 1$ and the hydraulic diameter is equal to the channel width $d_\mathrm{c} = a$. In this case, the permeability component in channel direction can be calculated directly from Eq. (4.67), that is $\kappa_\mathrm{hc} = \kappa_z$. The permeability component normal to the channels can be assumed to $\kappa_x = 0$.

For the case of a packed bed of granules or powder adsorbent, the hydraulic diameter has to be determined first to evaluate Eq. (4.67). For $Kn \leq 0.01$ the well-known Carman-Kozeny equation

$$\kappa_\mathrm{CK} = \frac{1}{180} \frac{\varepsilon^3}{(1-\varepsilon)^2} d_\mathrm{p}^2 \tag{4.68}$$

is valid, where d_p denotes the mean particle diameter, see Sect. 2.2.1. Comparing Eq. (4.68) with Eq. (4.67) for $Kn \to 0$ ($\Phi(Kn) \to 1$) gives the hydraulic diameter of a packed bed

$$d_\mathrm{c,pb} = \sqrt{\frac{16}{45}} \frac{\varepsilon}{1-\varepsilon} d_\mathrm{p}. \tag{4.69}$$

Reintegrating this result (4.69) into Eq. (4.67) yields

$$\kappa_{\mathrm{pb}} = \kappa_{\mathrm{CK}} \Phi(Kn) = \kappa_0 \Phi(Kn), \tag{4.70}$$

where κ_{CK} denotes the permeability determined by the Carman-Kozeny Eq. (4.68), which is valid for $Kn \leq 0.01$. Thus, the permeability of a packed bed with $Kn \geq 0.01$ can simply be calculated by multiplying the permeability determined by the Carman-Kozeny Eq. (4.68) with the Knudsen permeability correction factor $\Phi(Kn)$ given in Eq. (4.65).

To compare the permeability of a packed bed adsorbent, that is granules or powder adsorbents, to the permeability of a honeycomb adsorbent, Eq. (4.70) is simply divided by Eq. (4.67), giving

$$\frac{\kappa_{\mathrm{pb}}}{\kappa_{\mathrm{hc}}} = \frac{32}{180} \frac{\varepsilon_{\mathrm{pb}}^3}{\varepsilon_{\mathrm{hc}} \left(1 - \varepsilon_{\mathrm{pb}}\right)^2} \left(\frac{d_{\mathrm{p}}}{d_{\mathrm{c}}}\right)^2. \tag{4.71}$$

For random packed beds, a porosity of $\varepsilon_{\mathrm{pb}} = 0.4$ is usually applied. Since honeycombs allow for lower porosity values in general, a honeycomb porosity of $\varepsilon_{\mathrm{hc}} = 0.\bar{1}$ is assumed in Fig. 4.11 (a). The curves show that for these porosity values, identical permeabilities are achieved if the diameter of the packed bed particles is around two times the channel diameter of the honeycomb. This result agrees with the prediction found in literature that honeycombs offer a better mass transport in comparison to packed beds, e. g. [20]. Moreover, the curves reveal that powder adsorbents with $d_{\mathrm{p}} \leq 100\,\mu\mathrm{m}$ lead to permeability values several orders of magnitude lower compared to honeycombs. Hence, this confirms the necessity of the modification of the adsorber configuration for powder adsorbents as described in Sect. 4.3.1.

Finally, the derived Knudsen dependency of the permeability should be analyzed in terms of the Knudsen permeability correction factor as defined in Eq. (4.65). Note that the Knudsen permeability correction factor is identical for both honeycomb and packed bed. The evolution of the Knudsen permeability correction factor $\Phi(Kn)$ over the Knudsen number Kn is shown in Fig. 4.11 (b). The Knudsen permeability correction factor increases with the Knudsen number and starts to deviate significantly from the permeability value of the continuum regime already in the slip regime $0.01 \leq Kn \leq 0.1$. However, it should be emphasized that while the permeability increases with the Knudsen number, the mass flux according to Eq. (4.63) decreases. This is explained by the fact that high Knudsen numbers only occur for either low pressure or small pore space of the porous medium, which corresponds to low particle diameters in packed beds. Low pressure constitutes low vapor density as well as low pressure gradients, both reducing the mass flux. Furthermore, according to Eq. (4.68) low particle diameters significantly reduce the permeability as well.

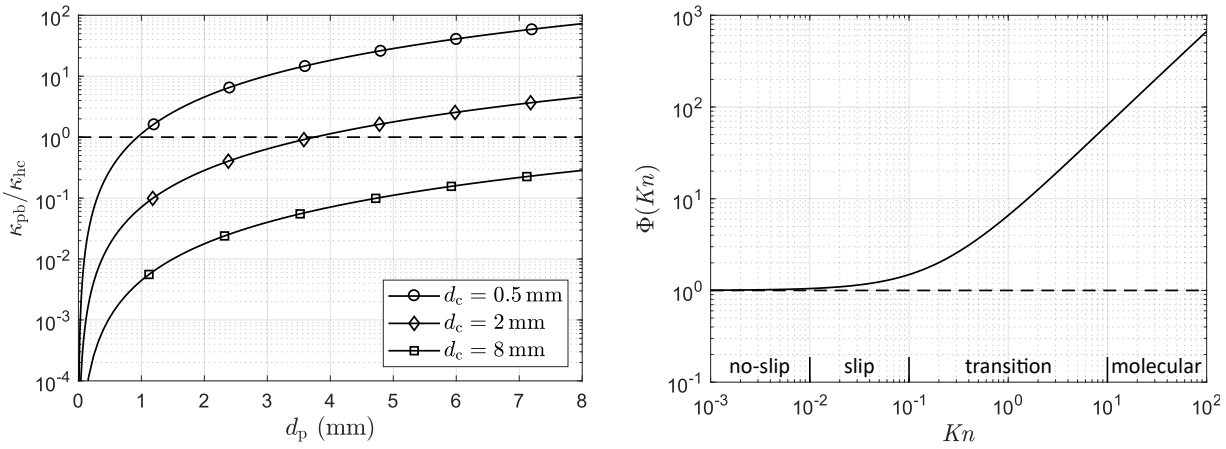

(a) Permeability ratio $\kappa_{\mathrm{pb}}/\kappa_{\mathrm{hc}}$ of packed beds to honeycombs versus particle diameter d_{p} for different channel diameters d_{c} and the porosities $\varepsilon_{\mathrm{pb}} = 0.4$, $\varepsilon_{\mathrm{hc}} = 0.\bar{1}$.

(b) Model prediction of the Knudsen permeability correction factor $\Phi(Kn)$ according to Eq. (4.65) versus Knudsen number Kn.

Figure 4.11.: Permeability ratio $\kappa_{\mathrm{pb}}/\kappa_{\mathrm{hc}}$ and Knudsen permeability correction factor $\Phi(Kn)$.

Heat Transport

The heat flux in a continuum is described by Fourier's law. Under the assumption of local thermal equilibrium, the law is also applicable to porous media applying an effective heat conductivity

$$\dot{\boldsymbol{q}} = -\boldsymbol{\lambda}_{\text{eff}} \nabla T. \tag{4.72}$$

In general, the effective heat conductivity $\boldsymbol{\lambda}_{\text{eff}}$ is a non-isotropic tensor. Comparison with the mass flux Eq. (4.63) reveals the analogue mathematical structure of the mass and heat flux. However, in comparison to the permeability, the effective heat conductivity cannot be separated further into strictly material and geometry dependent parameters. Nevertheless, similar to the permeability as in Eq. (4.67), the effective heat conductivity can be formally separated into the effective heat conductivity for the continuum region $\lambda_{\text{eff},0}$ and a non-dimensional Knudsen dependent function

$$\lambda_{\text{eff}} = \lambda_{\text{eff},0} \Psi(Kn). \tag{4.73}$$

Similar to the Knudsen permeability correction factor $\Phi(Kn)$, the non-dimensional function $\Psi(Kn)$ is defined as the Knudsen heat conductivity correction factor. Note that in contrast to the permeability, both terms in Eq. (4.73) still depend on both material and geometry parameters as well as the temperature.

To determine the effective heat conductivity in the continuum regime, the geometry parameters, e. g. channel or particle diameter and the heat conductivities of the vapor and the adsorbent including the adsorbate and interstitial vapor, are required. The latter is summarized in the effective heat conductivity of the zeolite adsorbent $\lambda_{\text{z,eff}}(X)$ and is discussed in detail for the SCM in Sect. 4.1.3.

With the effective heat conductivity of the zeolite adsorbent, the effective heat conductivity of the adsorbent bulk can be determined. For a honeycomb adsorbent the simple thermal resistance model as described for the SCM and MCM is applied, that is Eq. (4.29) in Sect. 4.1.3 for $\lambda_{\text{eff},z}$ and Eq. (4.51) in Sect. 4.2.3 for $\lambda_{\text{eff},x}$. It is found that the Knudsen dependency is negligible for honeycomb adsorbents due to the continuous solid phase. Hence, for a honeycomb adsorbent the Knudsen heat conductivity correction factor is $\Psi(Kn) \equiv 1$ and $\lambda_{\text{eff}} \equiv \lambda_{\text{eff},0}$.

Regarding the effective heat conductivity of packed beds, numerous models have been published, compare e. g. [41, 42]. However, only few models exist which also account for the Knudsen dependency. Here, we apply the well-known and validated Zehner-Bauer-Schlünder model (ZBS model) as described in [112, 41] and originally described in [43] and [44]. The main equation is an extensive function of the form

$$\lambda_{\text{eff}} = \text{fct}\left(\lambda_{\text{v}}(Kn), \lambda_{\text{z,eff}}(X), \varepsilon, d_{\text{p}}, \varphi, T, \epsilon\right), \tag{4.74}$$

where φ refers to an empirical fitting parameter to account for the finite contact area of the particles and ϵ is the emission coefficient for thermal radiation of the zeolite adsorbent. According to [117, 118], the emission coefficient for zeolite adsorbents is $\epsilon = 0.89$. Since thermal dispersion can be neglected ($Re \ll 1 \rightarrow Pe \ll 1$), the effective heat conductivity is independent from the vapor velocity.

The Knudsen dependency of the effective heat conductivity of a packed bed is a result of the Knudsen dependency of the heat conductivity of the interstitial vapor in the wedge-shaped gap around the contact area of two particles. The mean heat conductivity of the interstitial vapor in this gap region is calculated from

$$\lambda_{\text{v}}(Kn) = \lambda_{\text{v},0} \left(1 + l^*_{\text{mol}} \frac{d_{\text{c,pb}}/2}{d_{\text{p}}} Kn\right)^{-1}, \tag{4.75}$$

where l^*_{mol} denotes the modified mean free path of the vapor molecules, which reads

$$l^*_{\text{mol}} = \frac{2 - \alpha_T}{\alpha_T} \frac{\lambda_{\text{v},0}}{\mu} \frac{1}{2c_{\text{v},p} - R_{\text{s}}}. \tag{4.76}$$

To compare the effective heat conductivity of a packed bed to that of a honeycomb, the ratio of the conductivities in the continuum regime is given in Fig. 4.12 (a). As mentioned above, the effective heat conductivity of a honeycomb is independent of the Knudsen number, that is $\Psi_{\mathrm{hc}}(Kn) \equiv 1$. Hence, the ratio of the heat conductivities for any Knudsen number is equal to the ratio of the conductivities in the continuum regime multiplied with the Knudsen heat conductivity correction factor $\Psi_{\mathrm{pb}}(Kn)$ of a packed bed. For the figure, the porosity values are defined as before in Fig. 4.11, that is $\varepsilon_{\mathrm{pb}} = 0.4$ for the packed bed and $\varepsilon_{\mathrm{hc}} = 0.\bar{1}$ for the honeycomb. The figure shows that the conductivity ratio is lower than one in most states, that is the effective heat conductivity of a packed bed is lower than of a honeycomb. The variation with the particle diameter results from the point contact density of the adsorbent particles, which reduces with increasing particle diameter. Note that the ratio is independent of the channel diameter of the honeycomb. What is more, the figure shows that the ratio also depends on the temperature and water uptake, where the depicted curves mark the upper and lower bounds. The upper bound is only relevant for the charging process where high temperatures and low water uptake occur.

The resulting Knudsen dependency of the effective heat conductivity of a packed bed is given by the Knudsen heat conductivity correction factor $\Psi_{\mathrm{pb}}(Kn)$. The result for the studied binderless zeolite 13X in a water vapor atmosphere at 20 °C is shown in Fig. 4.12 (b). The fitting parameter for the finite contact area of the particles is determined to $\varphi = 0.0035$ by calibration with experimental results, discussed in the subsequent Sect. 4.4. In general, the fitting parameter should lie in the range of $0.001 \ldots 0.01$. Variation of the fitting parameter in this range shows only little dependency of $\Psi_{\mathrm{pb}}(Kn)$ for the examined zeolite adsorbent. In contrast to the permeability, see Fig. 4.11 (b), the effective heat conductivity decreases with increasing Knudsen number for $Kn \geq 0.01$. As mentioned above, the correction factor for the effective heat conductivity still depends on the particle geometry in terms of particle diameter as well as on the temperature. The dependency of the conductivity on the particle diameter is found to be significant for $Kn \geq 0.1$. Furthermore, comparison with the no-radiation case indicates that for $Kn \geq 0.1$ the thermal radiation is important even for low temperatures. Only for the case of fine powder adsorbent with $d_{\mathrm{p}} \leq 100\,\mu\mathrm{m}$ the results are found to be almost independent of radiation and well approximated by the no-radiation case. As an example, the temperature is varied for the case with a particle diameter of $d_{\mathrm{p}} = 2\,\mathrm{mm}$, showing a significant dependency of the effective heat conductivity on the temperature for higher Knudsen numbers. The temperature dependency can also be attributed to thermal radiation. In summary, the effective heat conductivity increases with particle diameter and temperature for $Kn \geq 0.1$.

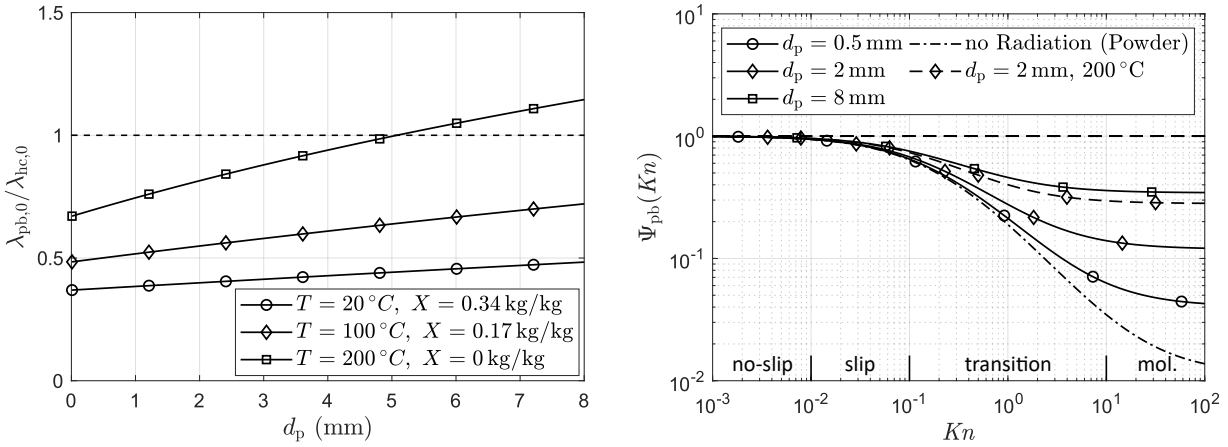

(a) Ratio of the effective conductivities of packed bed and honeycomb in the continuum regime versus particle diameter for varying temperature and water uptake.

(b) Model prediction of the Knudsen heat conductivity correction factor $\Psi_{\mathrm{pb}}(Kn)$ for packed beds versus Kn-number at 20 °C for different particle diameters.

Figure 4.12.: Effective heat effective conductivity ratio $\lambda_{\mathrm{pb},0}/\lambda_{\mathrm{hc},0}$ in the continuum regime and Knudsen heat conductivity correction factor $\Psi_{\mathrm{pb}}(Kn)$ for packed beds.

4.3.4. Adsorption Equations

The adsorption equilibrium X_{eq}, the adsorption enthalpy Δh_{a} and the adsorption kinetics parameter k_{a} are calculated by the equations given for the SCM and MCM in Sect. 4.1.4 and 4.2.4. The adsorption kinetics parameter for granules and powder adsorbents reads

$$k_{\mathrm{a}} = D_{\mathrm{eff}} \frac{60}{d_{\mathrm{p}}^2}. \tag{4.77}$$

4.3.5. Constitutive Equations

The parameter values and functions of the GCM are identical to the parameters of the SCM discussed in Sect. 4.1.5 and summarized in App. B.

4.3.6. Controller Equation

As mentioned in Sect. 4.2.1 for the MCM, the thermal power of the adsorber can be controlled by varying the inlet pressure over time. In comparison to the MCM, the GCM allows for the more practical control of the outlet temperature of the heat transfer fluid. For this purpose, a controller equation is required. The design of the controller is analog as for the MCM and described in Sect. 4.2.6. The controller equation reads

$$\frac{\partial p_{\mathrm{in}}}{\partial t} = \min\Big(K_{1,1} \left(p_{\mathrm{in,max}} - p_{\mathrm{in}}(t) \right) ; K_{1,2} \left(T_{\mathrm{htf,out,set}} - T_{\mathrm{htf,out}}(t) \right) \Big). \tag{4.78}$$

As suitable controller parameters the values $K_{\mathrm{I},1} = 10^{-4}\,1/\mathrm{s}$ and $K_{\mathrm{I},2} = 10^{-1}\,(\mathrm{Pa}/(\mathrm{K\,s})$ are identified. For a few of the studied cases (high channel or particle diameter) as well as for the powder adsorbent the controller parameters have to be slightly modified. The modifications are discussed with the results in Sect. 6.3.4.1.

4.3.7. Heat Exchanger Equation

To complete the model description, the governing equation for the heat exchanger is required. The governing equation for the temperature distribution in the heat transfer fluid along the heat exchanger plate $T_{\mathrm{htf}}(z,t)$ is derived from the energy balance Eq. (2.10). Since the heat transfer fluid (water) can be assumed incompressible, the formulation of the mass balance equation is not required. The energy balance reads

$$\rho_{\mathrm{htf}} c_{\mathrm{htf}} \frac{\partial T_{\mathrm{htf}}}{\partial t} = \frac{\partial}{\partial z} \left(\lambda_{\mathrm{htf}} \frac{\partial T_{\mathrm{htf}}}{\partial z} \right) - \dot{m}_{\mathrm{htf}} c_{\mathrm{htf}} \frac{\partial T_{\mathrm{htf}}}{\partial z} + \frac{1}{h_{\mathrm{htx}}} 2\, \dot{q}_{\mathrm{htf},n}|_{\mathrm{htx}}\,, \tag{4.79}$$

where ρ_{htf} denotes the density, c_{htf} the specific heat capacity and λ_{htf} the heat conductivity of the heat transfer fluid. These parameters are calculated according to the VDI heat atlas [112] and summarized in App. B. The mass flux in the heat exchanger plate is given by $\dot{m}_{\mathrm{htf}} = \rho_{\mathrm{htf}} u_{\mathrm{htf}}$ with u_{htf} as the mean velocity of the heat transfer fluid in the heat exchanger gap. The heat source term results from the coupling with the adsorbent bulk by the coupling condition (4.56). Since the heat exchanger plate is in contact with the adsorbent bulk on both sides, the heat flux from the adsorbent into the heat transfer fluid has to be accounted for twice. As already discussed in Sect. 4.3.1, the heat flux is calculated from the equation for convective heat transfer

$$\dot{q}_{\mathrm{htf},n}|_{\mathrm{htx}} = \alpha_{\mathrm{htf}} \left(T_{\mathrm{htx}} - T_{\mathrm{htf}} \right). \tag{4.80}$$

Assuming laminar flow of the heat transfer fluid, the convective heat transfer coefficient α_{htf} can be determined according to the procedure described in the VDI heat atlas [112], see App. B. The values for the convective heat transfer coefficient vary around $\alpha_{\mathrm{htf}} \approx 800\,\mathrm{W}/(\mathrm{m}^2\mathrm{K})$.

4.4. Model Validation

The validation of the derived models only regards the transport equations for the mass and heat flux. Since the balance equations are fundamental physical laws, no validation is required. Further, the implemented constitutive equations are taken from the VDI heat atlas [112] and thus can be assumed valid. The implemented adsorption equations have been validated in [16].

To validate the mass transport model, the derived Knudsen dependency of the permeability should be validated. Since both, the Hagen-Poiseuille and the Carman-Kozeny equation have been validated for the continuum regime ($Kn \leq 0.01$) [33], it is sufficient to examine the Knudsen permeability correction factor $\Phi(Kn)$ as defined in Eq. (4.65). The Knudsen permeability correction factor together with experimental results of three independent studies is shown in Fig. 4.13 (a). One experimental study examined the flow of nitrogen through a straight cylindrical micro tube [119]. Thus, the experimental results of this study are comparable to the flow of a rarefied gas through a honeycomb. Another experiment studied the flow of nitrogen at low pressures ($p \leq 20\,\mathrm{mbar}$) through a packed bed of glass beads with a particle diameter of $d_\mathrm{p} = 2\,\mathrm{mm}$ [120]. For the latter study the results are given by the mean Darcy velocity, but comparison with the analytic prediction of Darcy's law showed that the given experimental results are too high by exactly one order of magnitude. The author confirmed that all values applied to evaluate Darcy's law are correct. Therefore, a typing error in the annotation of the axis can be assumed and the experimental values are corrected by one order of magnitude. Thirdly, some values of a broad experimental study on flow through sandstone are reproduced from [96]. The experimental results show good agreement with the model prediction. Thus, the mass transport model can be assumed valid.

To validate the heat transport model, the derived Knudsen dependency of the effective heat conductivity should be validated for a packed bed of a zeolite adsorbent. Since Fourier's law can be assumed valid, it is sufficient to examine the Knudsen heat conductivity correction factor $\Psi(Kn)$. The Knudsen heat conductivity correction factor together with the results from an experimental study [117, 118] are shown in Fig. 4.13 (b). The experiment examined a fine zeolite 4A powder with a mean particle diameter of $d_\mathrm{p} = 4.3\,\mu\mathrm{m}$ and a porosity of $\varepsilon = 0.65$ in a nitrogen atmosphere. Good agreement is achieved in the no-slip, slip and molecular regime. In the transition regime the model underestimates the effective heat conductivity by slightly more than 30%. Considering this deviation, the heat transport model can be assumed to be valid.

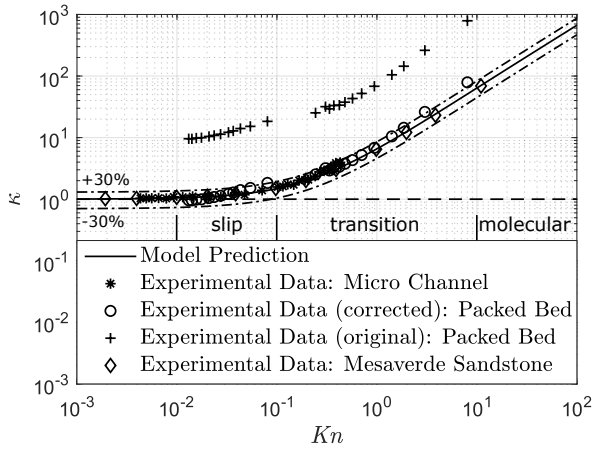

(a) Model prediction of the Knudsen permeability correction factor $\Phi(Kn)$ according to Eq. (4.65) versus Knudsen number Kn together with experimental results of three independent studies [119, 120, 96].

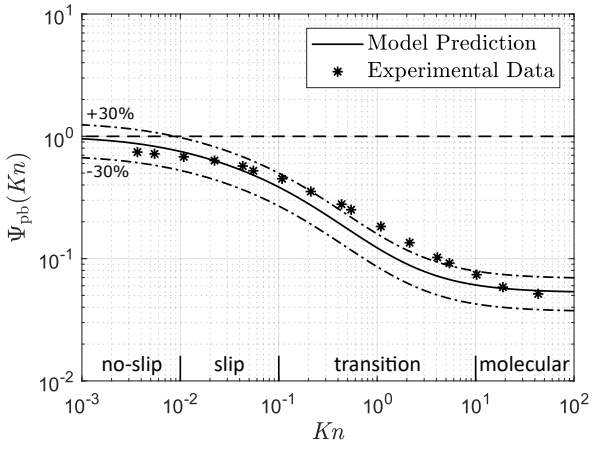

(b) Model prediction of the Knudsen heat conductivity correction factor $\Psi_\mathrm{pb}(Kn)$ versus Knudsen number Kn for fine zeolite 4A powder in a nitrogen atmosphere together with experimental results from [117].

Figure 4.13.: Comparison of the model prediction and experimental results for the mass and heat transport in terms of Knudsen permeability and heat conductivity correction factors.

5. Numerical Implementation

The SCM, MCM and GCM are described by systems of coupled non-linear PDEs, see Eq. (4.21), (4.43) and (4.61). Hence, it is relatively difficult or even impossible to derive analytical solutions. For simplified special cases (reduction of dimensions and/or variables, decoupling of equations etc.) analytical solutions could be derived, e. g. [67]. However, the full systems of governing equations of the SCM, MCM and GCM have to be solved numerically.

In general, to solve systems of PDEs, discretization methods such as the Finite Difference, Finite Volume and Finite Element Method are applied, e. g. [121]. Here, the Finite Difference Method (FDM) is applied, since it allows for a straightforward implementation. The spatial discretization is manually programmed in Matlab, whereas an available Matlab solver is used for the time integration. The discretization and time integration are described in the following.

5.1. Spatial Discretization

5.1.1. Mesh Generation and Adaption

The problem domains of the reduced problems studied by the SCM, MCM and GCM are either a straight one-dimensional line or a two-dimensional rectangle, see Fig. 4.2, 4.7 and 4.10. Thus, the deployment of a structured grid suggests itself. Regarding the knot spacing, a constant and uniform knot spacing Δz and Δx for each spatial direction is applied for the MCM and GCM.

However, for the SCM an adaptive mesh refinement (AMR) procedure is developed and implemented. The AMR allows for a dynamic and local reduction of the knot spacing while other parts of the mesh remain at a higher knot spacing. By this, the total number of computed knots can be reduced significantly, which in turn reduces the computational time. The motivation to apply an AMR for the SCM, results from the aim to conduct a broad parameter study leading to several hundred cases to be simulated [107]. Note that for a more comprehensive discussion of the simulation results of the SCM only a reduced number of cases is discussed in this work, see Sect. 6.1.1.

In general, the mesh is dynamically refined in regions, which require a higher precision. Typically, these regions correspond to the regions of high gradients. Therefore, the implemented criteria for the mesh adaption are the maximum allowed differences of temperature and pressure values between two neighboring knots. The maximum allowed differences are set to

$$\Delta T \leq 1\,\mathrm{K} \quad \Delta p \leq 50\,\mathrm{Pa}.$$

The values for the maximum allowed differences are derived from test simulations and convergence studies. Furthermore, the test simulations revealed that the AMR is stronger determined by the temperature than by the pressure evolution. In addition, the aspect ratio of the knot spacing of neighboring knots is limited to two and the knot spacing at the boundaries is fixed to the initial and minimum knot spacing Δz_{min}. Finally, to adapt the mesh, the time integration has to be interrupted. The implemented control for the time step of the mesh adaption is discussed in Sect. 5.2.2. Further, the AMR includes a predictive mesh refinement since the regions of high gradients move during the finite time step of the mesh adaption. As an example, the adapted mesh at a specific instant of time ($\tilde{t} = 0.1\%$, see Eq. (6.1)) for a reference case of the SCM (see Tab. 6.1), together with the corresponding temperature profile T versus the channel length z is shown in Fig. 5.1. Each vertical line marks the position of a knot. The figure confirms that the mesh is refined in the regions of high temperature gradient.

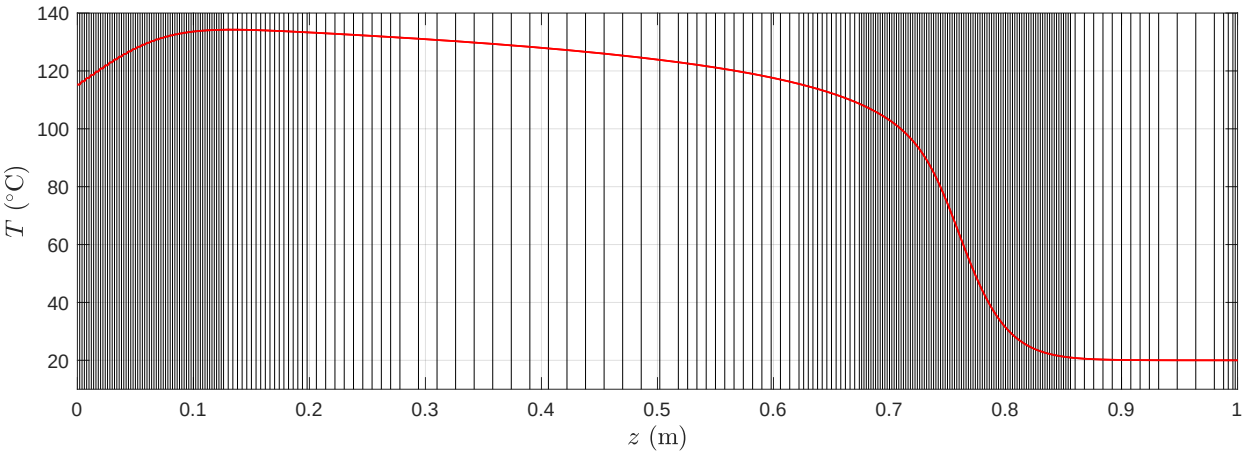

Figure 5.1.: Adapted mesh at a specific instant of time ($\tilde{t} = 0.1\%$, see Eq. (6.1)) for a reference case of the SCM (see Tab. 6.1) together with the corresponding temperature profile T versus the channel length z. Each vertical line marks the position of a knot.

To evaluate the effect of the implemented AMR, the computational time for the reference case of the SCM (see Tab. 6.1) is determined with and without AMR. The dependency of the required computational times on the inverse knot spacing, given by the knots per channel length L, is shown in Fig. 5.2. Note that in the case of implemented AMR, the given knot spacing only corresponds to the minimum allowed knot spacing while higher knot spacings can result from the mesh adaption, thus reducing the total number of knots. The computational times yield the typical non-linear increase with increasing number of knots, that is with decreasing knot spacing. In comparison, the cases without AMR lead to slightly lower computational times for less than 100 knots/L. However, in this range the computational times are relatively low already. For more than 100 knots/L, the AMR provides lower computational times. Due to the non-linear increase of the computational times, the acceleration of the computation by the AMR increases with the number of knots. For 1000 knots/L the AMR leads to a reduction of the computational time by 75%. For other cases studied by the SCM, the reduction can even reach up to 90%.

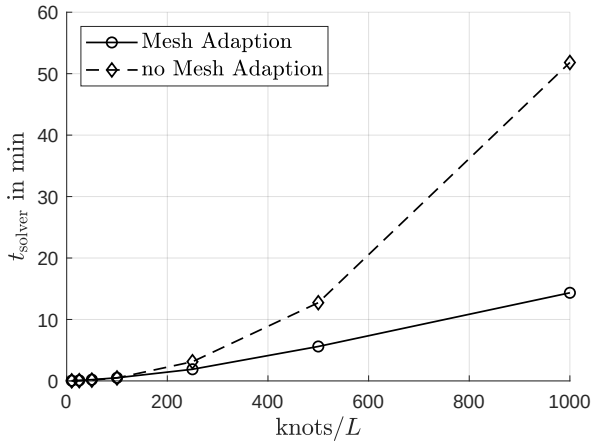

Figure 5.2.: Dependency of the required computational times on the knots per channel length L (equivalent to the inverse knot spacing) with and without AMR for the reference case of the SCM, see Tab. 6.1.

5.1.2. Mesh Convergence

To determine the required knot spacing for sufficient accuracy of the numerical results, mesh convergence studies are conducted for representative cases of the SCM, MCM and GCM. Suitable results to analyze the mesh convergence are the maximum temperature and the time required for the vapor to reach the closed end of the adsorber. The latter is defined as the time at which the pressure at the closed end has increased to 10% of the inlet pressure: $p(z = L) = 0.1p_{\text{in}}$. As an example, the mesh convergence of the reference case of the SCM (see Tab. 6.1) is discussed here. The results of the convergence study for $T_{\max}$ and $t_{p,10}$ with and without AMR versus the number of knots per channel length N_z are shown in Fig. 5.3. Both results show the typical convergence behavior. However, the variation of the maximum temperature as well as the difference between the results determined with and without AMR are negligible, see Fig. 5.3. (a). With respect to the time required for the vapor to reach the closed end of the adsorber $t_{p,10}$, Fig. 5.3. (b) shows that the result is not converged for less than 100 knots/L. However, the result only slightly increases for more than 100 knots/L. Thus, 100 knots/L would already provide a quite accurate result. Nevertheless, $N_z = 500$ knots/L is set for the SCM to ensure accuracy for all studied cases. It should be emphasized that the required total number of knots does not scale with the channel length L, but the required knot spacing does scale with the channel length. The lower knot spacing is required for the cases of shorter channel length because these cases are of higher dynamic in general. Thus, $N_z = 500$ knots/L is also set for the cases with $L < 1$ m. Finally, the comparison with the cases simulated without AMR reveals that the AMR leads to a little off-set of 2.7% for $t_{p,10}$ in the examined case. However, this inaccuracy is acceptable as the examined process is mainly determined by the heat transport and not by the mass transport, see Sect. 6.1.5. For the other results examined for the mesh convergence study, the off-sets between the results determined with and without AMR are negligible.

With respect to the mesh convergence study of the MCM, it is found that $N_{\text{z}} = 250$ knots/L are sufficient, see App. C. For the GCM, $N_{\text{z}} = 100$ knots/L are applied as a good compromise between numerical accuracy and computational time, see App. C. Again, as for the SCM, the required number of knots does not scale with the adsorber length L. Note that no AMR is applied for both the MCM and GCM.

As mentioned before, the problem domain of the MCM and GCM is a two-dimensional rectangle. Therefore, a spatial discretization in the transversal direction is required. For the MCM, the knot

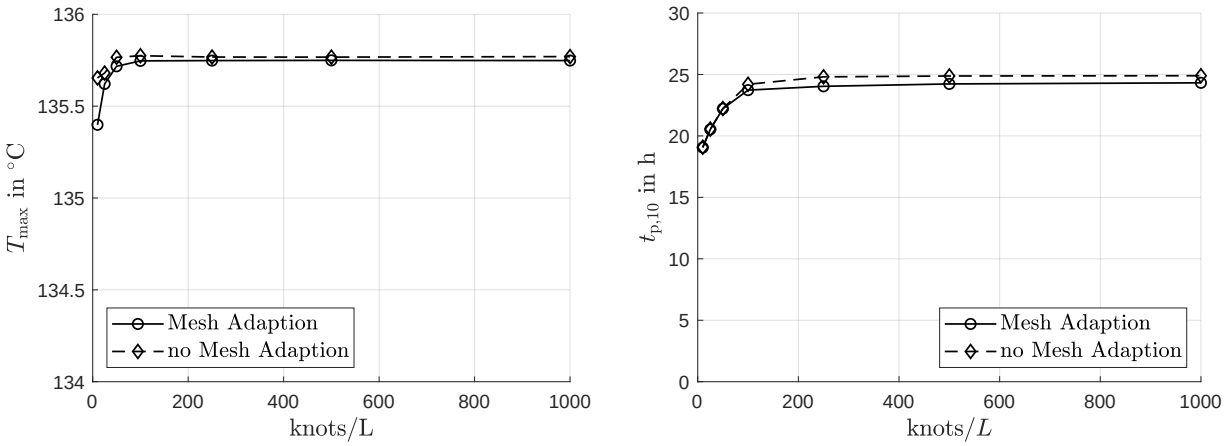

(a) Maximum temperature $T_{\max}$.

(b) Duration to reach the channel end $t_{p,10}$.

Figure 5.3.: Dependency of the maximum temperature $T_{\max}$ and of the time required for the vapor to reach the closed end of the adsorber $t_{p,10}$ on the number of knots per length N_z with and without AMR for the reference case of the SCM, see Tab. 6.2 .

spacing is determined by the discrete adsorbent channels and is equal to the outer height of each channel $\Delta x = (a + 2f)$ (respectively $\Delta y = (b + 2f)$ for a turned heat exchanger, see Fig. 4.6 (b)). As a consequence, accurate results can only be achieved for cases with an adequate number of channels, resulting in a small transversal knot spacing Δx in relation to the honeycomb width W. To evaluate whether the number of channels is adequate for achieving good numerical accuracy, a representative case with a minimum number of channels $N_\mathrm{c} = 4$ is simulated with first, second and third order approaches for the coupling heat flux terms. The results show no significant differences and thus it is appropriate to apply $N_x = N_\mathrm{c}$. Finally, with respect to the GCM, the spatial discretization in the transversal direction can be freely defined as the honeycomb is modeled as a continuum. It is found that a transversal discretization with $N_x = 8$ knots is sufficient for all studied cases, including the granules and powder cases, see App. C.

5.1.3. Approximation of Derivatives

As mentioned earlier, the FDM is applied to discretize the system of PDEs. The implemented discretization of the spatial derivatives is described in the following. Regarding the time derivatives, no manual discretization is required as a Matlab solver is employed for the time integration, see Sect. 5.2.1. In general, the spatial derivatives in the SCM, MCM and GCM are discretized by the Central-Difference-Approximation (CDA) which reads

$$\left.\frac{\partial Y}{\partial z}\right|_i \approx \frac{Y_{i+1} - Y_{i-1}}{2\Delta z}, \tag{5.1}$$

where Y denotes the unknown variable an i refers to the knot index. While the CDA is a first-order approximation, the related error is of second order: $\mathrm{err} = O(\Delta z^2)$. The CDA is applied to the spatial derivatives of the pressure p and temperature T. As the mass and heat flux $\dot{m}$ and $\dot{q}$ contain the spatial derivatives of the pressure and temperature, their differentiation would yield second-order as well as mixed derivatives of the pressure and temperature. This would require a second-order CDA. Instead, the CDA is directly applied to the spatial derivatives of the mass and heat flux. Finally, no spatial derivatives exist for the water uptake and the inlet pressure.

Applying the CDA to spatial derivatives of convective terms, here the convective heat transfer $\dot{m}c\partial_z T$, can lead to numerical instability. Regarding the convective heat transfer of the vapor in the adsorbent channel or bulk, it is found that the CDA causes no numerical instability since the vapor velocity is low. However, numerical instability occurs when applying the CDA to the convective heat transfer in the heat transfer fluid of the GCM. Implementing the standard first-order upwind scheme does not overcome this problem. It is found that a slightly modified form of the upwind scheme ensures numerical stability. The implemented upwind scheme is

$$\left.\frac{\partial T_\mathrm{htf}}{\partial z}\right|_i \approx \begin{cases} \dfrac{T_{\mathrm{htf},i} - T_{\mathrm{htf},i-2}}{2\Delta z} & |u_\mathrm{htf}| > 0 \\ \dfrac{T_{\mathrm{htf},i+2} - T_{\mathrm{htf,i}}}{2\Delta z} & |u_\mathrm{htf}| < 0 \end{cases} \tag{5.2}$$

which can be understood as a shifted CDA. For $u_\mathrm{htf} = 0$ the standard CDA according to Eq. (5.1) is applied, nevertheless the convective heat transfer term is zero.

5.1.4. Boundary Conditions

As the CDA, see Eq. (5.1), is not applicable to determine the spatial derivatives on the boundaries, a one-sided finite difference approximation of first order is applied. The approximation reads

$$\left.\frac{\partial Y}{\partial z}\right|_0 = \frac{Y_1 - Y_0}{\Delta z} \tag{5.3}$$

where 0 denotes the boundary, Y_0 the unknown variable on the boundary and Y_1 refers to the unknown variable at the first knot normal to the boundary.

For the MCM and GCM a one-sided finite difference approximation of second order is applied to the spatial derivative of the temperature normal to the heat exchanger boundary, that is the surface of the heat exchanger plate. The applied second-order approximation reads

$$\left.\frac{\partial T}{\partial z}\right|_{\mathrm{htx}} = \frac{-T_2 + 9T_1 - 8T_{\mathrm{htx}}}{3\Delta x}, \tag{5.4}$$

where T_1 and T_2 denote the temperature at the first and second knot normal to the heat exchanger surface. Note that for the MCM and GCM the spacing between the heat exchanger boundary and the first knot is only $\Delta x/2$.

The spatial derivative of the temperature in the convective heat transfer term $\varepsilon \dot{m}_c c_{p,\mathrm{v}} \partial_z T$ at the vapor inlet is determined with the vapor temperature at the inlet T_{in} by

$$\left.\frac{\partial T}{\partial z}\right|_{\mathrm{in}} = \frac{T_1 - T_{\mathrm{in}}}{\Delta z} \tag{5.5}$$

to account for the convective cooling of the inflowing vapor. Note that for the GCM the spacing between the inlet boundary and the first knot is set to $\Delta z/2$ to increase the numerical accuracy.

5.2. Time Integration

5.2.1. Stiff System Integration

As mentioned before, a Matlab solver is applied for the time integration. However, the usually applied solvers (e. g. Runge-Kutta or multi-step methods) fail to integrate the system. The reason lies in the special characteristics of the system of PDEs describing the SCM, MCM and GCM. Evaluating the matrix elements of the time coefficient matrix (left side of Eq. (4.21) or Eq. (4.61)) for the possible pressure, temperature and water uptake values (in SI-Units) yields

$$\left\{\begin{array}{ccc} \frac{\varepsilon}{R_{\mathrm{s}}}\frac{1}{T} & -\frac{\varepsilon}{R_{\mathrm{s}}}\frac{p}{T^2} & \rho_{\mathrm{b}} \\ 0 & \rho_{\mathrm{c/b}}\Big(c_{\mathrm{z}} + X c_{\mathrm{a}}\Big) & -\rho_{\mathrm{c/b}}\Big(\Delta h_{\mathrm{a}} - R_{\mathrm{s}} T\Big) \\ 0 & 0 & 1 \end{array}\right\} \sim \left\{\begin{array}{ccc} 10^{-7}\ldots10^{-6} & 10^{-10}\ldots10^{-5} & 10^{3} \\ 0 & 10^{5}\ldots10^{6} & 10^{9} \\ 0 & 0 & 10^{1} \end{array}\right\}. \tag{5.6}$$

Thus, the matrix elements cover several orders of magnitude in a wide range of

$$\left\{\frac{\varepsilon}{R_{\mathrm{s}}}\frac{p}{T^2}\right\} \approx 10^{-10} \ldots \Big\{\rho_{\mathrm{c/b}}(\Delta h_{\mathrm{a}} - R_{\mathrm{s}} T)\Big\} \approx 10^{9}. \tag{5.7}$$

This indicates that the examined systems of PDEs, or more precisely the systems of ordinary differential equations (ODEs) derived from the spatial discretization of the PDEs, are so-called stiff ODE systems, e. g. [122]. The integration of stiff ODE systems is not trivial. Therefore, instead of implementing an own time integration solver, the Matlab solver for stiff ODE systems *ode15s* is applied. The applied Matlab solver is described and discussed in detail in [123].

To apply the Matlab solver *ode15s*, the discretized system has to be implemented in the form $\partial_t \boldsymbol{Y} = \mathrm{fct}(\boldsymbol{Y}, t)$ to allow for an explicit evaluation of the time derivatives. Here, $\boldsymbol{Y}$ denotes the vector of unknown variables for all knots. The Matlab solver *ode15s* is successfully applied to all studied cases. However, it should be noted that for inlet pressures approximately above $p_{\mathrm{in}} \geq 40\,\mathrm{mbar}$ the solver fails to integrate the system. Nevertheless, these cases are not of interest for the TES application studied in this work.

Moreover, the ODE systems are solved in a fully coupled approach, that is no separation into subsystems for different domains or unknown variables is conducted. For the MCM and GCM the controller and the heat exchanger equations are also included. Hence, no coupling procedure is required. Finally, the time coefficient matrix is an upper triangular matrix. Therefore, a stepwise evaluation of the equations is possible and no inner iterations need to be conducted.

5.2.2. Time Step Control

As mentioned in Sect. 5.1.1, for the AMR of the SCM the time integration has to be interrupted. The time step of the mesh adaption is controlled to always exceed the internal time step of the Matlab solver and is determined by

$$\Delta t_{\mathrm{AMR}} = C \frac{L}{u_{\mathrm{c}}(z=0)}. \tag{5.8}$$

Here, C denotes a scaling factor for the time step of the mesh adaption and can be understood as a modified Courant number. The scaling factor is determined from the initial modified Courant number $C_0 = \Delta t_{\mathrm{AMR},0} u_{\mathrm{c}}(z=0)/L$, the previous scaling factor and from the channel length and diameter. Furthermore, the scaling factor depends on the predicted advancement of the vapor in the channel. As soon as the vapor reaches the closed end of the channel, a linear increase of the time step of the mesh adaption is applied.

The evolution of the time step of the mesh adaption together with the internal time step of the Matlab solver without AMR for the reference case of the SCM (see Tab. 6.1) is shown in Fig. 5.4 (a) and (b). In Fig. 5.4 (a) the evolution of the time steps is depicted in a log-log plot for the initial duration for which Eq. (5.8) is applied. It is clear that the time step of the mesh adaption is significant higher in comparison to the internal time step of the Matlab solver. As mentioned, the time step of the mesh adaption is increased linearly as soon as the vapor reaches the closed end of the channel, see Fig. 5.4 (b). For this part of the process, the time step of the mesh adaption still exceeds the internal time step of the Matlab solver but is of the same order of magnitude. Hence, the acceleration of the computation by the AMR might be reduced for this part of the calculation. Finally, for the MCM and GCM no control of a time step for mesh adaption is required as no AMR is applied. In general, the adaption of the internal time step by the Matlab solver is found to be efficient and stable for the studied cases.

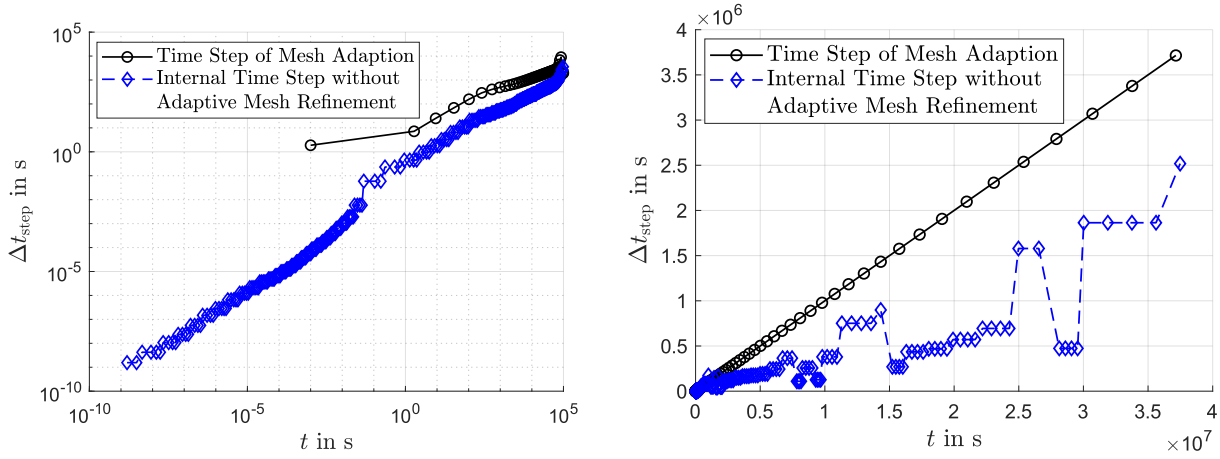

(a) Log-log plot for the initial duration with Eq. (5.8).

(b) Linear plot over the total process duration.

Figure 5.4.: Evolution of the time step of the mesh adaption together with the internal time step of the Matlab solver without AMR for the reference case of the SCM, see Tab. 6.1.

6. Results and Discussion

The simulation results of the three models SCM, MCM and GCM are discussed separately in this chapter (see Chap. 4 for Model Description). The discussion of the SCM results contributes to a basic understanding of the physical processes in closed low-pressure adsorbers. However, as a consequence of the one-dimensional and simple adsorber configuration, the results are of limited relevance for practical applications. The results of the two-dimensional models MCM and GCM are further analyzed with regard to modeling aspects as well as discussed in terms of application. Discussions of the SCM, MCM and GCM are included in part in:

[107] M. Schaefer and A. Thess. One-dimensional model of a closed low-pressure adsorber for thermal energy storage. *International Journal of Heat and Mass Transfer*, 2018.

[108] M. Schaefer and A. Thess. Simulation of a closed low-pressure honeycomb adsorber for thermal energy storage. *International Journal of Heat and Mass Transfer*, 2018.

[109] M. Schaefer and A. Thess. Modeling and simulation of closed low-pressure zeolite adsorbers for thermal energy storage. *International Journal of Heat and Mass Transfer*, 2019.

6.1. Single Channel Model

6.1.1. Case Set-Up

To study the influence of the geometry, the inner and outer channel diameter $d_{\mathrm{c,i}}$ and $d_{\mathrm{c,o}}$ as well as the length L of the single adsorbent channel are varied, see Fig. 4.2. The process parameters, given by the boundary and the initial conditions, are set to typical operating conditions of the discharging process, compare Sect. 1.2. The implemented values are summarized in Tab. 6.1. Note that in [107] the process parameters are varied for all geometry cases. Here, for a more comprehensive discussion, the influence of the process parameters is studied for one reference case (underlined values).

Table 6.1.: Geometry and process parameters of the cases studied by the SCM. The underlined values define the reference case.

Parameter	Value	Unit
Geometry		
$d_{\mathrm{c,i}}$	$\underline{0.5}$; 1.0; 2.0	mm
$d_{\mathrm{c,o}}$	(1.5; 2.0; $\underline{3.0}$) $\cdot\, d_{\mathrm{c,i}}$	mm
L	0.01; 0.1; $\underline{1}$	m
Boundary Conditions		
p_{in}	10	mbar
$T_{\mathrm{in}} = T_{\mathrm{s}}$	7	°C
T_{htx}	20	°C
Initial Conditions		
p_0	0.001	mbar
T_0	20	°C
$X_0 = X_{\mathrm{eq}}$	0.1	kg/kg

In accordance with [107], the results of the SCM are discussed in terms of mass transport, heat transport and adsorption. In contrast, the process duration and the influence of the process parameters are discussed in separate sections.

For a better comparability of the results, the non-dimensional time

$$\tilde{t} := \frac{t}{t_{\mathrm{tot}}} \tag{6.1}$$

is defined, where t_{tot} is the total process duration. For the SCM, the total process duration is defined as the time required for the temperature at the inlet of the adsorbent channel to decrease below 21°C, that is the maximum temperature variation along the channel has reduced to $\Delta T \leq 1\,\mathrm{K}$.

6.1.2. Mass Transport

The mass transport refers to the vapor flow in the vapor channel. The main assumption regarding this flow is that it is a creeping flow, that is the Reynolds number is low: $Re \ll 1$. To confirm the assumption, the maximum Reynolds number Re_{max} in the vapor channel versus the non-dimensional time $\tilde{t}$ is examined for all studied cases (see Tab. 6.1) and the range is shown in Fig. 6.1 (a). The figure reveals that the Reynolds number is very small throughout the process ($Re < 0.01 \ll 1$). Only initially, the Reynolds number exceeds the limit of creeping flow in some cases. However, the duration of this peak is negligibly short, and thus the assumption of creeping flow is valid.

Another aspect of the SCM regarding the vapor flow in the vapor channel is the consideration of the rarefaction effects, such as the slip and thermal creep effect, see Sect. 4.1.3. To evaluate whether rarefaction effects need to be considered for the studied cases, the Knudsen number has to be analyzed. The range of the Knudsen number Kn in the vapor channel versus the non-dimensional time $\tilde{t}$ is examined for all studied cases (see Tab. 6.1) and shown in Fig. 6.1 (b). Initially, the Knudsen number exceeds the slip regime up to the molecular regime. However, as discussed above for the Reynolds number, the duration of this excess is negligible short. For the major part of the process, the Knudsen numbers are below the transition regime: $Kn < 0.1$. Depending on the the channel diameter, the range of the Knudsen number either converges into the slip ($0.01 < Kn < 0.1$) or the no-slip ($Kn < 0.01$) regime. For a channel diameter of $d_{\mathrm{c,i}} = 0.5\,\mathrm{mm}$, the range of the Knudsen number remains in the slip regime over the whole process duration. This indicates that the slip effect might be relevant for this minimal channel diameter. In contrast, for a channel diameter of $d_{\mathrm{c,i}} = 2\,\mathrm{mm}$, the range of the Knudsen number completely lies in the no-slip regime. Thus, rarefaction effects are most likely negligible for these cases.

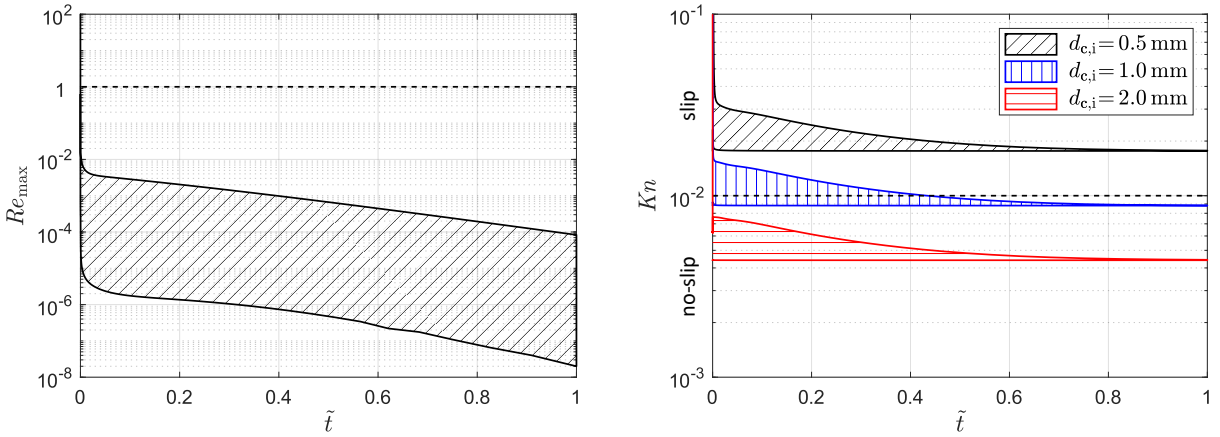

(a) Range of the maximum Reynolds number Re_{max}.

(b) Range of the Knudsen number Kn.

Figure 6.1.: Range of the maximum Reynolds number Re_{max} and Knudsen number Kn in the vapor channel versus the non-dimensional time $\tilde{t}$ for all cases studied by the SCM, see Tab. 6.1.

The local mass of the vapor in the channel corresponds to the local vapor density, which, according to the ideal gas law (4.12), is directly proportional to the pressure and inverse to the temperature. However, since the relative variation of the pressure is of several orders of magnitude (0.001 ... 10 mbar), and thus significantly higher than the relative variation of the temperature ($\approx 300 \ldots 450\,\mathrm{K}$), the vapor density mainly depends on the pressure. Therefore, the mass transport can be analyzed by examining the pressure.

The evolution of the pressure p in the vapor channel for the reference case (see Tab. 6.1) is shown in Fig. 6.2 (a). The sudden increase of the inlet pressure to $p_{\mathrm{in}} = 10\,\mathrm{mbar}$ leads to a relatively rapid advancement of the vapor into the channel in terms of the non-dimensional time. The vapor advances by a quarter of the channel length in less than 0.01% of the total process duration. However, the corresponding absolute time is $t = 1.11\,\mathrm{h}$. In comparison, the vapor flow in a channel of same geometry but without adsorption requires less than $t = 0.35\,\mathrm{s}$ to reach the end of the channel. This reveals that the advancement of the vapor is significantly slowed down by the radial adsorption of the vapor into the zeolite adsorbent. Furthermore, as the vapor advances further into the vapor channel the propagation velocity continues to decrease. For the vapor to reach $z \approx 0.75\,\mathrm{m}$ requires ten times longer than to reach $z \approx 0.25\,\mathrm{m}$. This decrease of the propagation velocity results from two effects. First, the further the vapor advances into the channel, the more vapor is being adsorbed along the channel. Second, the frictional losses of the vapor flow increase with the passed channel length. In addition, for $\tilde{t} = 0.1\%$ the pressure curve is of a concave shape. The concave shape results from the compressibility of the vapor, see Sect. 2.2.1. As the vapor reaches the closed end of the channel, the pressure increases throughout the channel. For the examined reference case, the pressure at the end of the channel has already increased to over 90% of the inlet pressure after less than $\tilde{t} = 1\%$.

As discussed before, the rarefaction effects on the mass transport are characterized by the Knudsen number. The evolution of the Knudsen number Kn in the vapor channel for the reference case (see Tab. 6.1) is shown in Fig. 6.2 (b). In accordance with Eq. (2.21), the Knudsen number and thus the Knudsen curves are inverse to the pressure. For a relatively short time $\tilde{t} < 1\%$, the Knudsen number ranges from the slip regime over the transition regime far into the free molecular regime. The length of the transition regime at $\tilde{t} = 0.1\%$ is marked on the corresponding pressure curve in Fig. 6.2 (a). For this instant of time, a significant part of the mass transport occurs in the transition regime. Further, as the pressure in the vapor channel increases after the vapor has reached the closed end of the channel, the Knudsen number decreases into the slip regime over the whole channel length. Finally, for $\tilde{t} > 1\%$ the shape of the Knudsen curve becomes mainly determined by the temperature since the pressure has reached an almost uniform distribution.

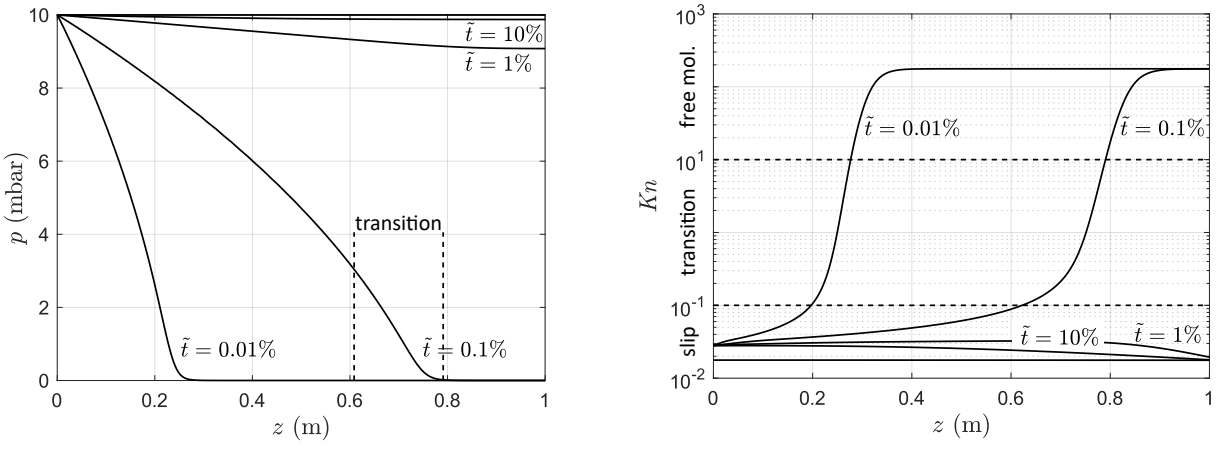

(a) Pressure p

(b) Knudsen number Kn

Figure 6.2.: Evolution of the pressure p and Knudsen number Kn in the vapor channel for the reference case, see Tab. 6.1.

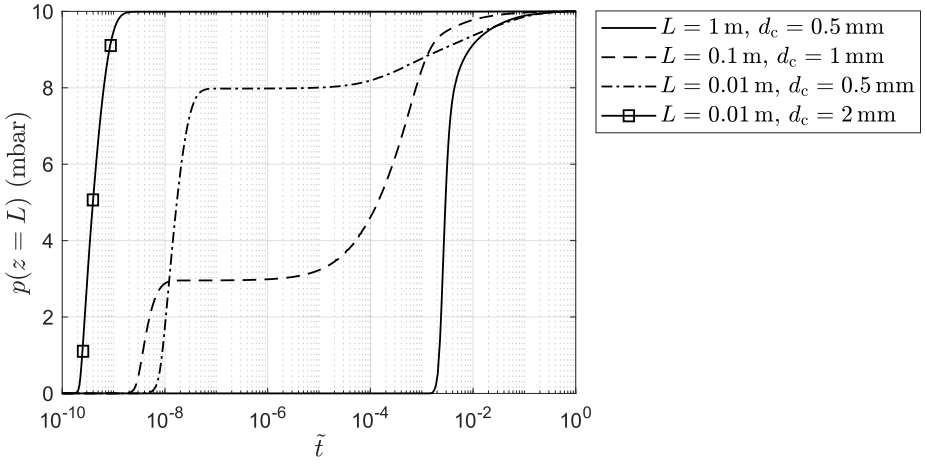

Figure 6.3.: Variation of the pressure at the end of the channel $p(z = L)$ versus the non-dimensional time $\tilde{t}$ for different geometry cases. For distinct geometry cases, the pressure at the end of the channel intermediately becomes constant over a short period of relative time.

From the discussion of the pressure evolution follows that a uniform pressure distribution can be assumed for the reference case as long as the details of the initial mass transport process for $\tilde{t} < 10\%$ are not of interest. The same applies to all studied cases (see Tab. 6.1). Nevertheless, the analysis of the pressure evolution for $\tilde{t} < 10\%$ reveals an unexpected physical phenomenon. To discuss this phenomenon, the variation of the pressure at the end of the channel $p(z = L)$ over the non-dimensional time $\tilde{t}$ is examined and shown in Fig. 6.3 for different geometry cases. Note that the pressure is plotted over the logarithmic non-dimensional time. It is observed that for distinct geometry cases the pressure at the end of the channel intermediately becomes constant over a short period of relative time, that is a pressure plateau exists. This phenomenon results from a temporary equilibrium between the vapor flow into the vapor channel and the adsorption by the zeolite adsorbent. To the author's knowledge, this phenomenon has not yet been reported in literature. It is clear from the figure that the level of the pressure plateau depends on the geometry of the adsorbent channel. In addition, the level of the pressure plateau also depends on the adsorbent properties. Hence, this phenomenon offers a novel experimental option to determine microscopic adsorbent properties such as porosity, tortuosity and mean macro-pore diameter.

6.1.3. Heat Transport

The heat transport in the adsorbent channel corresponds to the temperature. The evolution of the temperature T for the reference case (see Tab. 6.1) is shown in Fig. 6.4 (a). As discussed in the previous section, vapor is being adsorbed radially into the zeolite adsorbent while the vapor advances into the vapor channel. Due to the released heat of adsorption, the temperature increases. Therefore, a zone of increased temperature advances simultaneously with the vapor into the adsorbent channel. The figure reveals a steep temperature front of the advancing zone. In accordance with the mass transport, the relative time required for the temperature front to reach the end of the channel is low with $\tilde{t} < 1\%$. The rest of the process is characterized by a temperature decrease due to the heat extraction at the end of the channel. While the temperature decreases throughout the adsorber, the adsorption continues. However, the rate of the temperature decrease reduces over time since the temperature gradient and thus the heat flux by conduction decreases. Moreover, it is found that the inflowing vapor leads to a noticeable cooling of the adsorbent channel for $\tilde{t} \leq 1\%$, resulting in a temperature difference of ΔT between the maximum temperature in the adsorbent channel and the temperature at the inlet. Additionally, as the pressure gradient almost vanishes for $\tilde{t} > 1\%$ the mass flow rate of the inflowing vapor drops significantly. Thus, the convective cooling by the inflowing vapor becomes negligible.

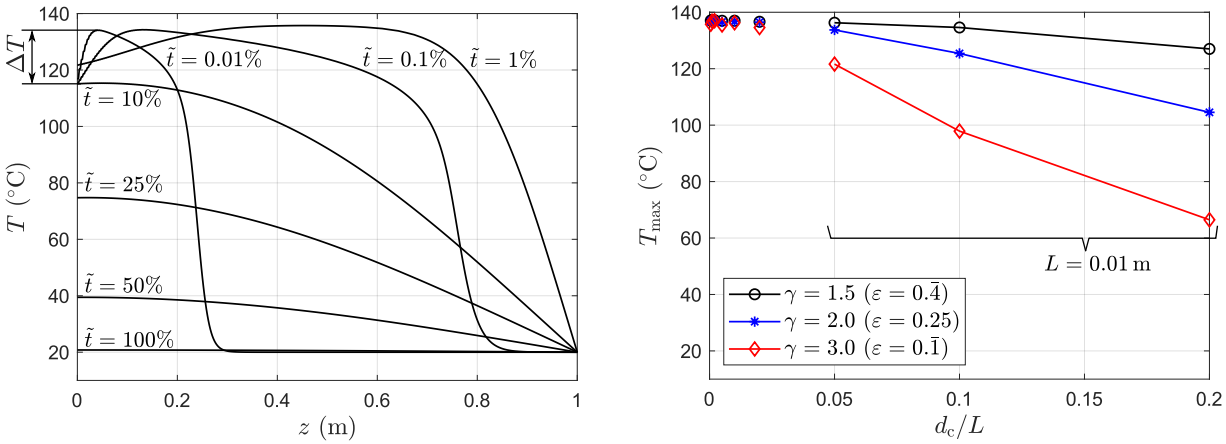

(a) Evolution of the temperature T

(b) Maximum temperatures T_{max}

Figure 6.4.: Evolution of the temperature T in the adsorbent channel for the reference case and variation of the maximum temperature T_{max} with the geometry parameters, s. Tab. 6.1.

The maximum temperature reached in the adsorber is found to depend on the geometry parameters. The dependency of the maximum temperature T_{max} on the aspect ratio of the inner channel diameter to the channel length $d_{c,i}/L$ as well as on the aspect ratio of the outer channel diameter to the inner channel diameter $\gamma = d_{c,o}/d_{c,i}$ is shown in Fig. 6.4 (b). The maximum temperature decreases with an increasing aspect ratio $d_{c,i}/L$. This decrease results from two effects. First, the heat transport path decreases with decreasing channel length, leading to an enhanced heat extraction. Second, for a constant aspect ratio $\gamma = d_{c,o}/d_{c,i}$, the adsorption kinetics decreases with increasing inner channel diameter, reducing the rate of released heat of adsorption. The second effect is amplified by increased aspect ratio $\gamma = d_{c,o}/d_{c,i}$. However, for an aspect ratio of $d_{c,i}/L \leq 0.02$, the maximum temperature becomes independent of the geometry parameters. The reached maximum temperature is solely determined by the adsorption. That means the temperature increases locally until pressure, temperature and water uptake reach a state of adsorption equilibrium.

To conclude the discussion of the heat transport, the thermal power is briefly analyzed. The thermal power is defined as the heat flux into the heat exchanger $p_{th,htx} = -\lambda_{eff}\, \partial_z T|_{htx}$. The specific thermal power at the heat exchanger $p_{th,htx}$ versus the non-dimensional time $\tilde{t}$ for varying geometry parameters is shown in Fig. 6.5. The thermal power initially increases fast as soon as the steep temperature front reaches the heat exchanger. Subsequently, the power slowly declines as

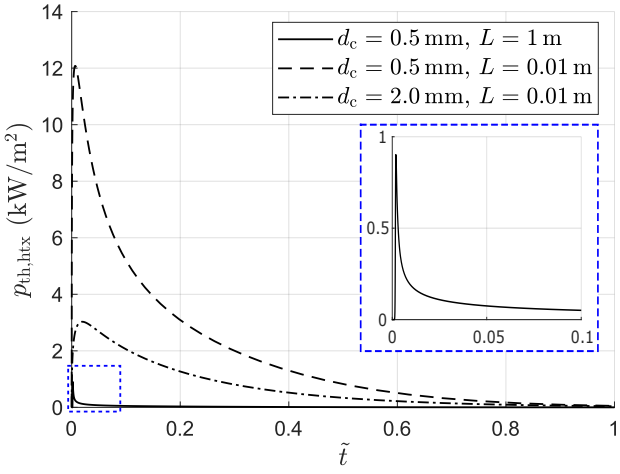

Figure 6.5.: Specific thermal power at the heat exchanger $p_{th,htx}$ over the non-dimensional time $\tilde{t}$.

the temperature in the adsorber decreases, compare Fig. 6.4 (a). It is found that the thermal peak power can be increased by one order of magnitude by reducing the length of the adsorbent channel by two orders of magnitude. However, increasing the inner channel diameter at a constant aspect ratio $\gamma = d_{c,o}/d_{c,i}$ reduces the thermal peak power again. As discussed above for the maximum temperature, this effect is explained by the limitation of the adsorption, that is the limitation by the internal mass transport resistance in the zeolite adsorbent, with increased channel diameter. This indicates that the thermal power can be optimized by variation of the geometry parameters.

6.1.4. Adsorption

The adsorption process is analyzed by the water uptake. The evolution of the water uptake X together with the local equilibrium water uptake X_{eq} in the adsorbent channel for the reference case (see Tab. 6.1) is shown in Fig. 6.6 (a). As discussed for the temperature, the advancing vapor in the vapor channel is radially adsorbed into the zeolite adsorbent. Therefore, a section of increased water uptake advances simultaneously with the vapor into the adsorbent channel. The increase of the water uptake is limited to the adsorption equilibrium, corresponding to the local pressure and temperature. Since the inflowing vapor initially reduces the temperature at the inlet of the adsorbent channel, compare Fig. 6.4 (a), the water uptake initially increases at the inlet. At the advancing front of the section of increased water uptake, the so-called adsorption front, the water uptake strongly deviates from the equilibrium water uptake due to the limitation by the internal mass transport resistance in the zeolite adsorbent. Thus, as long as the adsorption front is advancing through the adsorbent channel, the adsorption mainly takes place around the adsorption front. Comparison with the pressure evolution, see Fig. 6.2 (a), reveals that the advancing adsorption front lies in the range of the transition regime. Again, the relative time required for the adsorption front to reach the end of the channel is low with $\tilde{t} < 1\%$. The rest of the process is characterized by an increase of the water uptake in accordance with the temperature decrease in the adsorber, compare Fig. 6.4 (a). For this part of the process, no significant deviation from the local equilibrium water uptake is observed.

To further analyze the deviation from the adsorption equilibrium, the range of the maximum deviation $\Delta X_{max} = \max(X_{eq} - X)$ versus the non-dimensional time $\tilde{t}$ for all studied cases (see Tab. 6.1) is shown in Fig. 6.6 (b). Initially, the deviation from the adsorption equilibrium can reach up to $\Delta X_{max} \approx 0.275\,\mathrm{kg/kg}$. After the initial deviation peak, the maximum deviation from the

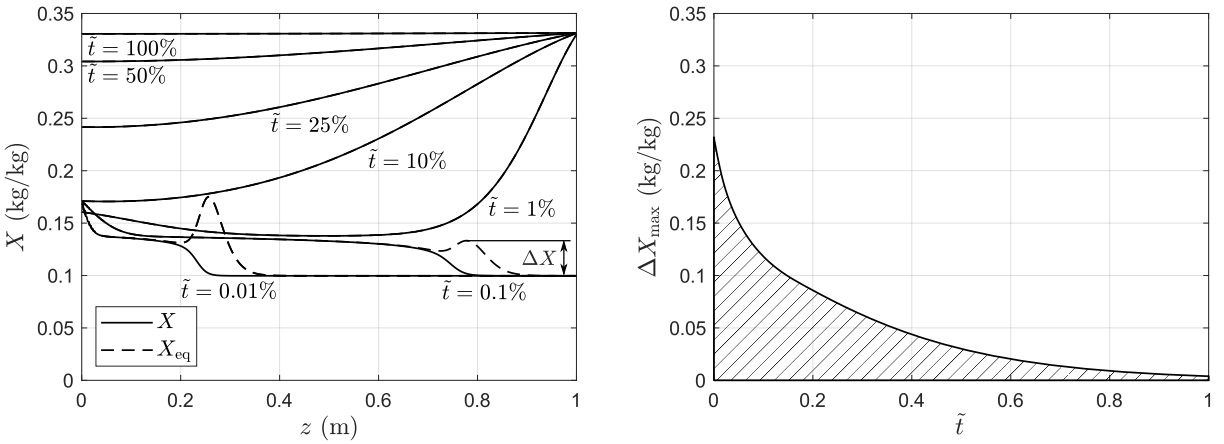

(a) Evolution of water uptake X and X_{eq}.

(b) Max. deviation from adsorption equilibrium ΔX_{max}

Figure 6.6.: Evolution of the water uptake X and X_{eq} in the adsorbent channel for the reference case and range of the maximum deviation from adsorption equilibrium ΔX_{max} for all studied cases, s. Tab. 6.1.

adsorption equilibrium continuously decreases. In general, the longer the adsorbent channel, the shorter the relative time for which significant deviation from the adsorption equilibrium occurs. While for $L = 1\,\mathrm{m}$ local adsorption equilibrium can be assumed for $\tilde{t} > 1\%$ in most cases, the deviation from the adsorption equilibrium has to be accounted for in all cases with $L = 0.01\,\mathrm{m}$.

6.1.5. Process Duration

One important parameter characterizing the discharging process is the total process duration. The total process duration t_{tot} versus the channel diameter $d_{\mathrm{c,i}}$ at different channel lengths L is given in Fig. 6.7 for all studied cases (see Tab. 6.1). One obvious conclusion is that the adsorber configuration studied by the SCM is of little practical relevance due to the long discharging durations. Further, the results show that the total process duration is independent of the channel diameter for channel lengths of $L \geq 0.1\,\mathrm{m}$. This indicates that the process is not limited by the mass transport, since otherwise the process duration would increase with decreasing inner channel diameter. Furthermore, the total process duration is independent of the aspect ratio of the outer to inner diameter $\gamma = d_{\mathrm{c,o}}/d_{\mathrm{c,i}}$ for channel lengths of $L \geq 0.1\,\mathrm{m}$. This indicates that the process is not limited by the adsorption. Otherwise, the process duration would increase with increasing aspect ratio of the outer to inner diameter since the adsorption kinetics parameter decreases with an increasing aspect ratio. In summary, it can be concluded that the total process durations of the studied cases with a channel length of $L \geq 0.1\,\mathrm{m}$ solely result from the limitation by the heat transport process.

In contrast, the total process duration is found to increase with increasing inner channel diameter for a channel length of $L = 0.01\,\mathrm{m}$. Following the previous discussion, this increase results from the limitation by the adsorption. As expected, the limitation by the adsorption increases with the aspect ratio of the outer to inner diameter $\gamma = d_{\mathrm{c,o}}/d_{\mathrm{c,i}}$. Finally, since none of the studied cases is limited by the mass transport in terms of the total process duration, no significant difference exists between the results of the Sharipov ($G_{\mathrm{P}}(Kn)$ according to Eq, (4.25)), slip and no-slip approach of the SCM. However, it is found that the effect of the thermal expansion of the vapor in the vapor channel is not negligible with respect to the process duration.

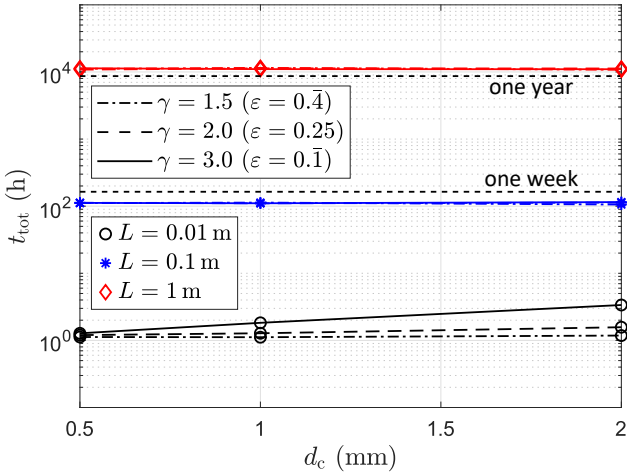

Figure 6.7.: Total process duration t_{tot} versus channel diameter $d_{\mathrm{c,i}}$ at different channel lengths L.

6.1.6. Process Parameters

To conclude the discussion of the simulation results of the SCM, the influence of the process parameters is analyzed in terms of the maximum temperature and the total process duration. The variation of the maximum temperature T_{max} and of the total process duration t_{tot} with the process parameters for the reference case (s. Tab. 6.1) is shown in Fig. 6.8. Note that the initial conditions yield four distinct initial states of water uptake, and thus the initial conditions can be defined by

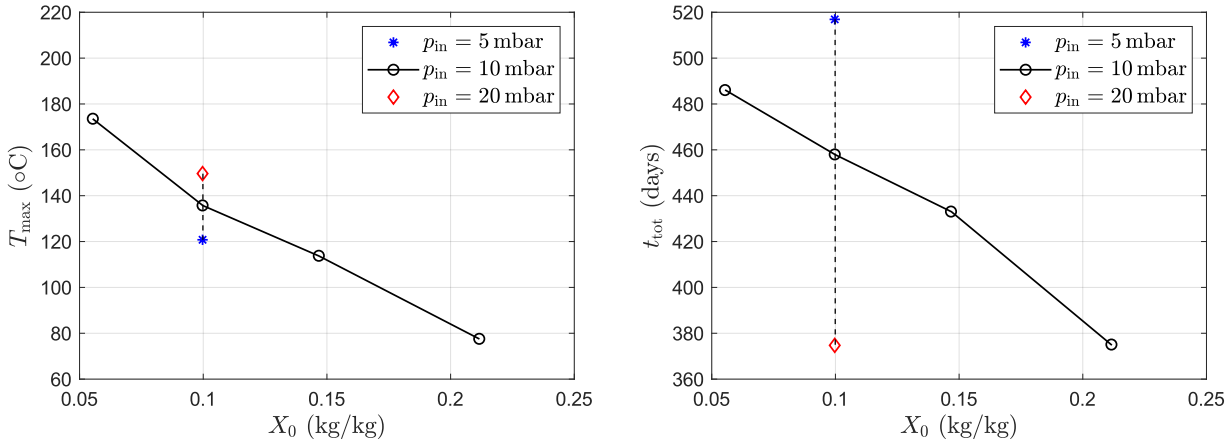

(a) Maximum temperature T_{max}.

(b) Total process duration t_{tot}.

Figure 6.8.: Variation of the maximum temperature T_{max} and the total process duration t_{tot} with the process parameters for the reference case, see Tab. 6.1.

the initial water uptake X_0. Regarding the maximum temperature, an almost linear dependency of the maximum temperature on the initial water uptake is found. The linear dependency correlates with the almost linear dependency of the heat of adsorption on the water uptake in this range, see Eq. (4.34). Similar dependency is observed for the total process duration. In contrast, the dependency of the maximum temperature and the total process duration on the inlet pressure is inverse. While the maximum temperature increases with the inlet pressure, the total process duration decreases. Finally, the influence of the inlet pressure on the total process duration is more prominent compared to the influence on the maximum temperature.

6.2. Multi Channel Model

6.2.1. Case Set-Up

To study the influence of the geometry, the channel height and width a and b, the web thickness f, the length L as well as the width W of the honeycomb adsorbent are varied, see Fig. 4.6 (a). The process parameters given by the boundary and the initial conditions are set as for the SCM, see Tab. 6.1. For one controlled case, the inlet pressure is increased to $p_{in} = 20\,\text{mbar}$. The implemented values are summarized in Tab. 6.2. In accordance with [108], the results of the MCM are first discussed for a reference case. The parameter values of the reference case are underlined in Tab. 6.2. Further, the results regarding modeling and application aspects are discussed separately.

Table 6.2.: Geometry parameters of the cases studied by the MCM. The underlined values define the reference case. The process parameters are set as for the SCM, see Tab. 6.1

Parameter	Value	Unit
a	0.5; 0.8; $\underline{1.0}$; $1.\bar{3}$; 1.6; 2.0	mm
b	$(\underline{1}; 2; 4; 10) \cdot a$	mm
f	$(0.25; 0.5; \underline{1.0}) \cdot a$	mm
L	0.1; $\underline{1}$	m
W	24; $\underline{48}$	mm

6.2.2. Reference Case

The reference case defined in Tab. 6.2 is studied to gain a basic understanding of the dynamic heat and mass transport as well as adsorption processes in the examined closed low-pressure honeycomb adsorber, see Fig. 4.5. The evolution of the symmetric temperature $T(\boldsymbol{x}, \tilde{t})$, pressure $p(\boldsymbol{x}, \tilde{t})$ and water uptake $X(\boldsymbol{x}, \tilde{t})$ fields is shown in Fig. 6.9 for a half-section of the honeycomb block of the reduced problem (see Fig. 4.7). As noted in Sect. 4.2.2, the MCM is discrete in the transversal direction due to the discrete adsorbent channels. However, in the figure the results are smoothed by interpolation in the transversal direction. The thin horizontal lines mark the virtual boundaries between the discrete adsorbent channels. Each row of the sub-figures represents the state at a specific non-dimensional time $\tilde{t}$, which is defined as for the SCM by Eq. (6.1). For the MCM the total process duration is defined as the time required for the spatial variations of temperature, pressure and water uptake to decrease below 1% of the corresponding maximum values.

The analysis of the temperature reveals that the adsorption leads to a temperature wave moving through the honeycomb, see Fig. 6.9 (a). The maximum values of the temperature wave occur in the honeycomb center and the minimum values at the heat exchanger boundary. Initially, the temperature in the center rises to a considerably high level of $T > 125$°C. Yet, after 10% of the total process duration, the maximum temperature has decreased to $T < 75$°C. Moreover, the advancing temperature wave has reached half of the honeycomb length. For the remaining time of the process, the temperature peak gradually decreases while advancing further into the honeycomb until it reaches the closed end of the honeycomb and vanishes.

The observed temperature evolution can be understood from the evolution of the pressure, see Fig. 6.9 (b). Initially, the applied boundary condition for the pressure at the inlet (Eq. (4.40), pressure jump) leads to a high pressure gradient at the inlet. This in turn induces a high vapor mass flow into the honeycomb, and thus results in a high adsorption rate. As a consequence, the temperature in the front part of the honeycomb rises quick initially. As the inflowing vapor advances further into the honeycomb, the pressure gradient, and thus the vapor mass flow into the honeycomb and the adsorption rate, gradually decrease.

Interestingly, at the beginning, the vapor in the center advances fastest into the honeycomb, but after 25% of the total process duration, the advancement of the vapor at the heat exchanger boundary exceeds the central channel. This effect can be explained by the evolution of the water uptake, see Fig. 6.9 (c). It is observed that initially a significant rise of the water uptake ($X = 0.15\,\mathrm{kg/kg}$) occurs farther in the honeycomb at the outer heat exchanger boundary compared to the honeycomb center. This indicates that almost instantly the adsorption at the very front of the honeycomb center reaches a temporary adsorption equilibrium. The temporary adsorption equilibrium results from the higher temperature in the honeycomb center. As a result, a higher fraction of the inflowing vapor can bypass the front of the honeycomb center without being adsorbed, thus resulting in a faster advancement of the vapor in the honeycomb center. As soon as the temperature in the center decreases again due to the heat extraction by the heat exchanger as well as convective cooling by the inflowing vapor, the adsorption continues in the front part of the honeycomb center, and thus reduces the advancement of the vapor into the honeycomb.

As soon as the vapor reaches the closed end of the honeycomb, the pressure increases quickly to the level of the inlet pressure throughout the honeycomb. This effect results from two events. First, as the vapor reaches the end of the honeycomb, the water uptake front also reaches the end. Thus, the mass sink due to adsorption vanishes, and hence the inflowing vapor fills the channels faster. Second, as the vapor reaches the closed end of the channels, a back-pressure effect occurs.

The discussion of the reference case demonstrates that the heat and mass transport and the adsorption processes are strongly coupled and can only be understood in their interaction. With respect to the cases of shorter honeycombs ($L = 0.1\,\mathrm{m}$), it is found that the heat and mass transport and adsorption processes are similar to the processes observed at the front ($z \leq 0.1\,\mathrm{m}$) of the reference case. Hence, no distinct temperature wave is observed for these cases.

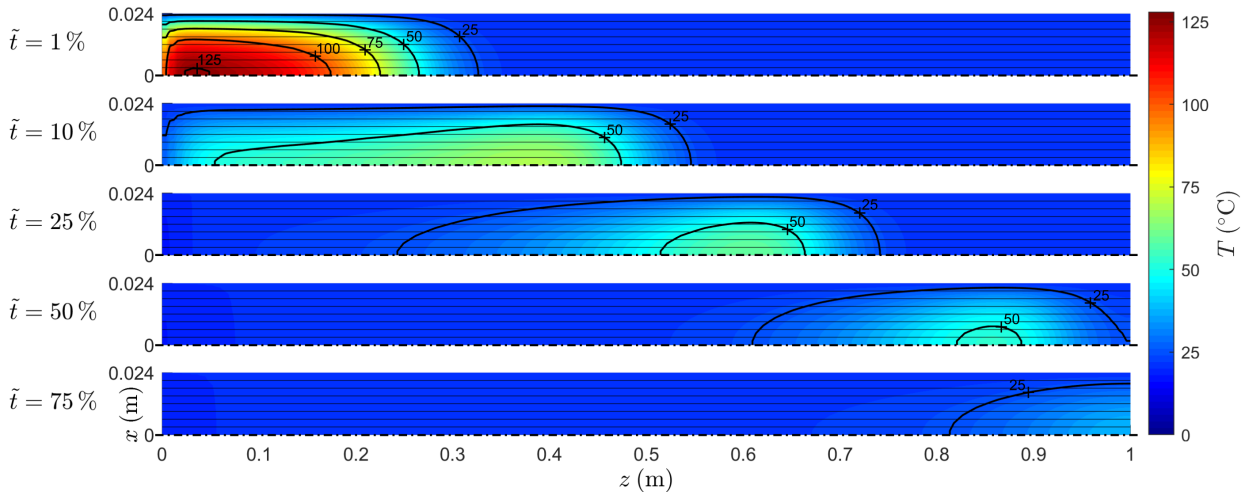

(a) Evolution of the symmetric temperature field $T(\boldsymbol{x}, \tilde{t})$ over the non-dimensional time $\tilde{t}$.

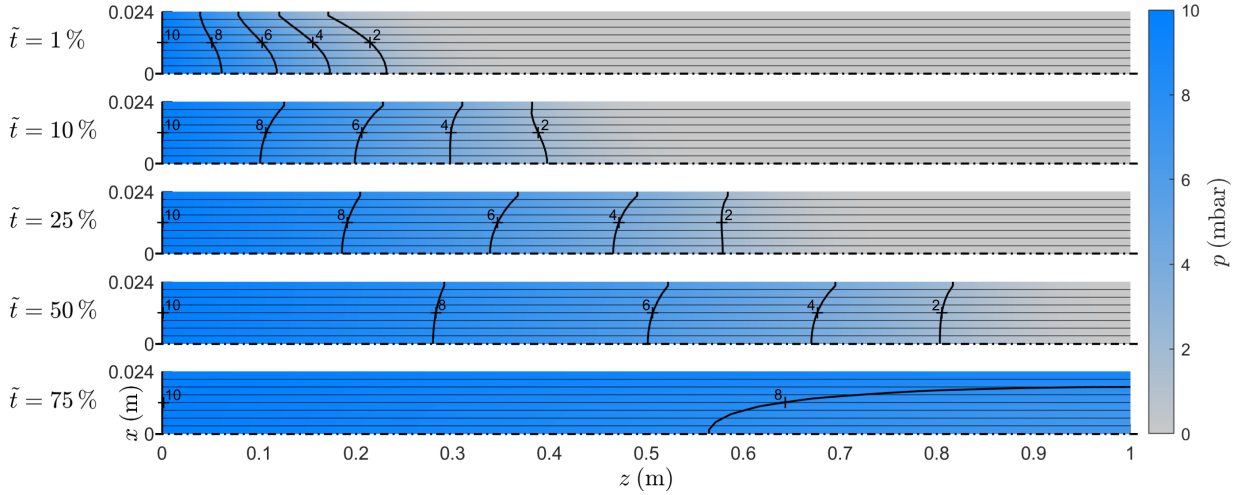

(b) Evolution of the symmetric pressure field $p(\boldsymbol{x}, \tilde{t})$ over the non-dimensional time $\tilde{t}$.

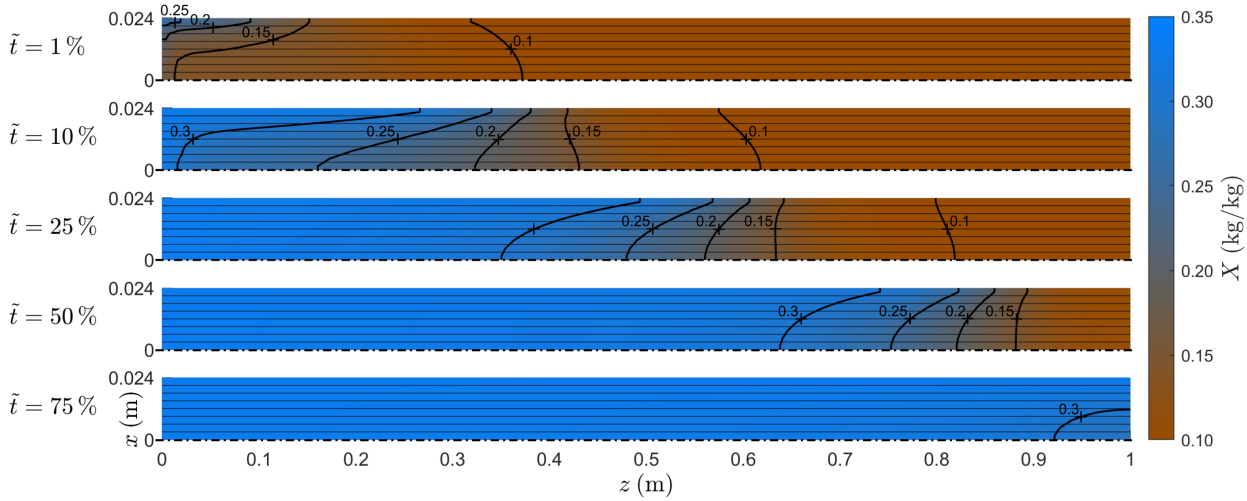

(c) Evolution of the symmetric water uptake field $X(\boldsymbol{x}, \tilde{t})$ over the non-dimensional time $\tilde{t}$.

Figure 6.9.: Evolution of the symmetric temperature $T(\boldsymbol{x}, \tilde{t})$, pressure $p(\boldsymbol{x}, \tilde{t})$ and water uptake $X(\boldsymbol{x}, \tilde{t})$ fields over the non-dimensional time $\tilde{t}$ in a half-section of the honeycomb block for the reference case, see Tab. 6.2. The results are smoothed by interpolation in the transversal direction over the discrete channels. The thin horizontal lines mark the virtual boundaries between the discrete channels.

6.2.3. Modeling

6.2.3.1. Equilibrium Assumptions

To discuss whether equilibrium assumptions for the temperature or the pressure would be valid for the honeycomb adsorber cases studied by the MCM (see Tab. 6.2), the spatial variations have to be analyzed. For this purpose, the evolution of the maximum relative deviations from the maximum values in the adsorber is evaluated. Regarding the adsorption, the evolution of the maximum relative deviation from the corresponding local adsorption equilibrium is determined. The range of the maximum relative deviations of the temperature T, pressure p and water uptake X versus the non-dimensional time $\tilde{t}$ for different sets of geometry parameter values are shown in Fig. 6.10. Note that the relative deviations of the temperature are evaluated on the Celsius scale.

From Fig. 6.10 (a) it follows that the maximum relative deviations of the temperature initially shoot up to 70 ... 85% for all cases. After half of the process, the relative deviations still lie in the range of 20 ... 75% and even at the end of the process, the relative deviations can reach up to more than 10%. Therefore, the spatial variations of the temperature must be accounted for and the equilibrium assumption cannot be applied to the temperature for the studied cases. Moreover, since in the MCM the thermal heat flux between the honeycomb and the heat exchanger is determined from the temperature gradient in the honeycomb at the heat exchanger surface, the spatial temperature distribution has to be considered in this model. Although the two ranges for the different honeycomb lengths overlap, the curves of the single cases can be distinguished. The cases of $L = 0.1\,\mathrm{m}$ decline after the initial peak, whereas the cases of $L = 1\,\mathrm{m}$ show a second peak.

The evaluation of the maximum relative deviations of the pressure yields that the range of the relative deviations can be distinguished more clearly by the honeycomb length, see Fig. 6.10 (b). For the honeycomb length of $L = 1\,\mathrm{m}$, the spatial variations of the pressure must always be taken into account, e. g. the relative deviation of the reference case remains at a maximum for more than half of the total process duration. In comparison, the relative deviations of the pressure in a honeycomb with a length of $L = 0.1\,\mathrm{m}$ generally decrease faster. For a few particular cases of large channel size a and b and low web thickness f, the relative deviations even decrease rapidly. For these few cases the equilibrium assumption could be applied to the pressure. However, for the majority of studied cases the equilibrium assumption cannot be applied.

Regarding the maximum relative deviations of the water uptake, it is found that the range of the relative deviations can also be distinguished by the honeycomb length, see Fig. 6.10 (c). Again, for a few particular cases with a honeycomb length of $L = 0.1\,\mathrm{m}$, the relative deviations of the water uptake decrease rapidly. For the majority of studied cases though, a significant relative deviation from the adsorption equilibrium over a relevant part of the total process duration is observed, e. g. for the reference case the relative deviation exceeds 50% over half of the total process duration. Thus, local adsorption equilibrium cannot be assumed and therefore the limitation by the internal mass transport resistance in the zeolite adsorbent has to be considered for the studied cases.

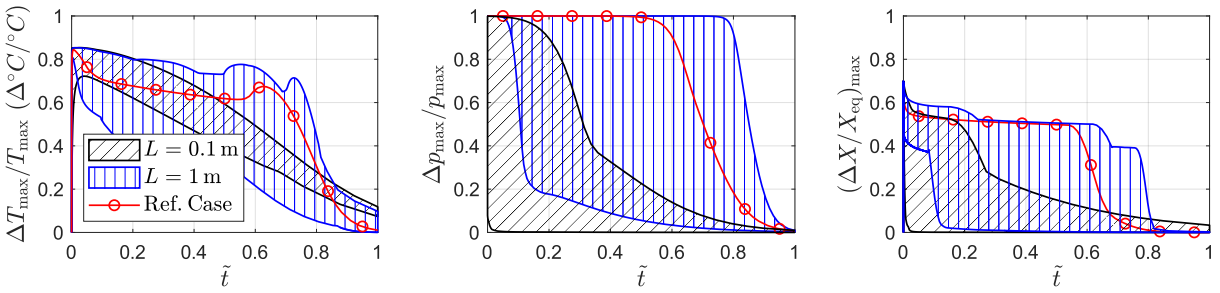

(a) Rel. deviations of temperature T. (b) Rel. deviations of pressure p. (c) Rel. deviations of water uptake X.

Figure 6.10.: Range of the maximum relative deviations of the temperature T, pressure p and water uptake X versus time for different sets of geometry parameter values, see Tab. 6.2.

6.2.3.2. Rarefaction Effects

As described in Sect. 4.2.3, the MCM takes rarefaction effects such as the slip and thermal creep effect into account. With respect to the thermal creep effect, the analysis of all studied cases (see Tab. 6.2) yields that the vapor mass flow induced by the thermal creep effect is smaller by approximately five orders of magnitude compared to the total vapor mass flow. Taking the reference case as an example, the maximum total vapor mass flow into a single channel of the honeycomb is 25.86 g/h compared to a maximum vapor mass flow of 0.00033 g/h induced by the thermal creep effect. Therefore, the thermal creep effect is negligible for all studied cases, and thus the effect is not discussed further. In contrast, the slip effect is found to have noticeable effect on the vapor mass flow in the honeycomb channels and is discussed below.

The evolution of the vapor mass flow $\dot{m}_{\mathrm{c,in}}$ into the central honeycomb channel for the reference case is shown in Fig. 6.11 (a). Initially, as described for the reference case in Sect. 6.2.2, a relatively high peak of the vapor mass flow occurs. The peak value lies outside the range of the figure but is indicated by the vertical arrow. The no-slip model underestimates the peak value of the vapor mass flow by 3.8%. Subsequently, the vapor mass flow rapidly drops to a significantly lower level and after a small second peak continues to decrease gradually. The no-slip model continues to slightly underestimate the vapor mass flow until $t \approx 17.5\,\mathrm{h}$. As a consequence, it predicts a higher mass flow afterwards. Overall, the no-slip model leads to an overestimation of the total process duration of about 7%. In comparison, the Sharipov and the slip model, corresponding to the G_{P}-functions (4.45) and (4.46), yield identical results over the whole process duration. Thus, rarefaction effects beyond the slip effect are negligible. Finally, since the total thermal power of the adsorber is proportional to the vapor mass flow into the adsorber, it can be concluded that the no-slip model also predicts the evolution of total thermal power reasonably well.

To evaluate the local influence of the slip effect, the vapor mass flow $\dot{m}_{\mathrm{c}}$ over the central honeycomb channel for the reference case is examined for $t = 3\,\mathrm{h}$, see Fig. 6.11 (b). For the examined time, the vapor mass flow (blue curve) decreases linearly along the channel and vanishes almost completely at $z \approx 0.5\,\mathrm{m}$. This indicates that the inflowing vapor is adsorbed with a constant adsorption rate over half of the honeycomb length. Hence, it can be concluded that the adsorption not solely occurs at a sharp adsorption front. Besides the vapor mass flow, the Knudsen number Kn with the corresponding flow regimes as well as the relative error Γ of the non-dimensional mass flow G_{P} of the no-slip model is also depicted. The figure reveals that the relevant vapor mass flow

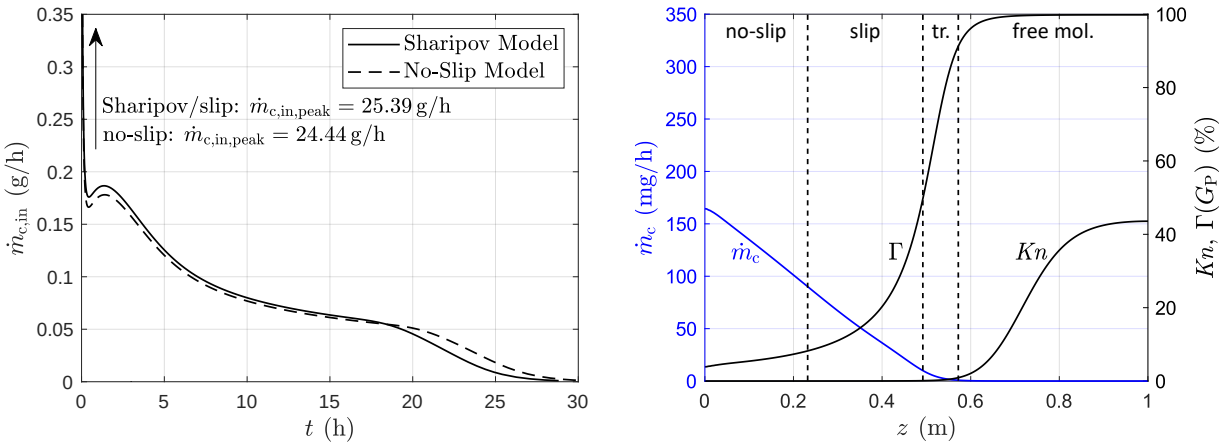

(a) Evolution of the vapor mass flow $\dot{m}_{\mathrm{c,in}}$ into the central honeycomb channel. The peak value lies outside of the figure range and is indicated by the vertical arrow.

(b) Vapor mass flow $\dot{m}_{\mathrm{c}}$, Knudsen number Kn and relative error Γ of the non-dim. mass flow G_{P} for the no-slip model over the central honeycomb channel at $t = 3\,\mathrm{h}$.

Figure 6.11.: Influence of the slip effect on the vapor mass flow in the central honeycomb channel for the reference case, see Tab. 6.2.

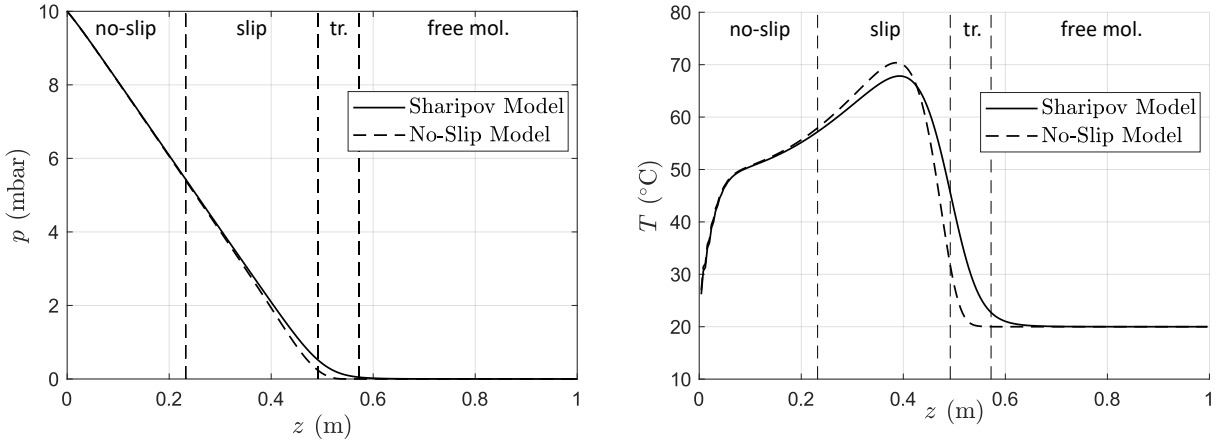

(a) Pressure distribution $p(z,t)$.

(b) Temperature distribution $T(z,t)$.

Figure 6.12.: Influence of the slip effect on the pressure and temperature distribution over the central honeycomb channel at $t = 3\,\mathrm{h}$ for the reference case, see Tab. 6.2.

reaches from the no-slip over the slip into the transitional regime. Accordingly, the local error of the non-dimensional mass flow increases from less than 5% at the channel entrance to approximately 90% at the adsorption front. In the free molecular regime, the relative error is at a maximum since the no-slip model predicts no mass flow.

However, the local error of the non-dimensional mass flow determined by the no-slip model is compensated to some extent by another error of the no-slip model. This error is related to the pressure. The pressure distribution along the channel $p(z,t)$ over the central honeycomb channel at $t = 3\,\mathrm{h}$ is shown in Fig. 6.12 (a). The figure reveals that the no-slip model predicts a higher pressure gradient in the slip regime. In accordance with Eq. (4.24), the increasing underestimation of the non-dimensional mass flow is compensated by an increasing overestimation of the pressure gradient along the channel. In the transition regime however, the no-slip model also underestimates the pressure gradient, amplifying the total local error. As the vapor mass flow is relatively low in the transition regime compared to the mass flow at the channel entrance, the effect of this local error on the global error (e. g. the total process duration) is negligibly low. The effect of the increased local error is most prominent for the temperature distribution along the central honeycomb channel and shown in Fig. 6.12 (b). The figure shows that the local error first leads to an overestimation of the temperature in the slip regime, followed by an increasing underestimation. The maximum underestimation of the temperature is 35% on a Celsius scale.

6.2.4. Application

As discussed in Sect. 1.3, the thermal power is of interest in TES application. Therefore, the following discussion focuses on the thermal power. For better comparability of the studied cases, the volumetric thermal power is examined. For the MCM, the volumetric thermal power is defined as the thermal power per volume of honeycomb adsorbent. That means that the volume of the heat exchanger plates and the storage casing as well as the insulation is not considered. Note that in the following the volumetric thermal power is also simply referred to as thermal power.

6.2.4.1. Variation of Geometry Parameters

At first, the effect of the geometry parameters on the thermal power is studied for the special cases of honeycombs with square channels ($a = b$). For these cases, $\gamma = \gamma_a = \gamma_b$ with γ according to Eq. (4.39) applies. The dependency of the thermal power p_{th} on the honeycomb geometry parameters for these cases is depicted in Fig. 6.13. While the absolute thermal power of all studied

cases is of the same order, the volumetric thermal power of the honeycomb cases depends on the honeycomb length. In general, the volumetric thermal power is inverse to the honeycomb length. As expected, the reduction of the honeycomb width W increases the thermal power since the length of the heat transport path is proportional to the honeycomb width. In addition, it is found that the increase of γ, that is the reduction of the honeycomb porosity ε, leads to a reduction of the thermal power. This limitation by the adsorption is explained by the increase of the mass transport resistance in the zeolite adsorbent due to an increased web thickness f, which in turn reduces the adsorption kinetics.

In Fig. 6.13 (a), the peak power $p_{\mathrm{th,peak}}$ is shown. The results reveal that an optimum of the peak power over the channel size for a honeycomb length of $L = 0.1\,\mathrm{m}$ exists in the studied parameter range. The local optimum can be explained by the external and internal mass transport resistance. Left of the optimum, the thermal power is limited by the external mass transport resistance of the honeycomb channels. Increasing the channel size reduces the external mass transport resistance, and thus increases the thermal power. At the same time, for a fixed γ, that is a fixed porosity ε of the honeycomb, the increase of the channel size also leads to an increase of the honeycomb web thickness f. As a consequence, the internal mass transport resistance of the zeolite adsorbent increases with the channel size. Hence, right of the optimum the thermal power is limited by the internal mass transport resistance of the zeolite adsorbent. For a honeycomb length of $L = 1\,\mathrm{m}$, no local optimum of the peak power exists in the depicted range of channel size. However, the optimum is found to be around $a \approx 4\,\mathrm{mm}$.

The evaluation of the mean power yields the interesting result that, while an optimum of the peak power is found for a honeycomb length of $L = 0.1\,\mathrm{m}$, no optimum exists for the mean power in the examined range of the channel size, see Fig. 6.13 (b). The opposite is found for the honeycomb length of $L = 1\,\mathrm{m}$. The explanation of the optimum of the mean power is analog to the explanation of the peak power optimum. In summary, TES based on the examined closed low-pressure honeycomb adsorber can be optimized either for the peak or the mean power.

To complete the discussion on the variation of the geometry parameters, the thermal power is examined for the general case of honeycombs with non-square channels. The evolution of the thermal power p_{th} for the reference case ($a = b$) and modified cases with non-square channels ($a \neq b$) is shown in Fig. 6.14 (a). It is found that the peak power increases with the aspect ratio b/a, given a constant value of the channel height. The increase of the peak power results from the decrease of the mass transport resistance in the honeycomb channels, which decreases with

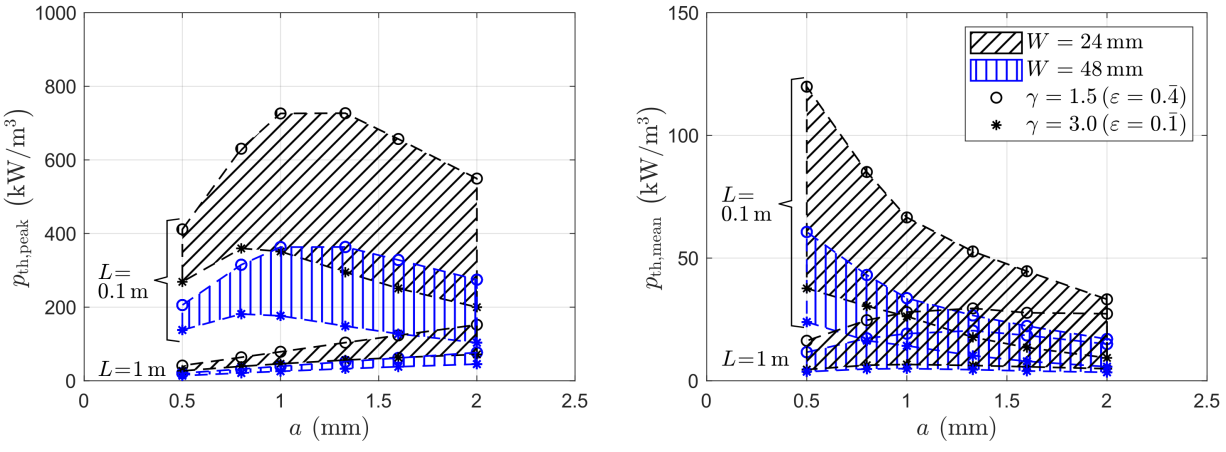

(a) Peak power $p_{\mathrm{th,peak}}$.

(b) Mean power $p_{\mathrm{th,mean}}$.

Figure 6.13.: Dependency of the volumetric thermal power p_{th} on the geometry parameters for honeycombs with square channels, see Tab. 6.2. The optima of the thermal power result from the external and internal mass transport resistances.

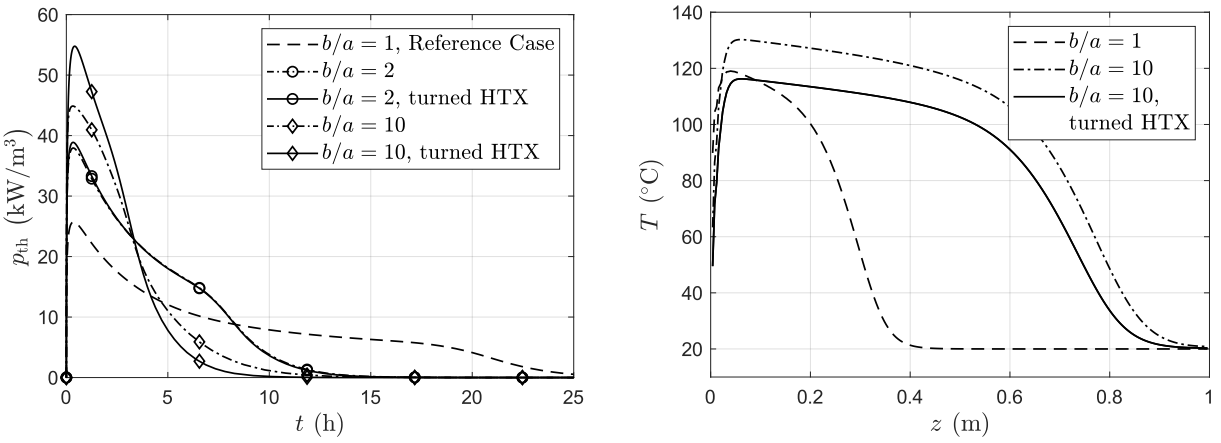

(a) Evolution of the thermal power p_{th}.

(b) Central temperature distribution $T(z)$ for $\tilde{t} = 1\%$.

Figure 6.14.: Evolution of the volumetric thermal power p_{th} and the temperature distribution for $\tilde{t} = 1\%$ (t_{tot} from reference case) in the central honeycomb channel for the reference case ($a = b$) and modified cases with non-square channels ($a \neq b$), see Tab. 6.2 .

the channel width. The reduced mass transport resistance increases the vapor mass flow into the honeycomb, and thus the vapor advances faster into the adsorber. As a result, the temperature front also advances faster, and thus the thermal power increases. The temperature distribution in the central honeycomb channel for $\tilde{t} = 1\%$ of the reference case is shown in Fig. 6.14 (b). With respect to the heat exchanger orientation (see Fig. 4.6), no significant difference for $b/a = 2$ occurs. In contrast, the heat exchanger orientation has a noticeable effect for an aspect ratio of $b/a = 10$. In this case, the turned heat exchanger yields an increase of the thermal power by 20%.

6.2.4.2. Control of Thermal Power

As discussed for the reference case in Sect. 6.2.2, the boundary condition for the pressure at the inlet initially induces a high vapor mass flow into the honeycomb, resulting in an immediate and high temperature rise at the honeycomb front. This temperature rise leads to an initial peak of the thermal power, compare e. g. Fig. 6.14 (a). Therefore, to control the thermal power, the inlet pressure has to be controlled. The implemented controller is described in Sect. 4.2.6.

The evolution of the volumetric thermal power p_{th} for the reference case without control and the controlled cases of different set point values $p_{\mathrm{th,set}}$ is shown in Fig. 6.15 (a). The results show that the thermal power can be effectively controlled by shifting the thermal energy of the power peak. The controlled case with a set point value of $p_{\mathrm{th,set}} = 10\,\mathrm{kW/m^3}$ and a maximum inlet pressure of $p_{\mathrm{in,max}} = 10\,\mathrm{mbar}$ shows that the thermal power cannot be hold at the set point value for the total process duration. In fact, for $t > 10\,\mathrm{h}$ the thermal power becomes limited by the mass transport. One solution to overcome the limitation by the mass transport is to increase the inlet pressure. The last case with a maximum inlet pressure of $p_{\mathrm{in,max}} = 20\,\mathrm{mbar}$ proves that it is possible to hold the thermal power at the set point value of $p_{\mathrm{th,set}} = 10\,\mathrm{kW/m^3}$ for the total process duration.

The evolution of the controlled inlet pressure p_{in} for the controlled cases of different set point values $p_{\mathrm{th,set}}$ is shown in Fig. 6.15 (b). The results show that the inlet pressure increases quickly initially. This pressure jump is proportional to the set point value $p_{\mathrm{th,set}}$. As soon as the set point value is reached, the power regulated controller is applied, significantly reducing the increase rate of the pressure. The slope of the subsequent pressure curve is proportional to the set point value of the thermal power. At the end of the process, the increase of inlet pressure is accelerated for the case with lowest set-point value ($p_{\mathrm{th,set}} = 2.5\,\mathrm{kW/m^3}$) and for the case with increased maximum inlet pressure ($p_{\mathrm{in,max}} = 20\,\mathrm{mbar}$). This indicates that the pressure regulated controller becomes activated again since the thermal power can no longer be hold at the set point value.

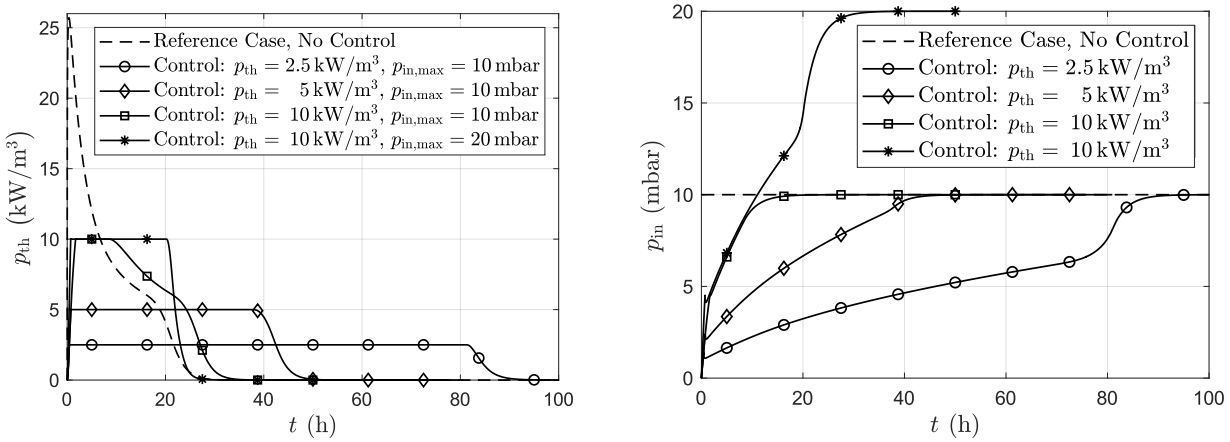

(a) Thermal power $p_{th}(t)$.

(b) Inlet pressure $p_{\mathrm{in}}(t)$.

Figure 6.15.: Volumetric thermal power p_{th} and corresponding inlet pressure p_{in} versus time t for the reference case without control and for the controlled cases of different set point values $p_{\mathrm{th,set}}$ and maximum inlet pressure $p_{\mathrm{in,max}}$.

To study the effect of the power control on the transport processes in the honeycomb, the controlled case with a set point value of $p_{\mathrm{th,set}} = 10\,\mathrm{kW/m^3}$ and a maximum inlet pressure of $p_{\mathrm{in,max}} = 20\,\mathrm{mbar}$ is examined further. The evolution of the symmetric temperature field $T(\boldsymbol{x}, \tilde{t})$ for a half-section of the honeycomb block is shown in Fig. 6.16. The comparison with the evolution of the symmetric temperature $T(\boldsymbol{x}, \tilde{t})$ field for the reference case without control (see Fig. 6.9 (a)) confirms the assumption that the controlled and moderate increase of the inlet pressure prevents the initial overheating of the honeycomb front. Furthermore, as the temperature wave advances into the honeycomb, the peak remains at the same temperature level, resulting in constant thermal power. Finally, for $\tilde{t} = 10\%$ and $\tilde{t} = 75\%$ a longer zone of increased temperature with $T \geq 50°\mathrm{C}$ is observed. These extended zones result from the fact that initially and at the end of the process the total length of the zone of increased temperature in the honeycomb is slightly shorter compared to the total length of the advancing temperature wave.

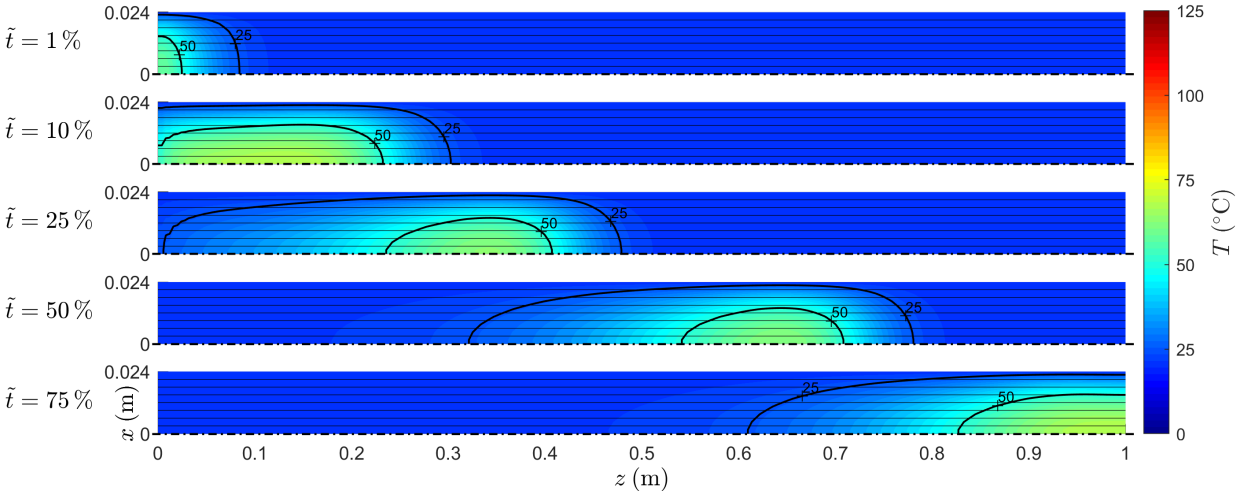

Figure 6.16.: Evolution of the symmetric temperature field $T(\boldsymbol{x}, \tilde{t})$ for the controlled case with a set point value of $p_{\mathrm{th,set}} = 10\,\mathrm{kW/m^3}$ and a maximum inlet pressure of $p_{\mathrm{in,max}} = 20\,\mathrm{mbar}$.

6.3. General Continuum Model

6.3.1. Case Set-Up

To study the influence of the geometry, the diameter of the honeycomb channels d_c and the diameter of the granules and powder particles d_p are varied. Regarding the process parameters, the boundary condition of the heat exchanger is varied in terms of the outlet temperature $T_{htf,out}$ and the mean velocity u_{htf} of the heat transfer fluid. Otherwise, the process parameters are set as for the SCM, see Tab. 6.1. In comparison to the MCM, the outlet temperature of the heat transfer fluid ($T_{htf,out}$) is controlled instead of the volumetric power. The implemented values are summarized in Tab. 6.3.

Table 6.3.: Geometry and process parameters of the cases studied by the GCM. The underlined values define the reference cases. Further parameters are set as for the SCM, see Tab. 6.1

Parameter	Value	Unit
Geometry		
$\underline{d}_c$, $\underline{d}_p$	honeycomb / granules: 0.5; <u>1</u>; <u>2</u>; 4; 8	mm
	powder**:** 0.5; <u>50</u>	μm
ε	honeycomb: $0.\bar{1}$; granules: 0.4; powder: 0.65	m^3/m^3
L	1	m
W	48	mm
h_{htx}	3	mm
Boundary Conditions		
$T_{htf,in}$	20	°C
$T_{htf,out}$	30; <u>40</u>; 60 (ΔT_{htf} = 10; <u>20</u>; 40)	°C
u_{htf}	0.5; <u>1.0</u>; 2.0	mm/s

6.3.2. Reference Cases

As for the MCM, one reference case for each adsorbent configuration as defined in Tab. 6.3 is studied to gain a basic understanding of the transport processes in the adsorbent bulk. Note that for the powder case the adsorber configuration is modified to overcome mass transport limitations, see Sect. 4.3.1. In this case, the vapor is supplied at the symmetry plane between two heat exchanger plates over the whole length of the adsorber. For the GCM the total process duration, also referred to as discharging duration, is defined as the time required for the outlet temperature of the heat transfer fluid to decrease below 21°C, that is the temperature lift is below $\Delta T_{htf} = 1\,K$.

The evolution of the symmetric temperature fields $T(x, \tilde{t})$ in the studied half-section of the adsorbent bulk (see Sect. 4.3.1) for the three reference cases is shown in Fig. 6.17. Each row of the sub-figures represents the state at a specific non-dimensional time $\tilde{t}$, which is defined by Eq. (6.1) for the SCM. For the GCM, the total process duration is defined as the time required for the outlet temperature of the heat transfer fluid to decrease below $T_{htf,out} \leq 21°C\,(\Delta T_{htf,out} \leq 1\,K)$. Note that the non-dimensional times for the three reference cases are the same, while the absolute times differ. Furthermore, the pressure and water uptake fields are not discussed here. For the honeycomb case without control, these fields have been discussed in detail for the MCM in Sect. 6.2.2. Qualitatively, the pressure and water uptake fields are similar to the fields of the controlled honeycomb and granules case as well as the powder case (turned by 90°) studied by the GCM.

The analysis of the honeycomb reference case reveals that the controlled discharge of the adsorber leads to an advancing temperature wave with an almost constant peak value of $T_{max} < 75°C$, see Fig. 6.17 (a). At the same time, the heat transfer fluid flowing in opposite direction heats up as it

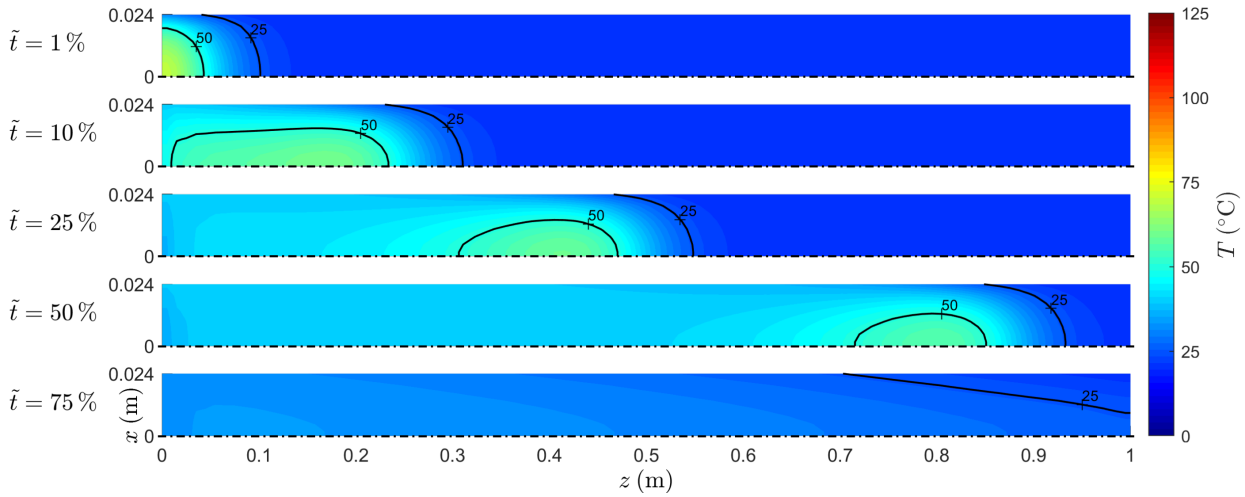

(a) Honeycomb reference case: $d_\mathrm{c} = 1\,\mathrm{mm}$, $\varepsilon = 0.\bar{1}$, $t_\mathrm{tot} = 50.4\,\mathrm{h}$.

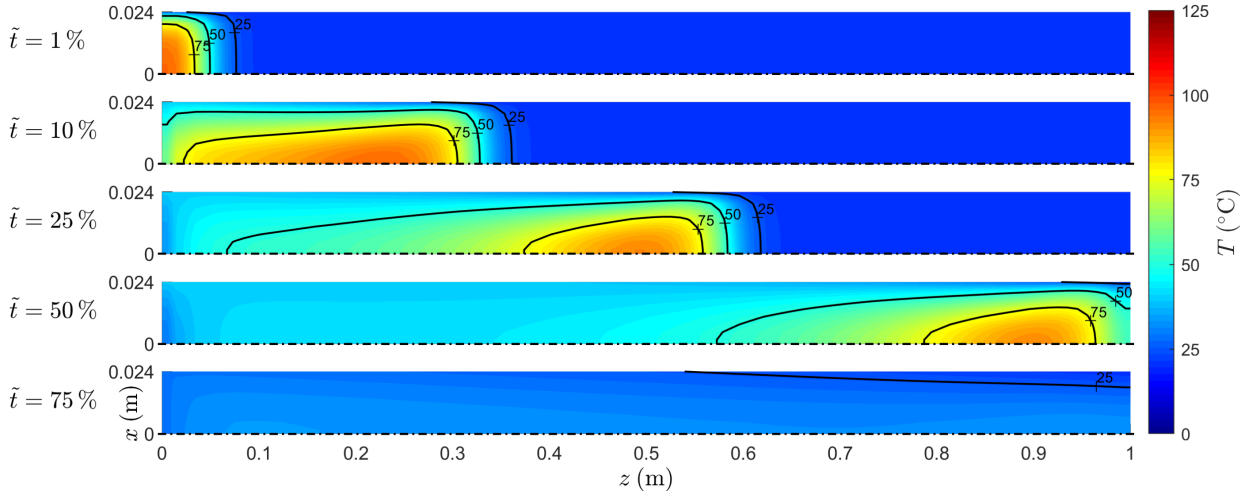

(b) Granules reference case: $d_\mathrm{p} = 2\,\mathrm{mm}$, $\varepsilon = 0.4$, $t_\mathrm{tot} = 36.7\,\mathrm{h}$.

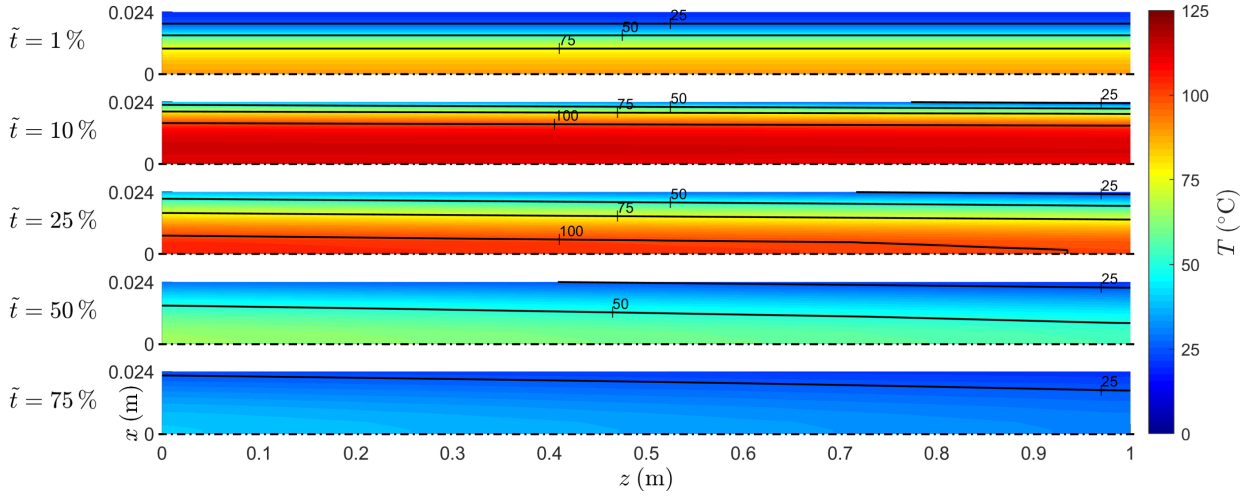

(c) Powder reference case: $d_\mathrm{p} = 50\,\mu\mathrm{m}$, $\varepsilon = 0.65$, $t_\mathrm{tot} = 32.6\,\mathrm{h}$.

Figure 6.17.: Evolution of the temperature fields $T(\boldsymbol{x}, \tilde{t})$ over the non-dimensional time $\tilde{t}$ in the studied half-section of the adsorbent bulk for the reference cases of honeycomb, granules and powder adsorbent, see Tab. 6.3.

passes the front of the temperature wave. Thus, the heat exchanger surface and consequently the region behind the advancing temperature wave remains heated-up. The temperature wave reaches the end of the adsorber already at around $\tilde{t} = 55\%$. Subsequently, the adsorbent bulk is cooled down by the heat exchanger to the inlet temperature of the heat transfer fluid.

For the granules reference case, the controlled discharge similarly leads to an advancing temperature wave, see Fig. 6.17 (b). Evaluation of Eq. (4.71) yields a permeability ratio of $\kappa_{\mathrm{pb}}/\kappa_{\mathrm{hc}} = 1.14$. Thus, the mass transport resistances for the honeycomb and granules reference cases are almost identical. Regarding the heat transport, the effective heat conductivity of the packed bed of granules can be more than 50% lower compared to the honeycomb adsorbent, see Fig. 4.12 (a) in Sect. 4.3.3. Hence, to realize the same heat transfer to the heat transfer fluid and to reach the set outlet temperature, a higher temperature gradient normal to the heat exchanger surface is required in accordance with Fourier's law (4.28). As a consequence the peak value of the temperature wave is controlled by the inlet pressure to $T_{\mathrm{max}} > 75°\mathrm{C}$. Further comparison with the honeycomb reference case shows that the temperature field is less symmetric around the wave peak. The temperature wave is stretched behind the wave peak, while the temperature gradient at the wave front is steeper. The effect results from both the lower effective heat conductivity as well as the increased speed of the advancing temperature wave. The increased speed is a result of the higher porosity of the granules adsorbent compared to the honeycomb adsorbent. Thus, the solid fraction of the adsorbent and thus the stored energy density are lower by 32.5%. Comparison of the total process durations confirms this conclusion ($t_{\mathrm{tot,hc}} = 50.4\,\mathrm{h}$, $t_{\mathrm{tot,pb}} = 36.7\,\mathrm{h}$).

The evolution of the temperature field for the powder reference case is shown in Fig. 6.17 (c). As mentioned above, the vapor is supplied from the symmetry plane for this case to overcome mass transport limitations. Comparison of the permeabilities by Eq. (4.71) confirms that the permeability of the powder reference case is significantly lower compared to the honeycomb reference case by a factor of more than 100. Due to the modified vapor supply, the temperature evolution differs substantially from the honeycomb and granules reference cases. In fact, the temperature profile in the transversal direction is more comparable to the result of the one-dimensional adsorber set-up analyzed by the SCM, see Sect. 6.1.3. The heat-up of the powder adsorbent starts from the symmetry plane, showing no distinct wave peak as well as no horizontal variation. Only as the temperature front reaches the heat exchanger surface around $\tilde{t} \approx 2\%$, the heat transfer fluid starts to extract heat from the adsorbent bulk. This leads to a slight tilt of the temperature distribution. As a result of the modified adsorber configuration, as well as the low effective heat conductivity of the powder bed, the maximum temperature in the powder reference case reaches $T_{\mathrm{max}} > 100°\mathrm{C}$. In particular, the small particle diameter leads to high Knudsen numbers $Kn > 1$, resulting in a significant decrease of the effective heat conductivity, see Fig. 4.12 (b). Again, the higher porosity results in a lower stored energy density, which reduces the total process duration to $t_{\mathrm{tot}} = 32.6\,\mathrm{h}$.

With respect to the application, the evolution of the outlet temperature of the heat transfer fluid $T_{\mathrm{htf,out}}(t)$ is of particular interest and shown in Fig. 6.18 for the three reference cases. The figure proves that the outlet temperature can be well controlled to the set value for all cases. Only for the powder case, increased temperature oscillations occur initially and the control parameter $K_{1,1}$ has to be reduced to $K_{1,1} = 0.5 \cdot 10^{-4}\,1/\mathrm{s}$. The increased oscillations occur in this case because the temperature front reaches the heat exchanger surface over the whole length at once. Moreover, the figure shows clearly that the set value of the outlet temperature can only be held for a limited time $t_{\mathrm{dc,real}}$ before the outlet temperature of the heat transfer fluid starts to decline. As discussed before, the higher porosity of the granules and powder bed constitute a lower stored energy density, which reduces the total process duration t_{tot}. In addition, the figure reveals that the outlet temperature decreases with different rates depending on the adsorbent configuration. Ideally, the outlet temperature can be held at the set value until the adsorber is fully discharged. For the granules reference case, this ideal case is depicted by the dotted line and the ideal duration is marked as $t_{\mathrm{dc,ideal}}$. The deflection from this ideal case is further discussed in Sect. 6.3.4.

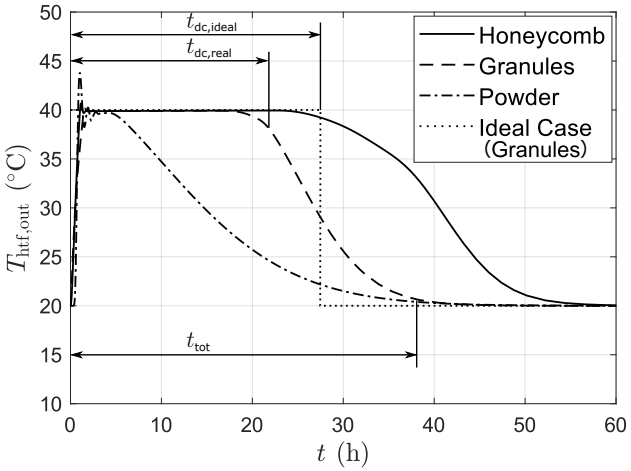

Figure 6.18.: Outlet temperature of the heat transfer fluid $T_{\mathrm{htf,out}}(t)$ versus time t for the honeycomb, granules and powder reference cases, see Tab. 6.3. In addition, the ideal discharging case is depicted for the granules (dotted line).

6.3.3. Modeling

6.3.3.1. Equilibrium Assumptions

As discussed for the MCM in Sect. 6.2.3.1, the spatial variations of temperature and pressure as well as the local deviation from the adsorption equilibrium have to be analyzed to evaluate whether equilibrium assumptions would be valid for the studied adsorber cases (see Tab. 6.3). The spatial variations can be analyzed by the maximum relative deviations from the maximum values in the adsorber. Note that the relative deviations of the temperature are evaluated on the Celsius scale. The local deviation from the adsorption equilibrium is analyzed by the maximum relative deviation from the corresponding local adsorption equilibrium. The maximum relative deviations of the temperature T, pressure p and water uptake X versus the non-dimensional time $\tilde{t}$ are shown in Fig. 6.19 for the three distinct reference cases. Nevertheless, the conclusions derived in the following apply to all cases studied by the GCM.

The analysis of the maximum relative deviations of the temperature, see Fig. 6.19 (a), reveals that the equilibrium assumption cannot be applied to the temperature. The maximum relative deviations reach up to 80% and even at the end of the process lie in the range of $4 \ldots 24\%$. In addition, the modification of the adsorber configuration for the powder reference case leads to a qualitatively different course compared to the honeycomb and granules reference cases. While for the honeycomb and granules cases the maximum relative deviations are almost constant during

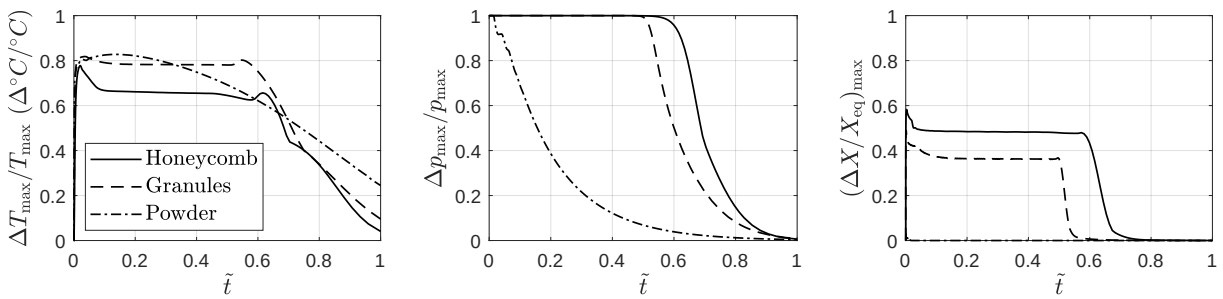

(a) Rel. deviations of temperature T. (b) Rel. deviations of pressure p. (c) Rel. deviations of water uptake X.

Figure 6.19.: Maximum relative deviations of the temperature T, pressure p and water uptake X versus the non-dimensional time $\tilde{t}$ for the three reference cases, see Tab. 6.3.

the phase of advancing temperature wave, the maximum relative deviation for the powder case constantly decreases after it has reached its maximum.

With respect to the relative deviations of the pressure, see Fig. 6.19 (b), it is found that the equilibrium assumption cannot be applied to the pressure. For the honeycomb and granules case, the maximum relative deviations are at the maximum for more than half of the process duration. Again, the powder case shows a different behavior. The maximum relative deviation decreases monotonously from the beginning of the process. Nevertheless, the maximum relative deviations for the powder case are also not negligible.

Finally, the evaluation of the relative deviations of the water uptake, see Fig. 6.19 (c), shows that local adsorption equilibrium cannot be assumed for the honeycomb and granules case, that is the limitation by the internal mass transport resistance in the zeolite adsorbent has to be considered. However, for the powder case it is valid to assume adsorption equilibrium throughout the process. This result is expected since the particle diameter of the powder particles is very small, resulting in low internal mass transport resistance, and thus a high adsorption kinetic.

6.3.3.2. Rarefaction Effects

To evaluate the relevance of rarefaction effects, that is the dependency of the permeability as well as the effective heat conductivity on the Knudsen number as described in Sect. 4.3.3, the total process durations are determined twice for the three reference cases (see Tab. 6.3): once with and once without consideration of the rarefaction effects. The determined total process durations t_{tot} versus the channel or particle diameter $d_{\mathrm{c/p}}$ for the three reference cases are shown in Fig. 6.20. The course of the total process duration is not discussed here, but is analyzed with respect to the application in the following section.

For the honeycomb and for the granules reference case, see Fig. 6.20 (a) and (b), the total process durations with and without rarefaction effects are identical for $d_{\mathrm{c/p}} \geq 2\,\mathrm{mm}$. Only for smaller diameters, the total process duration determined with rarefaction effects is lower compared to the results determined without rarefaction effects. The maximum overestimation of the total process duration due to negligence of the rarefaction effect is determined for the granules case with a particle diameter of $d_{\mathrm{p}} = 0.5\,\mathrm{mm}$ to 27%. The lower process durations determined with the rarefaction effects result from the increase of the permeability with the Knudsen number. Thus, in these cases the process is limited by the external mass vapor transport in the adsorbent bulk.

In contrast, the total process durations for the powder reference case, see Fig. 6.20 (c), show the opposite behavior and the process durations determined with the rarefaction effects are higher compared to the results without rarefaction effects. The maximum underestimation of the total process duration due to negligence of the rarefaction effect is 23%. The higher process durations determined with the rarefaction effect result from the increase of the effective heat conductivity with the Knudsen number. Thus, for the powder cases, the process is limited by the heat transport.

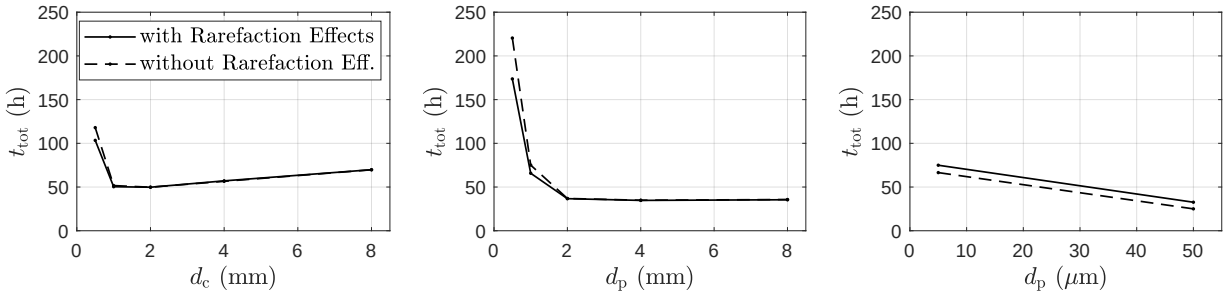

(a) Honeycomb reference case. (b) Granules reference case. (c) Powder reference case.

Figure 6.20.: Total process durations t_{tot} determined with and without rarefaction effects versus the channel or particle diameter $d_{\mathrm{c/p}}$ for the three reference cases, see Tab. 6.2.

6.3.4. Application

In TES application, one particular important parameter is the discharging temperature, that is the outlet temperature of the heat transfer fluid. Furthermore, it is of interest to which degree the stored energy can be discharged at a set discharging temperature. To evaluate this degree, a discharging degree is defined as

$$\eta_{\mathrm{dc}} := \frac{t_{\mathrm{dc,real}}}{t_{\mathrm{dc,ideal}}}, \tag{6.2}$$

where $t_{\mathrm{dc,real}}$ denotes the real and $t_{\mathrm{dc,ideal}}$ the ideal discharging duration at a set discharging temperature. For the granules reference case, this two durations are marked in Fig. 6.18. The real discharging duration is defined as the duration for which the outlet temperature of the heat transfer fluid is above 95% of the set temperature value on a Celsius-scale (here 38°C for the granules reference case with $T_{\mathrm{htf,out,set}} = 40°\mathrm{C}$). The ideal discharging duration is determined by dividing the energy stored in total by the ideal constant discharging power.

6.3.4.1. Variation of Adsorbent Configuration

The influence of the adsorbent configuration on the discharging behavior can be analyzed by the discharging degree. For this purpose, the discharging degrees are determined for honeycomb, granules and powder adsorbents of varying channel and particle diameters as defined in Tab. 6.3. The discharging conditions are set as in the reference cases to $T_{\mathrm{htf,out,set}} = 40°\mathrm{C}$ ($\Delta T_{\mathrm{htf}} = 20\,\mathrm{K}$) and $u_{\mathrm{htf}} = 1\,\mathrm{mm/s}$. The discharging degrees η_{dc} versus the channel or particle diameter $d_{\mathrm{c/p}}$ for the honeycomb and granules cases are shown in Fig. 6.21. The results of the powder cases are not depicted and further discussed since the maximum discharging degree is below 50%, and hence the thermal discharging performance is inferior to the honeycomb and granules cases.

The analysis of the honeycomb cases, see Fig. 6.21 (a), reveals that a distinct optimum of the discharging degree over the channel diameter exists around $d_{\mathrm{c}} = 2\,\mathrm{mm}$. The maximum discharging degree is approximately 80%. For smaller channel diameters, the achievable discharging degree decreases rapidly. With increasing diameter, the discharging degree decreases almost linearly, but with a lower slope. The results are in accordance with the results observed for the cases studied MCM, which found an optimum of the thermal power, see Sect. 6.2.4.1. Thus, the explanation of the local optimum is similar. The local optimum can be explained by mass transport and adsorption

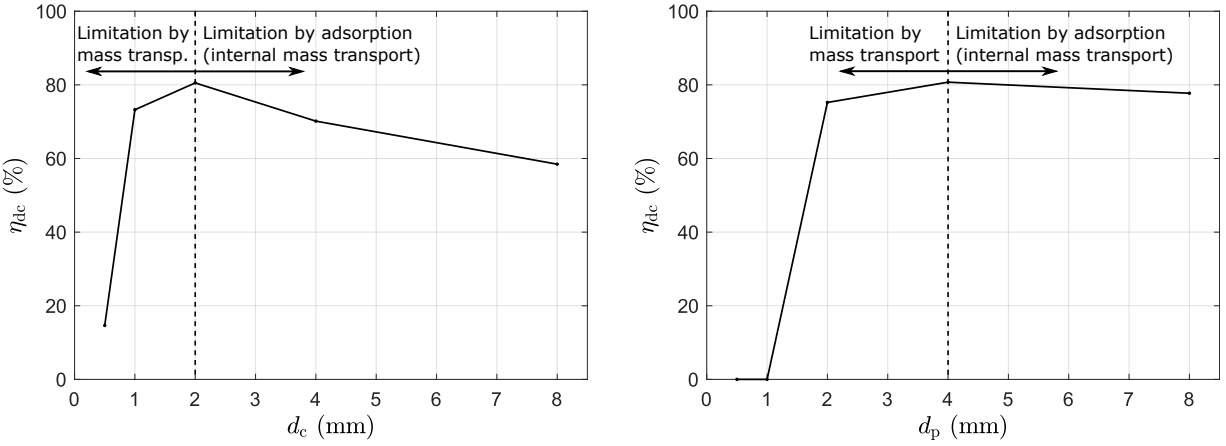

(a) Honeycomb cases. (b) Granules cases.

Figure 6.21.: Discharging degrees η_{dc} versus the channel or particle diameter $d_{\mathrm{c/p}}$ for the honeycomb and granules cases as defined in Tab. 6.3. The discharging conditions are set as in the reference cases to $T_{\mathrm{htf,out,set}} = 40°\mathrm{C}$ ($\Delta T_{\mathrm{htf}} = 20\,\mathrm{K}$) and $u_{\mathrm{htf}} = 1\,\mathrm{mm/s}$.

limitations. Left of the optimum, the discharging degree is limited by the mass transport, that is the vapor flow in the honeycomb channels. Reducing the channel diameters, reduces the permeability, see Eq. (4.67). To the right of the optimum, the discharging degree is limited by the adsorption, that is the internal mass transport by diffusion in the zeolite adsorbent. Since the porosity is set to a constant value, increased channel diameters constitute increased web thickness, thus reducing the adsorption kinetics.

The results for the granules cases are given in Fig. 6.21 (b). In general, the same behavior as for the honeycomb adsorbent is observed. An optimum exists which can be explained as before by mass transport and adsorption limitations. However, the optimum is not as distinct and shifted to a higher particle diameter of around $d_\mathrm{p} = 4\,\mathrm{mm}$. Still, the maximum discharging degree is around 80%. For smaller particle diameters, the discharging degree also decreases rapidly and drops to 0% for $d_\mathrm{p} \leq 1\,\mathrm{mm}$. A discharging deficiency of 0% occurs if the set temperature cannot be reached at any time. Nevertheless, thermal energy is discharged from the adsorber but on an insufficient temperature level. For bigger particle diameters a slight decrease of the discharging degree also occurs. However, since the granules adsorbent has a higher surface to volume ratio compared to the honeycomb, the process is less limited by the adsorption. Thus, the discharging degree decreases less with increasing diameter.

6.3.4.2. Variation of Discharging Conditions

To study the influence of the discharging conditions, the discharging degree is evaluated. The discharging conditions can be varied by two parameters: the discharging temperature, that is the set outlet temperature of the heat transfer fluid $T_\mathrm{htf,out,set}$, and the mean velocity of the heat transfer fluid u_htf in the heat exchanger plates. The mean velocity of the heat transfer fluid can be converted to the more practical parameter of volume flow of heat transfer fluid per storage volume. Here, in comparison to the definition of the volumetric thermal power for the MCM in Sect. 6.2.4, the volume of the adsorbent bulk as well as the volume of the heat transfer fluid and the volume of the heat exchanger plates are taken into account. The thickness of the heat exchanger metal sheets is assumed to be 1.5 mm. With this, the varied velocity of $u_\mathrm{htf} = 0.5 \ldots 2\,\mathrm{mm/s}$ converts to a specific volume flow of $\dot{v}_\mathrm{htf} = 100 \ldots 400\,\mathrm{Liter/m^3h}$. The volumetric thermal power reads

$$p_\mathrm{th} = \rho_\mathrm{htf} \dot{v}_\mathrm{htf} c_\mathrm{htf} \left(T_\mathrm{htf,out,set} - T_\mathrm{htf,in}\right) = \rho_\mathrm{htf} \dot{v}_\mathrm{htf} c_\mathrm{htf} \Delta T_\mathrm{htf}. \tag{6.3}$$

Thus, the thermal power can be increased by increasing the discharging temperature and by increasing the specific volume flow of the heat transfer fluid, see Fig. 6.22. For the studied parameter range the volumetric thermal power lies in the range of $1.2 \ldots 18.5\,\mathrm{W/m^3}$.

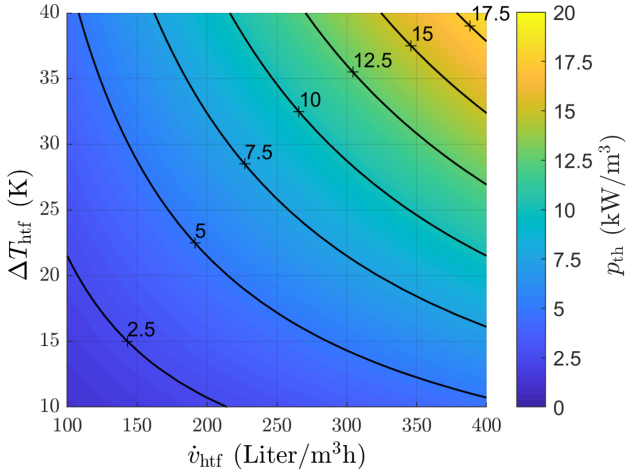

Figure 6.22.: Volumetric thermal power p_th for the granules cases as defined in Tab. 6.3 versus specific volume flow $\dot{v}_\mathrm{htf}$ and temperature lift ΔT_htf of the heat transfer fluid.

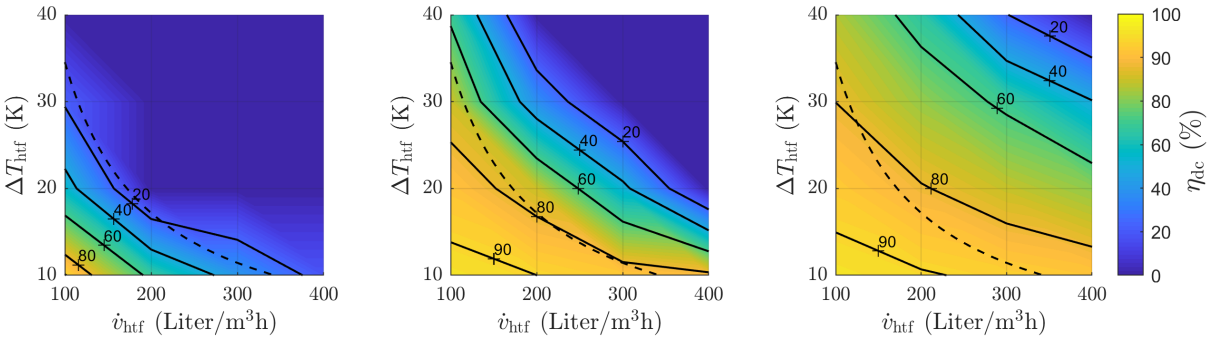

(a) Particle diameter $d_{\mathrm{p}} = 1\,\mathrm{mm}$. (b) Particle diameter $d_{\mathrm{p}} = 2\,\mathrm{mm}$. (c) Particle diameter $d_{\mathrm{p}} = 4\,\mathrm{mm}$.

Figure 6.23.: Discharging degrees η_{dc} for the granules cases as defined in Tab. 6.3 versus specific volume flow $\dot{v}_{\mathrm{htf}}$ and temperature lift ΔT_{htf} of the heat transfer fluid. The dashed line marks the contour line of the volumetric thermal power at $p_{\mathrm{th}} = 4\,\mathrm{kW/m^3}$.

The results of the discharging degrees η_{dc} for the granules cases as defined in Tab. 6.3 versus the specific volume flow $\dot{v}_{\mathrm{htf}}$ and temperature lift ΔT_{htf} of the heat transfer fluid are given in Fig. 6.23 for the particle diameters of $d_{\mathrm{p}} = 1\,\mathrm{mm}$, $2\,\mathrm{mm}$ and $4\,\mathrm{mm}$. The results yield the general result that higher the thermal power (higher $\dot{v}_{\mathrm{htf}}$ and/or higher ΔT_{htf}) induces lower discharging degree. Furthermore, for all three examined particle diameters a range of process parameters exists for which the discharging degree drops to 0%.

For a particle diameter of $d_{\mathrm{p}} = 1\,\mathrm{mm}$, see Fig. 6.23 (a), discharging degrees above 80% can be achieved only for low thermal power with the maximum discharging degree of 91% in the studied range. The discharging degree decreases fast with increasing thermal power and drops to 0% at a thermal power above $\approx 4\,\mathrm{W/m^3}$. Moreover, the figure reveals that the discharging degree decreases sharper with increasing temperature lift than with increased volume flow of the heat transfer fluid.

Doubling the particle diameter to $d_{\mathrm{p}} = 2\,\mathrm{mm}$, see Fig. 6.23 (b), the maximum discharging degree only increases slightly to 93%. However, the discharging degrees at higher discharging powers are increased significantly. For example, for thermal powers of $\approx 4\,\mathrm{W/m^3}$ the discharging degrees lie in the range of $\approx 60 \ldots 80\%$.

Further increase of the particle diameter to $d_{\mathrm{p}} = 4\,\mathrm{mm}$, see Fig. 6.23 (c), extends the discharging degree region of $\approx 60 \ldots 80\%$ even more to higher thermal powers. However, the maximum discharging degree does not increase above 93%. As for the smaller particle diameters, it is not possible to discharge the storage with the maximum thermal power of the studied range ($p_{\mathrm{th,max}} \approx 18.5\,\mathrm{W/m^3}$).

For the maximum studied particle diameter of $d_{\mathrm{p}} = 8\,\mathrm{mm}$, only a small change compared to the cases with $d_{\mathrm{p}} = 4\,\mathrm{mm}$ is observed. Finally, increasing the inlet pressure, increases the discharging degrees, allowing for higher discharging power, compare Fig. 6.15 (a) in Sect. 6.2.4.2.

6.3.5. Charging Process

The focus of this work is on the discharging process, that is the adsorption process. Nevertheless, to close the results discussion of the GCM, one charging process, that is desorption process, is analyzed. As an exemplary case, a honeycomb adsorber is examined. The geometry parameters are set as for the honeycomb reference case, see Tab. 6.3. With respect to the process parameters, the boundary and initial conditions are set to typical charging conditions, compare Sect. 1.2. The implemented values are summarized in Tab. 6.4.

The outlet pressure p_{out} is not controlled but set to a constant value. Therefore, no boundary condition regarding the temperature reduction of the heat transfer fluid is defined. Additionally, the definition of the vapor temperature at the outlet is not required anymore since the vapor flows out of the adsorber during desorption. In contrast to the previously studied discharging cases, the

Table 6.4.: Process parameters of the honeycomb adsorber charging case studied by the GCM. The geometry parameters are set as for the honeycomb reference case, see Tab. 6.3.

Parameter	Value	Unit
Boundary Conditions		
p_{out}	20	mbar
$T_{\mathrm{htf,in}}$	180	°C
$u_{\mathrm{htf,in}}$	1.0	mm/s
Initial Conditions		
p_0	20	mbar
T_0	20	°C
$X_0 = X_{\mathrm{eq}}$	0.34	kg/kg

flow direction of the heat transfer fluid is now from left to right. In general, this allows for a more efficient charging process since the pressure increase due to the released vapor is reduced. A lower pressure corresponds to a lower adsorption equilibrium of the water uptake, hence accelerating the desorption. However, since the direction of the vapor flow in the adsorbent bulk is also inverted, it is still opposite to the flow direction of the heat transfer fluid. Finally, to ensure numerical stability, the inlet temperature of the heat transfer fluid is not implemented as a sudden temperature jump but is increased linearly to its maximum value over a duration of $t = 2\,\mathrm{h}$. This modification is acceptable, as in practical application with solar thermal heat supply, a similar finite heat-up time would also be required in the morning hours during sunrise [124].

The evolution of the symmetric temperature $T(\boldsymbol{x}, \tilde{t})$, pressure $p(\boldsymbol{x}, \tilde{t})$ and water uptake $X(\boldsymbol{x}, \tilde{t})$ fields during charging are shown in Fig. 6.24 for a half-section of the studied honeycomb adsorber. The analysis of the temperature, see Fig. 6.24 (a), shows that the honeycomb adsorbent is gradually heated up. Due to the heat transport limitations in the honeycomb adsorbent, the heat-up of the honeycomb center is delayed. Furthermore, the heat-up process is generally prolonged by the internal heat sink resulting from the desorption. The total process duration required to completely heat up the honeycomb adsorbent is $t_{\mathrm{tot}} \approx 24\,\mathrm{h}$. In comparison, the heat-up time of the same honeycomb adsorbent without desorption would be $t \approx 8\,\mathrm{h}$. With respect to practical application, the charging process of the studied honeycomb adsorber case would require several days.

The evaluation of the pressure, see Fig. 6.24 (b), shows that the pressure significantly increases locally up to $p \geq 30\,\mathrm{mbar}$. The pressure increase results from the vapor released by the desorption. The desorption, and thus the vapor release, is linked to the temperature by the adsorption equilibrium, see Eq. (4.32). Therefore, the initial pressure increase is at a maximum at the heat exchanger boundary and at a minimum at the honeycomb center. However, as the desorption completes earlier at the heat exchanger boundary due to the initially higher desorption rate, the pressure in the honeycomb center exceeds the pressure at the heat exchanger surface later in the process. With respect to the granules case, the transversal pressure gradient is not so prominent since the packed bed allows for a transversal vapor flow and thus pressure equalization.

Regarding the water uptake, see Fig. 6.24 (c), it is found that the distribution is inverse to the temperature distribution. Thus, the water uptake is mainly dependent on the temperature for the studied charging case. As discussed for the pressure, the desorption rate is higher at the heat exchanger boundary compared to the honeycomb center. Therefore, the water uptake decreases faster at the heat exchanger boundary. At the end of the process, a state of uniform distribution of the water uptake with $X = 0.1\,\mathrm{kg/kg}$ is reached.

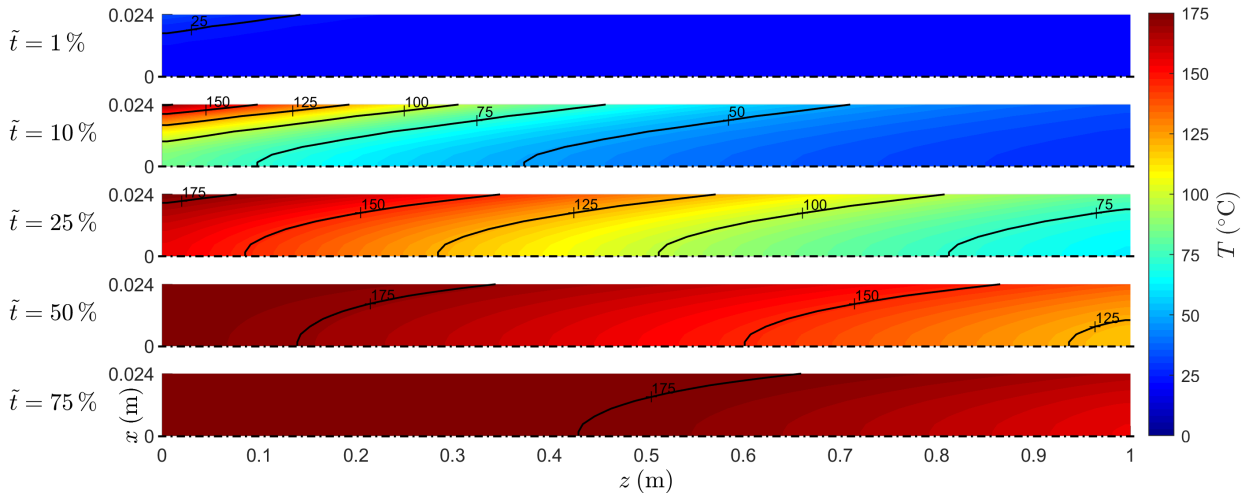

(a) Evolution of the symmetric temperature field $T(\boldsymbol{x}, \tilde{t})$ over the non-dimensional time $\tilde{t}$.

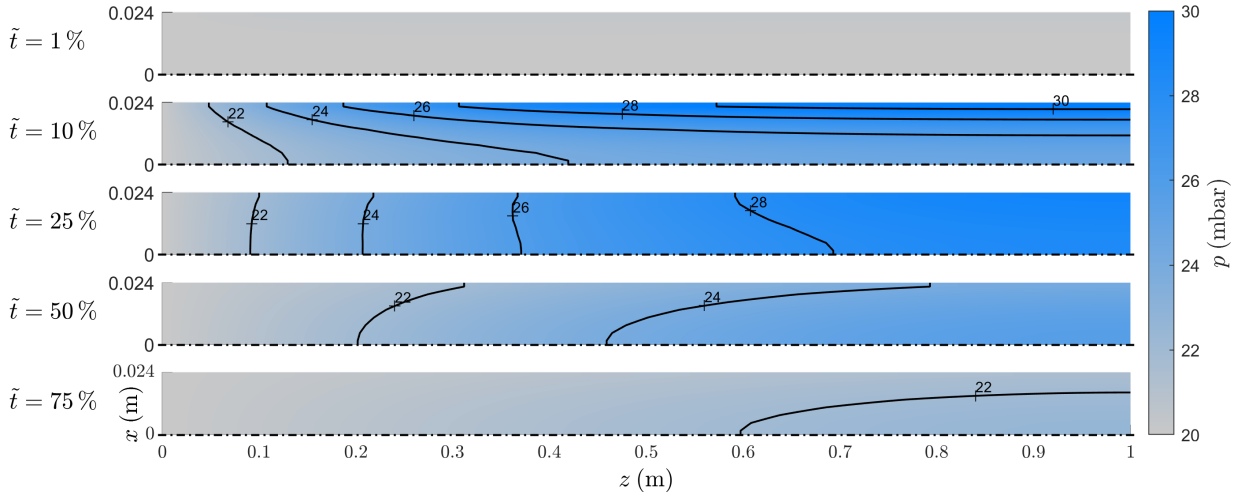

(b) Evolution of the symmetric pressure field $p(\boldsymbol{x}, \tilde{t})$ over the non-dimensional time $\tilde{t}$.

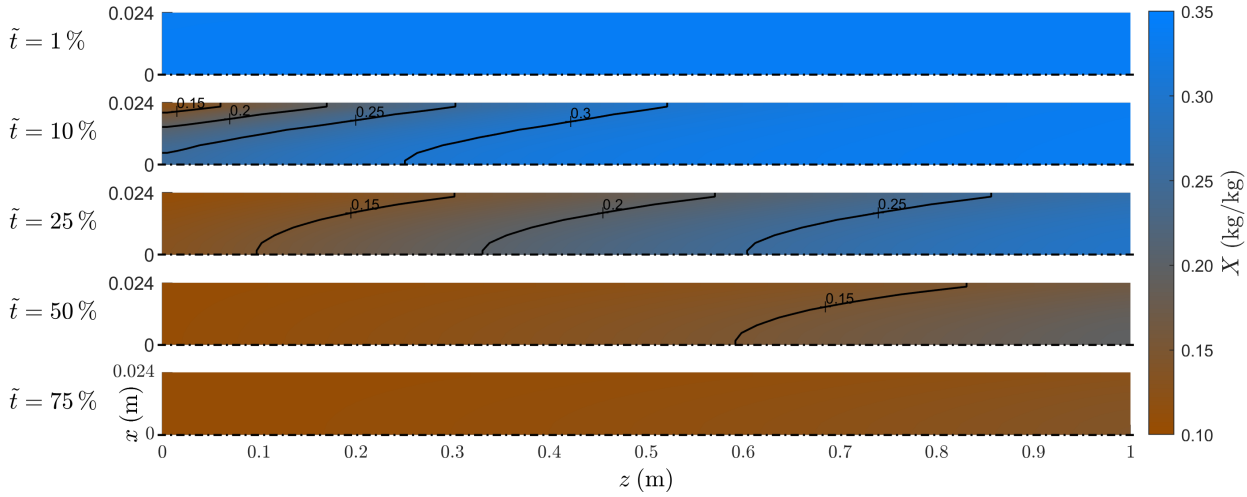

(c) Evolution of the symmetric water uptake field $X(\boldsymbol{x}, \tilde{t})$ over the non-dimensional time $\tilde{t}$.

Figure 6.24.: Evolution of the symmetric temperature $T(\boldsymbol{x}, \tilde{t})$, pressure $p(\boldsymbol{x}, \tilde{t})$ and water uptake $X(\boldsymbol{x}, \tilde{t})$ fields over the non-dimensional time $\tilde{t}$ in a half-section of the honeycomb block for the charging case, see Tab. 6.4.

6.4. Model Comparison

To close the results discussion, the SCM, MCM and GCM are compared by some selected results. Since the adsorber configuration studied by the SCM differs from the MCM and GCM in terms of the heat exchanger design (see Sect. 4.1.1, 4.2.1 and 4.3.1), the comparability of the SCM results to the MCM and GCM results is limited. Since the heat extraction is restricted to the closed end of the honeycomb arrangement in the SCM, the model predicts an almost instant heat-up of the whole honeycomb ($\tilde{t} \approx 0.15\%$) to its maximum temperature ($T_{\max} = 136°C$ for the reference case, see Tab. 6.1) before the honeycomb is cooled down, see Fig. 6.4 (a). In comparison, for the reference cases with a honeycomb length of $L = 1\,\mathrm{m}$ (see Tab. 6.2 and 6.3), the MCM and the GCM only predict a short initial heat-up of the front part of the honeycomb to a maximum temperature of around $T_{\max} \approx 125°C$, see Fig. 6.9 (a). Subsequently, due to the heat extraction along the sides of the honeycomb, the maximum temperature for the rest of the process is below $T < 75°C$. Moreover, the relative time required for the temperature wave to reach the end of the honeycomb is around $\tilde{t} \approx 50\%$. For the controlled case, the temperature never exceeds $T < 75°C$, see Fig. 6.16. Finally, the impact of the different heat exchanger designs is most obvious for the total process duration. While the SCM predicts a total process duration for the reference case of $t_{\mathrm{tot}} = 427\,\mathrm{days}$, the MCM predicts a total process duration of only $t_{\mathrm{tot}} = 2.3\,\mathrm{h}$ for the comparable reference case. In summary, the adsorber configuration studied by the SCM is primarily limited by the heat transport, whereas the adsorber configuration studied by the MCM and GCM dependents on both the mass and heat transport as well as the adsorption.

The main difference between the MCM and the GCM is also related to the heat exchanger. While the surface temperature of the heat exchanger is assumed to a constant value of $T_{\mathrm{htx}} = 20°C$ for the MCM, the GCM includes the heat-up of the heat transfer fluid along the heat exchanger plate. Thus, the surface temperature of the heat exchanger varies along the heat exchanger plate in the GCM. The impact of this different heat exchanger boundary condition is clear for the controlled cases, see Fig. 6.16 and Fig. 6.17 (a). The MCM predicts an instant cooling of the region behind the advancing temperature wave, whereas this region remains heated up for the GCM until the temperature wave reaches the end of the honeycomb. As a consequence, the MCM predicts slightly higher thermal powers and lower total process durations.

Regarding the evaluation of modeling aspects, both models confirm that equilibrium assumptions must not be applied for the studied closed low-pressure adsorbers of a length of $L = 1\,\mathrm{m}$. Only for a few particular cases with a length of $L = 0.1\,\mathrm{m}$, the MCM results showed that it would be valid to assume pressure and adsorption equilibrium. With respect to the rarefaction effects, both models revealed that the slip effect can be relevant for small channel and particle diameters. However, Knudsen effects beyond the slip regime are found to be negligible. Only for the powder case, the Knudsen effect has to be considered for the whole Knudsen range.

Regarding the evaluation of application aspects, both models predicted that the discharging process can be optimized by variation of the channel diameter. While the optimization was analyzed for the volumetric thermal power in the case of the MCM, the GCM was analyzed in terms of a defined discharging degree (see Eq. (6.2)). The MCM predicts that the optimum channel diameter for maximum thermal power is around $d_{\mathrm{c}} \approx 4\,\mathrm{mm}$ for a honeycomb length of $L = 1\,\mathrm{m}$. In comparison, the GCM predicts that the optimum channel diameter for maximum discharging degree is around $d_{\mathrm{c}} \approx 2\,\mathrm{mm}$. Furthermore, since the GCM, in contrast to the MCM, considers the heat transfer fluid, the influence of the discharging conditions on the discharging degree can be evaluated.

Finally, to simulate honeycomb adsorbents the square channels are transformed to circular channels in the GCM. This allows to deploy the general Poiseuille coefficient G_{P} for circular channels (see Eq. (4.25)) for all three studied adsorbent configurations: honeycomb, granules and powder. To analyze the possible impact of this transformation for the honeycomb case, the evolution of the temperature calculated by the GCM is compared to the results determined with the MCM. The results are compared for the honeycomb reference case without control, deploying a constant surface temperature of the heat exchanger, see Tab. 6.2. The evolution of the symmetric temperature fields

$T(\boldsymbol{x}, \tilde{t})$ over the non-dimensional time $\tilde{t}$ in a half-section of the honeycomb block determined by the GCM for the reference case of the MCM (see Tab. 6.2) is shown in Fig. 6.25. The non-dimensional time is defined with the total process duration determined by the MCM so that the results are directly comparable. Comparison of the temperature fields calculated by the GCM to the temperature fields determined by the MCM, see Fig. 6.9 (a), reveals that the temperature wave advances slightly faster for the MCM. Therefore, it can be concluded that the geometry transformation leads to a slight underestimation of the mass transport in the square channels of the honeycomb. Nevertheless, the predicted temperature fields are almost identical. However, the results indicate that for honeycomb adsorbents with rectangular channels the MCM should be applied as it provides a more accurate prediction of the the mass transport in the honeycomb channels.

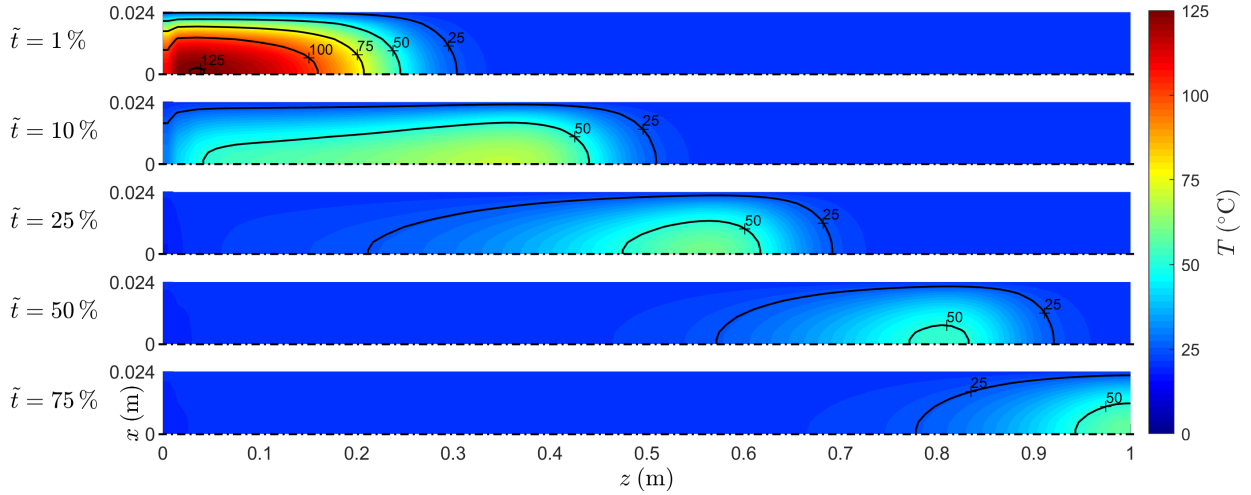

Figure 6.25.: Evolution of the symmetric temperature fields $T(\boldsymbol{x}, \tilde{t})$ over the non-dimensional time $\tilde{t}$ in a half-section of the honeycomb block determined by the GCM for the reference case of the MCM, see Tab. 6.2. The non-dimensional time is defined with the total process duration determined by the MCM.

7. Summary

Closed low-pressure adsorbers for thermal energy storage (TES) have been modeled and simulated in this thesis. The focus was on the discharging process. As the adsorption pair, binderless zeolite 13X with water was examined. A stepwise model development from pore to storage scale was conducted: Single Channel Model (SCM), Multi Channel Model (MCM) and General Continuum Model (GCM). The stepwise model development allowed for an accurate description of the underlying physical processes. The Finite Difference Method was implemented to numerically solve the models. Simulations were conducted for defined reference cases as well as over a range of geometry and process parameters.

Through the detailed analysis of the reference cases, a better understanding of the transport processes in closed low-pressure adsorbers was gained, particularly for adsorbers of larger scale ($L = 0.1 \ldots 1\,\mathrm{m}$) as in TES applications. Furthermore, the results were analyzed with respect to two particular modeling aspects: equilibrium assumptions and rarefaction effects. With respect to the application, the discharging performance was analyzed in terms of thermal power and a defined discharging degree. Both the adsorber configuration (main dimensions, vapor supply and heat extraction) and the adsorbent configuration (macroscopic adsorbent dimensions and structure: powder, granules, honeycomb) have been varied. In addition, the effect of the discharging conditions was evaluated. Finally, one exemplary charging process was examined.

Conclusions

The detailed analysis of the reference cases for the SCM, MCM and GCM revealed that the mass and heat transport and the adsorption processes are strongly coupled and can only be understood in their interaction. During discharging, the vapor flowing into the adsorber is being adsorbed, leading to an advancing adsorption front, which in turn results in a simultaneously advancing temperature front or wave. The increased temperature shifts the adsorption equilibrium, thus reducing the adsorption rate, which again strongly effects the advancement of the inflowing vapor.

For one-dimensional adsorber configurations as studied by the SCM, that is the mass and heat transport are in the same direction, the discharging process is generally limited by the heat transport. Only for short adsorber lengths ($L < 0.1\,\mathrm{m}$), the process can additionally become limited by the adsorption, that is the internal mass transport resistance in the zeolite adsorbent. This fundamental finding confirms the results reported in manifold publications on small-scale closed adsorbers for heat pump application. However, for large-scale adsorbers required for TES application, one-dimensional adsorber configurations lead to insufficient thermal power and unsuitable discharging durations of up to one year.

In contrast, for two-dimensional adsorber configurations as studied by the MCM and GCM, that is the mass and heat transport are in perpendicular directions, the discharging process can be limited either by the mass or heat transport or by the adsorption. The limitation depends on the configuration of the adsorber and adsorbent. Moreover, two-dimensional adsorber configurations can provide sufficient thermal power and reasonable discharging durations for domestic heating applications.

In the introduction, specific questions regarding the modeling and application were formulated. These questions together with the derived answers are given below:

Modeling:

- Is it valid to apply equilibrium assumptions (e. g. uniform pressure assumption)?
  For one-dimensional adsorber configurations, it is valid to assume a uniform pressure distribution throughout the adsorber as long as the details of the relatively short initial mass transport process are not of interest. In any case, the temperature distribution has to be considered since the discharging process is determined by the heat transport. Further, the local deviation from adsorption equilibrium, that is the limitation by the internal mass transport resistance in the zeolite adsorbent, should be taken into account for adsorbers of short length ($L < 0.1\,\mathrm{m}$). In contrast, for two-dimensional adsorber configurations (adsorber length $L \geq 0.1\,\mathrm{m}$), no equilibrium assumptions can be applied in general. Only for honeycomb adsorbers of short length ($L = 0.1\,\mathrm{m}$), large channel diameter and high porosity, the assumption of a uniform pressure distribution and local adsorption equilibrium could be applied. Finally, for powder adsorbent it is always valid to assume local adsorption equilibrium.

- Is it required to take rarefaction effects (e. g. slip effect) due to the low pressure into account?
  For most studied cases, the Knudsen number reaches from the no-slip up to the free molecular regime for a substantial part of the discharging process. However, the influence of the rarefaction effects is found to be rather low. This is explained by the fact that the major part of the mass transport occurs in the no-slip and slip regime and only a relatively little or even negligible share of mass transport occurs in the transition and free molecular regime. More specifically, for one-dimensional adsorber configurations, the slip effect was found to be irrelevant, since the discharging process is solely determined by the heat transport. The results for the two-dimensional adsorber configurations with honeycombs and granules showed that the slip effect is only relevant for small channel and particle diameters ($d_{\mathrm{c/p}} \leq 1\,\mathrm{mm}$). The negligence of the slip effect leads to an overestimation of the discharging duration of up to 27%. For the case of powder adsorbent, the effect of the rarefaction is vice versa, that is the discharging duration is increased since the effective heat conductivity in the packed bed is reduced. Finally, the thermal creep effect is found to be generally negligible.

Application:

- How does the adsorber configuration (e. g. adsorber length) influence the discharging?
  In general, for one-dimensional adsorber configurations, the thermal power decreases with increasing adsorber length while the discharging duration increases. Similarly, for two-dimensional adsorber configurations, the volumetric thermal power decreases with increasing adsorber length. However, the effect on the total thermal power is relatively low. Furthermore, the volumetric thermal power decreases with increasing width between the parallel heat exchanger plates. For example, for honeycomb adsorbers of a length $L = 0.1\,\mathrm{m}$ the peak power can reach up to $p_{\mathrm{th,peak}} = 700\,\mathrm{kW/m^3}$ in the studied ranges, while increasing the length to $L = 1\,\mathrm{m}$ reduces the peak power to below $p_{\mathrm{th,peak}} < 100\,\mathrm{kW/m^3}$. For the examined discharging processes with power control ($L = 1\,\mathrm{m}$), the thermal power is constant and the achievable volumetric thermal power lies in the range of $p_{\mathrm{th}} \approx 1 \ldots 10\,\mathrm{kW/m^3}$.

- How does the adsorbent configuration (e. g. particle diameter) influence the discharging?
  For one-dimensional adsorber configurations, the variation of the channel diameter has no effect or only little effect in the case of a short adsorber length ($L = 0.01\,\mathrm{m}$). In contrast, for two-dimensional adsorber configurations, the influence of the adsorbent configuration on the discharging performance is significant. For a set adsorber configuration and a fixed adsorbent porosity, the volumetric thermal power can be optimized by variation of the channel or particle diameter. The optimum is a result of the mass transport and adsorption limitations, decreasing and increasing respectively with the channel or particle diameter. Interestingly, the optima for peak and mean power do not coincide. Therefore, the optimization has to be applied for either the peak or the mean power. With respect to the aspect ratio of

width to height of the rectangular honeycomb channels, the thermal power increases with increasing aspect ratio (constant channel height) due to the enhanced mass transport in the channel. Moreover, arranging the heat exchanger plates parallel to the smaller side of the channels further increases the thermal power due to the higher effective heat conductivity of the honeycomb in the transversal direction. In general, the same conclusions apply to the discharging degree.

- How do the discharging conditions (e. g. discharging temperature) influence the discharging? For the two-dimensional adsorber configurations, the discharging degree is found to strongly depend on the discharging conditions in terms of discharging temperature and volume flow of the heat transfer fluid, extracting the heat from the adsorber. In general, the discharging degree decreases with increasing discharging temperature, that is with increasing temperature lift of the heat transfer fluid. Similarly, the discharging degree decreases with increasing volume flow of the heat transfer fluid. In comparison, the discharging degree decreases slightly steeper with the discharging temperature. The maximum discharging degree is $\eta_{\mathrm{dc}} = 93\%$ in the studied range, corresponding to a constant volumetric thermal power of $p_{\mathrm{th}} \approx 1\,\mathrm{kW/m^3}$. The discharge with a constant volumetric thermal power of $p_{\mathrm{th}} \approx 5\,\mathrm{kW/m^3}$ can be realized with a discharging degree of around 80%.

Finally, the analysis of an exemplary charging process of a honeycomb adsorber revealed that the pressure in the adsorber can increase by more than 50% (10 mbar) due to the desorption.

Outlook

Through this thesis, a deep understanding of the transport processes in closed low-pressure adsorbers was gained and comprehensive answers to specific questions regarding modeling and application were found. Nevertheless, the following further studies are suggested:

- To make the derived model available for advanced engineering tasks, e. g. more complex heat exchanger design, the model could be implemented in a three-dimensional numerical solver.
- To facilitate energy system simulations, e. g. complete building simulations, models of reduced dimension (0D) could be derived by parameter studies from the present model.
- To contribute to the material research, the model could be extended on the sub-scales to explicitly describe the transport processes in the micro-porous adsorbent.
- A fundamental experiment should be set up to validate the derived system of coupled model equations. In this context, the observed temporary pressure plateau at the closed end of the adsorber during discharging could be studied in detail and the hypothesis that this plateau offers a novel approach to determine adsorbent properties (e. g. tortuosity) could be verified.
- Finally, the charging process could be studied in more detail and the model could be applied to other applications (e. g. sauna storage heater).

Bibliography

[1] B. D. Solomon and K. Krishna. The coming sustainable energy transition: History, strategies, and outlook. *Energy Policy*, 39(11):7422–7431, 2011.

[2] A. B. Gallo, J. R. Simoes-Moreira, H. K. M. Costa, M. M. Santos, and E. Moutinho dos Santos. Energy storage in the energy transition context: A technology review. *Renewable and Sustainable Energy Reviews*, 65:800–822, 2016.

[3] H. Ibrahim, A. Ilinca, and J. Perron. Energy storage systems: Characteristics and comparisons. *Renewable and Sustainable Energy Reviews*, 12(5):1221–1250, 2008.

[4] N. Hartmann, O. Vöhringer, C. Kruck, and L. Eltrop. Simulation and analysis of different adiabatic compressed air energy storage plant configurations. *Applied Energy*, 93:541–548, 2012.

[5] A. Thess. Thermodynamic efficiency of pumped heat electricity storage. *Physical Review Letters*, 111(11), 2013.

[6] G. Alva, Y. Lin, and G. Fang. An overview of thermal energy storage systems. *Energy*, 144:341–378, 2018.

[7] L. F. Cabeza. *Advances in Thermal Energy Storage Systems: Methods and Applications*. Elsevier, 2014.

[8] M. Linder. Using thermochemical reactions in thermal energy storage systems. In L. F. Cabeza, editor, *Advances in Thermal Energy Storage Systems : Woodhead Publishing Series in Energy*, pages 357–374. Woodhead Publishing, 2015.

[9] F. Kuznik, K. Johannes, C. Obrecht, and D. David. A review on recent developments in physisorption thermal energy storage for building applications. *Renewable and Sustainable Energy Reviews*, 94:576–586, 2018.

[10] K. E. N'Tsoukpoe, G. Restuccia, T. Schmidt, and X. Py. The size of sorbents in low pressure sorption or thermochemical energy storage processes. *Energy*, 77:983–998, 2014.

[11] R. Westermann and C. Richter. dena-Gebäudereport kompakt 2018: Statistiken und Analysen zur Energieeffizienz im Gebäudebestand. *DENA - Deutsche Energie-Agentur GmbH*, 2018.

[12] U. Eicker. *Solare Technologien für Gebäude: Grundlagen und Praxisbeispiele*. Viewg+Teubner, 2011.

[13] R. Köll, W. van Helden, G. Engel, W. Wagner, B. Dang, J. Jaenchen, H. Kerskes, T. Badenhop, and T. Herzog. An experimental investigation of a realistic-scale seasonal solar adsorption storage system for buildings. *Solar Energy*, 155:388–397, 2017.

[14] N. Yu, R. Z. Wang, and L. W. Wang. Sorption thermal storage for solar energy. *Progress in Energy and Combustion Science*, 39(5):489–514, 2013.

[15] K. E. N'Tsoukpoe, H. Liu, N. Le Pierrès, and L. Luo. A review on long-term sorption solar energy storage. *Renewable and Sustainable Energy Reviews*, 13(9):2385–2396, 2009.

[16] B. Mette, H. Kerskes, H. Drück, and H. Müller-Steinhagen. Experimental and numerical investigations on the water vapor adsorption isotherms and kinetics of binderless zeolite 13X. *International Journal of Heat and Mass Transfer*, 71:555–561, 2014.

[17] B. Mette. *Experimentelle und numerische Untersuchungen zur Reaktionsführung thermochemischer Energiespeicher*. Dissertation, 2014.

[18] P. Tatsidjodoung, N. Le Pierrès, J. Heintz, D. Lagre, L. Luo, and F. Durier. Experimental and numerical investigations of a zeolite 13X/water reactor for solar heat storage in buildings. *Energy Conversion and Management*, 108:488–500, 2016.

[19] F. Akhtar, L. Andersson, S. Ogunwumi, N. Hedin, and L. Bergström. Structuring adsorbents and catalysts by processing of porous powders. *Journal of the European Ceramic Society*, 34(7):1643–1666, 2014.

[20] B. Formisano and C. Bonten. Extruded zeolitic honeycombs for sorptive heat storage. *AIP Conference Proceedings*, 1779:030003–1–5, 2016.

[21] L. D. Landau and E. M. Lifshitz. *Mechanics: Volume 1.* Course of Theoretical Physics S. Butterworths-Heinemann, 1976.

[22] L. D. Landau and E. M. Lifshitz. *Fluid Mechanics: Volume 6.* Course of Theoretical Physics S. Butterworths-Heinemann, 1987.

[23] K. Hutter and Y. Wang. *Fluid and Thermodynamics: Volume 1: Basic Fluid Mechanics.* Springer, 2016.

[24] K. Hutter and Y. Wang. *Fluid and Thermodynamics: Volume 2: Advanced Fluid Mechanics and Thermodynamic Fundamentals.* Springer, 2016.

[25] R. B. Bird, W. E. Stewart, and E. N. Lightfoot. *Transport Phenomena.* John Wiley & Sons, 2007.

[26] A. Beskoek and G. E. Karniadakis. A model for flows in channels, pipes, and ducts at micro and nano scales. *Microscale Thermophysical Engineering*, 3(1):43–77, 1999.

[27] A. Beskoek, G. E. Karniadakis, and W. Trimmer. Rarefaction and compressibility effects in gas microflows. *Journal of Fluids Engineering-Transactions of the ASME*, 118(3):448–456, 1996.

[28] C. Shen. *Rarefied Gas Dynamics: Fundamentals, Simulations and Micro Flows.* Heat and Mass Transfer. Springer, 2005.

[29] F. Sharipov and V. Seleznev. Data on internal rarefied gas flows. *Journal of Physical and Chemical Reference Data*, 27(3):657, 1998.

[30] J. C. Maxwell. On stresses in rarified gases arising from inequalities of temperature. *Philosophical Transactions of the Royal Society of London*, 170:231–256, 1879.

[31] H. Darcy. *Les Fontaines Publiques de la Ville de Dijon: Exposition et Application.* Victor Dalmont, 1856.

[32] S. Whitaker. Flow in porous media I: A theoretical derivation of Darcy's law. *Transport in Porous Media*, 1(1):3–25, 1986.

[33] M. Kaviany. *Principles of Heat Transfer in Porous Media.* Springer, 2012.

[34] J. Kozeny. Über kapillare Leitung des Wassers im Boden. *Sitzungsber Akad. Wiss.*, 136(2a):271–306, 1927.

[35] P. C. Carman. *Flow of Gases Through Porous Media*. Butterworths Scientific Publications, 1956.

[36] L. J. Klinkenberg. The permeability of porous media to liquids and gases. In *Drilling and production practice*, 1941.

[37] J. Fourier. *Theorie Analytique de la Chaleur*. Chez Firmin Didot, père et fils, 1822.

[38] H. D. Baehr and K. Stephan. *Heat and Mass Transfer*. Springer, 2006.

[39] E. H. Kennard. *Kinetic Theory of Gases*. McGraw-Hill, 1938.

[40] VDI-Gesellschaft Verfahrenstechnik und Chemieingenieurwesen. *VDI Heat Atlas*. Springer, 2010.

[41] E. Tsotsas and H. Martin. Thermal conductivity of packed beds: A review. *Chemical Engineering and Processing*, 22(1):19–37, 1987.

[42] W. van Antwerpen, du Toit, C. G., and P. G. Rousseau. A review of correlations to model the packing structure and effective thermal conductivity in packed beds of mono-sized spherical particles. *Nuclear Engineering and Design*, 240(7):1803–1818, 2010.

[43] P. Zehner and E. U. Schlünder. Wärmeleitfähigkeit von Schüttungen bei mäßigen Temperaturen. *Chemie Ingenieur Technik*, 42(14):933–941, 1970.

[44] P. Zehner and E. U. Schlünder. Einfluß der Wärmestrahlung und des Druckes auf den Wärmetransport in nicht durchströmten Schüttungen. *Chemie Ingenieur Technik*, 44(23):1303–1308, 1972.

[45] R. Bauer and E. U. Schlünder. Part I: Effective radial thermal conductivity of packings in gas flow. Part II: Thermal conductivity of the packing fraction without gas flow. *International Chemical Engineering*, 18:189–204, 1978.

[46] A. Dąbrowski. Adsorption—from theory to practice. *Advances in Colloid and Interface Science*, 93(1-3):135–224, 2001.

[47] D. D. Do. *Adsorption Analysis: Equilibria and Kinetics*. World Scientific, 1998.

[48] W. Kast. *Adsorption aus der Gasphase, Ingenieurwissenschaftliche Grundlagen und technische Verfahren*. VCH Verlagsgesellschaft, 1988.

[49] D. M. Ruthven. *Principles of Adsorption and Adsorption Processes*. John Wiley & Sons, 1984.

[50] D. Bathen and M. Breitbach. *Adsorptionstechnik*. Springer, 2013.

[51] B. P. Bering, M. M. Dubinin, and V. V. Serpinsky. Theory of volume filling for vapor adsorption. *Journal of Colloid and Interface Science*, 21(4):378–393, 1966.

[52] J. Kärger and D. M. Ruthven. *Diffusion in Zeolites and Other Microporous Materials*. Wiley, 1992.

[53] E. Glueckauf. Theory of chromatography. Part 10.—Formulæ for diffusion into spheres and their application to chromatography. *Transactions of the Faraday Society*, 51:1540–1551, 1955.

[54] B. N. Okunev, A. P. Gromov, L. I. Heifets, and Y. I. Aristov. A new methodology of studying the dynamics of water sorption/desorption under real operating conditions of adsorption heat pumps: Modelling of coupled heat and mass transfer in a single adsorbent grain. *International Journal of Heat and Mass Transfer*, 51(1-2):246–252, 2008.

[55] S. Sircar and J. R. Hufton. Why does the Linear Driving Force model for adsorption kinetics work? *Adsorption*, 6(2):137–147, 2000.

[56] G. Beckmann and P. V. Gilli. *Thermal Energy Storage: Basics, Design, Applications to Power Generation and Heat Supply*. Springer, Wien, 1984.

[57] J. Xu, R. Z. Wang, and Y. Li. A review of available technologies for seasonal thermal energy storage. *Solar Energy*, 103:610–638, 2014.

[58] A. Solé, I. Martorell, and L. F. Cabeza. State of the art on gas-solid thermochemical energy storage systems and reactors for building applications. *Renewable and Sustainable Energy Reviews*, 47:386–398, 2015.

[59] L. Scapino, H. A. Zondag, J. van Bael, J. Diriken, and C. C. M. Rindt. Sorption heat storage for long-term low-temperature applications: A review on the advancements at material and prototype scale. *Applied Energy*, 190:920–948, 2017.

[60] L. F. Cabeza, A. Solé, and C. Barreneche. Review on sorption materials and technologies for heat pumps and thermal energy storage. *Renewable Energy*, 110:3–39, 2016.

[61] L. Yong and K. Sumathy. Review of mathematical investigation on the closed adsorption heat pump and cooling systems. *Renewable and Sustainable Energy Reviews*, 6(4):305–337, 2002.

[62] A. Pesaran, H. Lee, Y. Hwang, R. Radermacher, and H. H. Chun. Review article: Numerical simulation of adsorption heat pumps. *Energy*, 100:310–320, 2016.

[63] T. Nagel, S. Beckert, C. Lehmann, R. Glaeser, and O. Kolditz. Multi-physical continuum models of thermochemical heat storage and transformation in porous media and powder beds-A review. *Applied Energy*, 178:323–345, 2016.

[64] M. S. Fernandes, G. J. V. N. Brites, J. J. Costa, A. R. Gaspar, and V. A. F. Costa. Modeling and parametric analysis of an adsorber unit for thermal energy storage. *Energy*, 102:83–94, 2016.

[65] H. Schreiber, S. Graf, F. Lanzerath, and A. Bardow. Adsorption thermal energy storage for cogeneration in industrial batch processes: Experiment, dynamic modeling and system analysis. *Applied Thermal Engineering*, 89:485–493, 2015.

[66] T. A. Fuller, W. J. Wepfer, S. V. Shelton, and M. W. Ellis. A two-temperature model of the regenerative solid-vapor heat pump. *Journal of Energy Resources Technology*, 116(4):297–304, 1994.

[67] L. M. Sun, N. B. Amar, and F. Meunier. Numerical study on coupled heat and mass transfers in an absorber with external fluid heating. *Heat Recovery Systems and CHP*, 15(1):19–29, 1995.

[68] A. Assefa. Analysis of combined heat and mass transfer of water-vapor in a cylinderical zeolite adsorber. *Zede Journal*, 16:67–75, 1999.

[69] K. C. Leong and Y. Liu. Numerical study of a combined heat and mass recovery adsorption cooling cycle. *International Journal of Heat and Mass Transfer*, 47(22):4761–4770, 2004.

[70] H. Demir, M. Mobedi, and S. Ülkü. Effects of porosity on heat and mass transfer in a granular adsorbent bed. *International Communications in Heat and Mass Transfer*, 36(4):372–377, 2009.

[71] I. Solmus, D. A. S. Rees, C. Yamali, and D. Baker. A two-energy equation model for dynamic heat and mass transfer in an adsorbent bed using silica gel/water pair. *International Journal of Heat and Mass Transfer*, 55(19-20):5275–5288, 2012.

[72] M. Duquesne, J. Toutain, A. Sempey, S. Ginestet, and E. Palomo del Barrio. Modeling of a nonlinear thermochemical energy storage by adsorption on zeolites. *Applied Thermal Engineering*, 71(1):469–480, 2014.

[73] A. I. Radu, T. Defraeye, P. Ruch, J. Carmeliet, and D. Derome. Insights from modeling dynamics of water sorption in spherical particles for adsorption heat pumps. *International Journal of Heat and Mass Transfer*, 105:326–337, 2017.

[74] G. G. Ilis, M. Mobedi, and S. Ülkü. Comparison of uniform and non-uniform pressure approaches used to analyze an adsorption process in a closed type adsorbent bed. *Transport in Porous Media*, 98(1):81–101, 2013.

[75] L. Yong and K. Sumathy. Comparison between heat transfer and heat mass transfer models for transportation process in an adsorbent bed. *International Journal of Heat and Mass Transfer*, 47(8-9):1587–1598, 2004.

[76] J. Jaenchen, T. H. Herzog, K. Gleichmann, B. Unger, A. Brandt, G. Fischer, and H. Richter. Performance of an open thermal adsorption storage system with Linde type A zeolites: Beads versus honeycombs. *Microporous and Mesoporous Materials*, 207:179–184, 2015.

[77] H. Liu and K. Nagano. Numerical simulation of an open sorption thermal energy storage system using composite sorbents built into a honeycomb structure. *International Journal of Heat and Mass Transfer*, 78:648–661, 2014.

[78] F. B. Cortés, F. Chejne, F. Carrasco-Marín, C. Moreno-Castilla, and A. F. Pérez-Cadenas. Water adsorption on zeolite 13X: comparison of the two methods based on mass spectrometry and thermogravimetry. *Adsorption*, 16(3):141–146, 2010.

[79] S. Semprini, C. Lehmann, S. Beckert, O. Kolditz, R. Glaeser, H. Kerskes, and T. Nagel. Numerical modelling of water sorption isotherms of zeolite 13XBF based on sparse experimental data sets for heat storage applications. *Energy Conversion and Management*, 150:392–402, 2017.

[80] K. Schumann, B. Unger, A. Brandt, and F. Scheffler. Investigation on the pore structure of binderless zeolite 13x shapes. *Microporous and Mesoporous Materials*, 154:119–123, 2012.

[81] J. Jaenchen, K. Schumann, E. Thrun, A. Brandt, B. Unger, and U. Hellwig. Preparation, hydrothermal stability and thermal adsorption storage properties of binderless zeolite beads. *International Journal of Low-Carbon Technologies*, 2012.

[82] G. E. Karniadakis, A. Beskoek, and N. R. Aluru. *Microflows and Nanoflows: Fundamentals and Simulation*. Springer, 2005.

[83] M. Knudsen. Die Gesetze der Molekularströmung und der inneren Reibungsströmung der Gase durch Röhren. *Annalen der Physik*, 333(1):75–130, 1909.

[84] S. Colin. Rarefaction and compressibility effects on steady and transient gas flows in microchannels. *Microfluidics and Nanofluidics*, 1(3):268–279, 2005.

[85] B. T. Porodnov and F. T. Tukhvetov. Theoretical investigation of nonisothermal flow of a rarefied gas in a cylindrical capillary. *Journal of Engineering Physics*, 36(1):61–66, 1979.

[86] G. A. Bird. *The DSMC method*. CreateSpace Independent Publishing Platform, 2013.

[87] S. K. Loyalka and S. A. Hamoodi. Poiseuille flow of a rarefied gas in a cylindrical tube: solution of linearized Boltzmann equation. *Physics of Fluids A: Fluid Dynamics*, 2(11):2061–2065, 1990.

[88] F. Sharipov. Rarefied gas flow through a long rectangular channel. *Journal of Vacuum Science and Technology A*, 17(5):3062–3066, 1999.

[89] I. A. Graur and F. Sharipov. Non-isothermal flow of rarefied gas through a long pipe with elliptic cross section. *Microfluidics and Nanofluidics*, 6(2):267–275, 2009.

[90] P. Perrier, I. A. Graur, T. Ewart, and J. G. Meolans. Mass flow rate measurements in microtubes: From hydrodynamic to near free molecular regime. *Physics of Fluids*, 23(4), 2011.

[91] T. Ewart, P. Perrier, I. A. Graur, and J. G. Meolans. Mass flow rate measurements in a microchannel, from hydrodynamic to near free molecular regimes. *Journal of Fluid Mechanics*, 584:337–356, 2007.

[92] F. Sharipov and I. A. Graur. General approach to transient flows of rarefied gases through long capillaries. *Vacuum*, 100:22–25, 2014.

[93] L. Wang, S. Wang, R. Zhang, C. Wang, Y. Xiong, X. Zheng, S. Li, K. Jin, and Z. Rui. Review of multi-scale and multi-physical simulation technologies for shale and tight gas reservoirs. *Journal of Natural Gas Science and Engineering*, 37:560–578, 2017.

[94] K. Hooman, A. Tamayol, M. Dahari, M. R. Safaei, H. Togun, and R. Sadri. A theoretical model to predict gas permeability for slip flow through a porous medium. *Applied Thermal Engineering*, 70(1):71–76, 2014.

[95] F. Civan. Effective correlation of apparent gas permeability in tight porous media. *Transport in Porous Media*, 82(2):375–384, 2010.

[96] A. S. Ziarani and R. Aguilera. Knudsen's permeability correction for tight porous media. *Transport in Porous Media*, 91(1):239–260, 2012.

[97] S. Colin. Gas microflows in the slip flow regime: A critical review on convective heat transfer. *Journal of Heat Transfer-Transactions of the ASME*, 134(2), 2012.

[98] R. E. Hayes, A. Rojas, and J. Mmbaga. The effective thermal conductivity of monolith honeycomb structures. *Catalysis Today*, 147:S113 – S119, 2009.

[99] Y. Ogniewicz and M. Yovanovich. Effective conductivity of regularly packed spheres - basic cell model with constriction. In *15th Aerospace Sciences Meeting*, Reston, Virigina, 1977. American Institute of Aeronautics and Astronautics.

[100] C. T. Hsu, P. Cheng, and K. W. Wong. Modified Zehner-Schlunder models for stagnant thermal conductivity of porous media. *International Journal of Heat and Mass Transfer*, 37(17):2751–2759, 1994.

[101] M. Moscardini, Y. Gan, S. Pupeschi, and M. Kamlah. Discrete element method for effective thermal conductivity of packed pebbles accounting for the Smoluchowski effect. *Fusion Engineering and Design*, 127:192–201, 2018.

[102] J. Grobbel, S. Brendelberger, C. Sattler, and R. Pitz-Paal. Heat transfer in a directly irradiated ceria particle bed under vacuum conditions. *Solar Energy*, 158:737–745, 2017.

[103] M. Rouhani and M. Bahrami. Effective thermal conductivity of packed bed adsorbers: Part 2 - Theoretical model. *International Journal of Heat and Mass Transfer*, 123:1212–1220, 2018.

[104] M. Bahrami, M. Yovanovich, and J. R. Culham. Effective thermal conductivity of rough spherical packed beds. *International Journal of Heat and Mass Transfer*, 49(19-20):3691–3701, 2006.

[105] B. Dawoud, M. I. Sohel, A. Freni, S. Vasta, and G. Restuccia. On the effective thermal conductivity of wetted zeolite under the working conditions of an adsorption chiller. *Applied Thermal Engineering*, 31(14):2241–2246, 2011.

[106] E. Tsotsas and E. U. Schlünder. Contact drying of mechanically agitated particulate material in the presence of inert gas. *Chemical Engineering and Processing*, 20(5):277–285, 1986.

[107] M. Schaefer and A. Thess. One-dimensional model of a closed low-pressure adsorber for thermal energy storage. *International Journal of Heat and Mass Transfer*, 117:571–583, 2018.

[108] M. Schaefer and A. Thess. Simulation of a closed low-pressure honeycomb adsorber for thermal energy storage. *International Journal of Heat and Mass Transfer*, 126:796–807, 2018.

[109] M. Schaefer and A. Thess. Modeling and simulation of closed low-pressure zeolite adsorbers for thermal energy storage. *International Journal of Heat and Mass Transfer*, 139:685–699, 2019.

[110] A. Patton, B. D. Crittenden, and S. P. Perera. Use of the linear driving force approximation to guide the design of monolithic adsorbents. *Chemical Engineering Research and Design*, 82(A8):999–1009, 2004.

[111] Z. Y. Liu, G. Cacciola, G. Restuccia, and N. Giordano. Fast simple and accurate measurement of zeolite thermal conductivity. *Zeolites*, 10(6):565–570, 1990.

[112] VDI-Gesellschaft Verfahrenstechnik und Chemieingenieurwesen. *VDI Heat Atlas (German Edition)*. Springer, 2006.

[113] V. Vučelić and D. Vučelić. Heat capacities of water on zeolites. *Studies in Surface Science and Catalysis*, 24:475–480, 1985.

[114] I. A. Graur and M. T. Ho. Rarefied gas flow through a long rectangular channel of variable cross section. *Vacuum*, 101:328–332, 2014.

[115] R. J. LeVeque. *Finite difference methods for ordinary and partial differential equations: Steady-state and time-dependent problems*, volume 98. Siam, 2007.

[116] K. Ogata and Y. Yang. *Modern Control Engineering*. India: Prentice Hall, 2002.

[117] A. C. Griesinger, K. Spindler, and E. Hahne. Measurements and theoretical modelling of the effective thermal conductivity of zeolites. *International Journal of Heat and Mass Transfer*, 42(23):4363–4374, 1999.

[118] A. C. Griesinger. *Experimentelle und theoretische Untersuchung des Wärmetransports in Zeolithschüttungen*. Dissertation, Medien-Verlag Köhler, 1997.

[119] T. Ewart, P. Perrier, I. A. Graur, and J. G. Meolans. Mass flow rate measurements in gas micro flows. *Experiments in Fluids*, 41(3):487–498, 2006.

[120] E. Afrasiabian, L. Marino, and C. M. Casciola. Experimental analysis of the non isothermal rarefied gas flow through a packed bed of spheres. *International Journal of Heat and Mass Transfer*, 66(0):791–797, 2013.

[121] M. Schäfer. *Computational Engineering - Introduction to Numerical Methods*. Springer, 2006.

[122] J. D. Lambert. *Numerical Methods for Ordinary Differential Systems: The Initial Value Problem*. John Wiley & Sons, 1991.

[123] L. F. Shampine and M. W. Reichelt. The MATLAB ODE suite. *Siam Journal on Scientific Computing*, 18(1):1–22, 1997.

[124] J. Ullmann. Transient simulation of vacuum flat collector with TRNSYS. *Personal communication*, 2018.

A. Model Description

A.1. Adsorption Mass Sink

To determine the volumetric adsorption mass sink term $\sigma_{m,\mathrm{v,z}}$, the definition of the water uptake given by Eq. (2.38) is differentiated with respect to time. This gives

$$\frac{\partial X}{\partial t} = \frac{1}{M_\mathrm{z}} \frac{\partial M_\mathrm{a}}{\partial t}. \tag{A.1}$$

Considering

$$\frac{\partial M_\mathrm{a}}{\partial t} = \sigma_{m,\mathrm{v,z}} V \tag{A.2}$$

and

$$M_\mathrm{z} = (1-\varepsilon)\rho_\mathrm{z} V \tag{A.3}$$

yields the result

$$\sigma_{m,\mathrm{v,z}} = (1-\varepsilon)\rho_\mathrm{z} \frac{\partial X}{\partial t}. \tag{A.4}$$

A.2. Vapor Accumulation in Adsorbent

To prove that the vapor accumulation in the zeolite adsorbent is negligible, the product rule is applied to the related term in Eq. (4.11). With the Eq. (4.38) for the uptake dependent inner porosity $\varepsilon_\mathrm{z}(X)$ of the zeolite adsorbent, this yields

$$\frac{\partial}{\partial t}\left(\varepsilon_\mathrm{z}\left(X\right)\bar{\rho}_\mathrm{v,z}\right) \approx -\bar{\rho}_\mathrm{v,z}\frac{\rho_\mathrm{z}}{\rho_\mathrm{a}}\frac{\partial X}{\partial t} + \varepsilon_\mathrm{z}\left(X\right)\frac{\partial \bar{\rho}_\mathrm{v,z}}{\partial t}. \tag{A.5}$$

Due to the low pressure, the vapor density is very low ($\bar{\rho}_\mathrm{v,z} \leq 10^{-2}\,\mathrm{kg/m^3}$) compared to the density of the zeolite adsorbent ($\rho_\mathrm{z} = 1150\,\mathrm{kg/m^3}$). Thus,

$$\left|-\bar{\rho}_\mathrm{v,z}\frac{\rho_\mathrm{z}}{\rho_\mathrm{a}}\frac{\partial X}{\partial t}\right| \ll \left|\rho_\mathrm{z}\frac{\partial X}{\partial t}\right| \tag{A.6}$$

is true and the first term on the right side of Eq. (A.5) is proved negligible.

Regarding the second term on the right side of Eq. (A.5), it is not possible to prove analytically that the term is negligible. That is, it is not possible to show that

$$\left|(1-\varepsilon)\varepsilon_\mathrm{z}\left(X\right)\frac{\partial \bar{\rho}_\mathrm{v,z}}{\partial t}\right| \ll \left|\varepsilon\frac{\partial \rho_\mathrm{v}}{\partial t}\right| \tag{A.7}$$

is true. However, it is possible to verify by means of numerical simulations that the second term on the right side of Eq. (A.5) can be omitted as well. As an example, the specific thermal power $p_\mathrm{th,htx}$ versus the non-dimensional time $\tilde{t}$ for the reference case studied by the SCM (see Tab. 6.1) is computed with and without consideration of the vapor accumulation in the zeolite adsorbent. The results are shown in Fig. A.1. The figure confirms that the results are identical, and thus the vapor accumulation in the zeolite adsorbent is negligible.

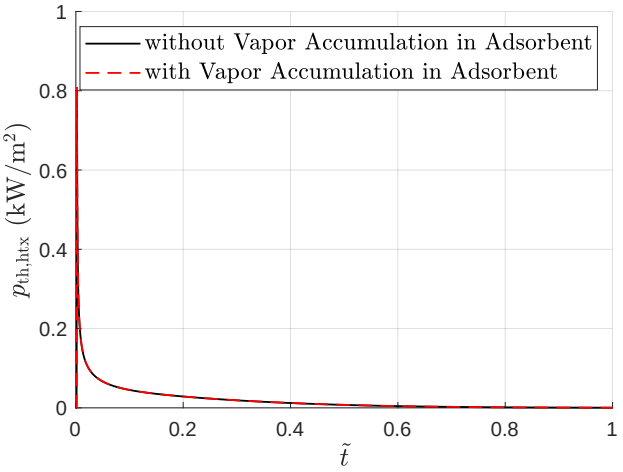

Figure A.1.: Specific thermal power at the heat exchanger $p_{\mathrm{th,htx}}$ versus non-dimensional time $\tilde{t}$.

A.3. Internal Energy of Adsorbate

To derive Eq. (4.15) for the internal energy of the adsorbate e_{a}, the definition of the adsorption enthalpy Δh_{a} is applied

$$\Delta h_{\mathrm{a}} = h_{\mathrm{v}} - h_{\mathrm{a}}, \tag{A.8}$$

where h_{v} and h_{a} denote the enthalpy of the vapor and adsorbate. Substituting the enthalpies by their definitions with the internal energy

$$h_{\mathrm{v}} = e_{\mathrm{v}} + p v_{\mathrm{v}}, \tag{A.9}$$
$$h_{\mathrm{a}} = e_{\mathrm{a}} + p v_{\mathrm{a}}, \tag{A.10}$$

yields

$$e_{\mathrm{a}} = e_{\mathrm{v}} + p\,(v_{\mathrm{v}} - v_{\mathrm{a}}) - \Delta h_{\mathrm{a}}. \tag{A.11}$$

Considering that the specific volume of the vapor is higher by several orders of magnitude compared to the specific volume of the adsorbate, that is

$$v_{\mathrm{v}} \gg v_{\mathrm{a}}, \tag{A.12}$$

and taking the ideal gas law

$$p v_{\mathrm{v}} = R_{\mathrm{s}} T \tag{A.13}$$

into account, the required equation is derived

$$e_{\mathrm{a}} = e_{\mathrm{v}} + R_{\mathrm{s}} T - \Delta h_{\mathrm{a}}. \tag{A.14}$$

A.4. Adsorption in Rectangular Channels

To confirm the validity of the transformation Eq. (4.52) for rectangular channels, the kinetics parameter k_a is calculated with Eq. (4.35) for different aspect ratios of channel width to channel height b/a. The result is shown in Fig. A.2. The figure shows that the kinetics parameter converges to the value of the kinetics parameter for adsorption into a plane adsorbent sheet. This confirms the validity of the approach also for rectangular channels of higher aspect ratios b/a.

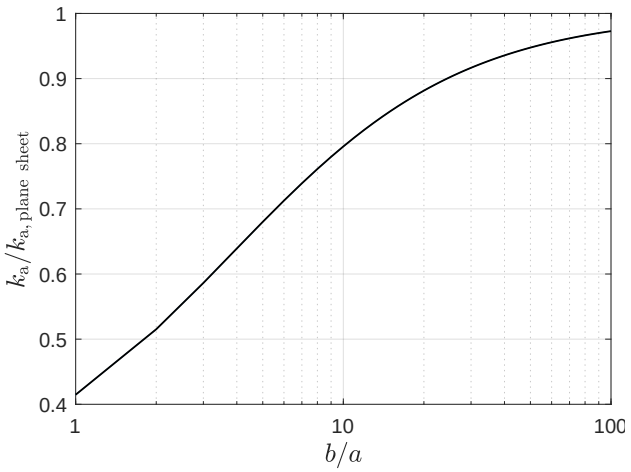

Figure A.2.: Ratio of adsorption kinetics parameter $k_\mathrm{a}/k_{\mathrm{a,plane\,sheet}}$ for rectangular adsorbent channels versus the aspect ratio of channel width to channel height b/a.

B. Model Parameters

Constant Parameters

The parameters related to the adsorption are mostly taken from [16].

Latin Letters		Value	Unit
$c_{a,min}$	minimum of the specific heat capacity of the adsorbate at the temperature T_{min} in Eq. (4.37)	836	J/kg K
c_z	specific heat capacity of dry zeolite adsorbent	880	J/kg K
C	empirical factor for thermal accommodation coefficient α_T of vapor in Eq. (2.35)	3.6	-
d_{mp}	mean macro pore diameter of zeolite adsorbent	300 e−9	m
E_a	characteristic energy of adsorption in Eq. (4.32)	1.19225 e6	J/kg
Δh_e	enthalpy of vaporization of the adsorbate (water)	2.445 e6	J/kg
$K_{I,1}$	controller parameter of power and temperature control in Eq.(4.53) and (4.78)	1 e−4	1/s
$K_{I,2}$	controller parameter of power control in Eq.(4.53)	1 e−1	m^3Pa/W s
$K_{I,2}$	controller parameter of temp. control in Eq. (4.78)	1 e−1	Pa/K s
n_a	heterogeneity parameter of adsorption in Eq. (4.32)	1.55	-
R_s	specific gas constant of vapor	461.4	J/kg K
T_{min}	minimum reference temperature for specific heat capacity of the adsorbate in Eq. (4.37)	210	K
T_{ref}	minimum reference temperature for specific heat capacity of the adsorbate in Eq. (4.37)	335	K
$v_{a,max}$	max. specific volume of the adsorbate in Eq. (4.32)	341.03 e−6	m^3/kg

Greek Letters		Value	Unit
α_1	fitting parameter for specific heat capacity of the adsorbate in Eq. (4.37)	37.6	J/kg K
α_2	fitting parameter for specific heat capacity of the adsorbate in Eq. (4.37)	3.976 e−4	$1/K^2$
α_p	empirical weighing factor for effective heat conductivity of zeolite 13X granules in Eq. (4.30)	0.227	-
α_p	empirical weighing factor for eff. heat conductivity of zeolite 13X honeycomb with PTFE in Eq. (4.30)	0.734	-
β_a	thermal expansion coeff. of adsorbate in Eq. (4.33)	0.2066 e−3	1/K
$\varepsilon_{z,max}$	maximum inner porosity of the fully desorbed dry zeolite adsorbent in Eq. (4.38)	0.6	m^3/m^3
ϵ	radiation emission coeff. for zeolite in Eq. (4.74)	0.89	-
λ_z	heat conductivity of pure zeolite crystal	1	W/m K
$\rho_{a,20°C}$	density of the adsorbate at 20°C in Eq. (4.33)	998.21	kg/m^3
ρ_z	density of dry zeolite adsorbent including inner pores	1150	kg/m^3
τ_z	inner tortuosity of the zeolite adsorbent in Eq. (4.36)	4	-
φ	fitting parameter for the finite contact area of the particles in Eq. (4.74)	0.0035	-

Temperature-dependent Parameters

The temperature-dependent parameters listed below are calculated by polynomial correlation functions given in the VDI Heat Atlas [112]. With respect to the effective heat conductivity of packed beds (granules and powder adsorbent), the ZBS model is applied as described in [40].

Latin Letters		**Unit**
c_{htf}	specific heat capacity of heat transfer fluid (water) $c_{\mathrm{htf}} = A + B\,T + C\,T^2 + D\,T^3 + E/T^2$ $A = 3092$, $B = 12.328$, $C = -0.044504$, $D = 0.005226\,\mathrm{e}{-2}$, $E = 0$	J/kg K
$c_{p,\mathrm{v}}$	specific heat capacity at constant pressure of vapor $c_{p,\mathrm{v}} = A + B\,T + C\,T^2 + D\,T^3 + E/T^2$ $A = 1833.10$, $B = -0.035$, $C = 0.000696$, $D = -0.000215\,\mathrm{e}{-3}$, $E = -0.000026\,\mathrm{e}{-3}$	J/kg K
p_{sat}	saturation pressure of vapor $p_{\mathrm{sat}} = p_{\mathrm{crit}}\,\exp\left(T_{\mathrm{crit}}/T\,\left(A\,k + B\,k^{1.5} + C\,k^3 + D\,k^6\right)\right)$ $k = 1 - T/T_{\mathrm{crit}}$ $p_{\mathrm{crit}} = 220.64\,\mathrm{e}5$ Pa, $T_{\mathrm{crit}} = 647.096$ K $A = -7.71374$, $B = 1.31467$, $C = -2.51444$, $D = -1.72542$	Pa

Greek Letters		**Unit**
α_{htf}	heat transfer coefficient of heat transfer fluid $\alpha_{\mathrm{htf}} = \overline{Nu}\dfrac{\lambda_{\mathrm{htf}}}{2h_{\mathrm{htx}}}$, $\overline{Nu} = \sqrt[3]{Nu_1^3 + Nu_2^3 + Nu_3^3}$ $Nu_1 = 7.541$, $Nu_2 = 1.841\sqrt[3]{\zeta}$, $Nu_3 = \sqrt[6]{\dfrac{2}{1+22Pr}}\sqrt{\zeta}$, $\zeta = Re\,Pr\dfrac{2h_{\mathrm{htx}}}{z}$, $Re = \dfrac{\rho_{\mathrm{htf}}u_{\mathrm{htf}}h_{\mathrm{htx}}}{\mu_{\mathrm{htf}}}$, $Pr = \dfrac{\mu_{\mathrm{htf}}c_{\mathrm{htf}}}{\lambda_{\mathrm{htf}}}$	W/m^{2}K
λ_{a}, λ_{htf}	heat conductivity of adsorbate and heat transfer fluid (water) $\lambda_{\mathrm{a/htf}} = A + B\,T + C\,T^2 + D\,T^3 + E\,T^4$ $A = -0.3623$, $B = 0.50659\,\mathrm{e}{-2}$, $C = -0.05805\,\mathrm{e}{-4}$, $D = -0.01527\,\mathrm{e}{-7}$, $E = 0.01847\,\mathrm{e}{-10}$	W/m K
$\lambda_{\mathrm{v},0}$	heat conductivity of vapor in continuum regime $\lambda_{\mathrm{v},0} = A + B\,T + C\,T^2$ $A = 0.46\,\mathrm{e}{-3}$, $B = 0.046\,\mathrm{e}{-3}$, $C = 0.051150\,\mathrm{e}{-6}$	W/m K
μ	shear viscosity of vapor $\mu = A + B\,T + C\,T^2$ $A = -0.10718\,\mathrm{e}{-5}$, $B = 0.35248\,\mathrm{e}{-7}$, $C = 0.03575\,\mathrm{e}{-10}$	Pa s
μ_{htf}	shear viscosity of heat transfer fluid (water) $\mu_{\mathrm{htf}} = \exp\left(A + B/T + C\,T + D\,T^2 + E\,T^3\right)$ $A = -22.968$, $B = 3275.89$, $C = 0.017637$, $D = 0.000693\,\mathrm{e}{-3}$, $E = -0.012933\,\mathrm{e}{-6}$	Pa s
ρ_{htf}	density of heat transfer fluid (water) $\rho_{\mathrm{htf}} = A\left(B^{1+(1-T/C)\hat{}D}\right)^{-1}$ $A = 1.5053957$, $B = 0.03642$, $C = 617.774$, $D = 0.05871$	kg/m^3

C. Mesh Convergence

Multi Channel Model (MCM)

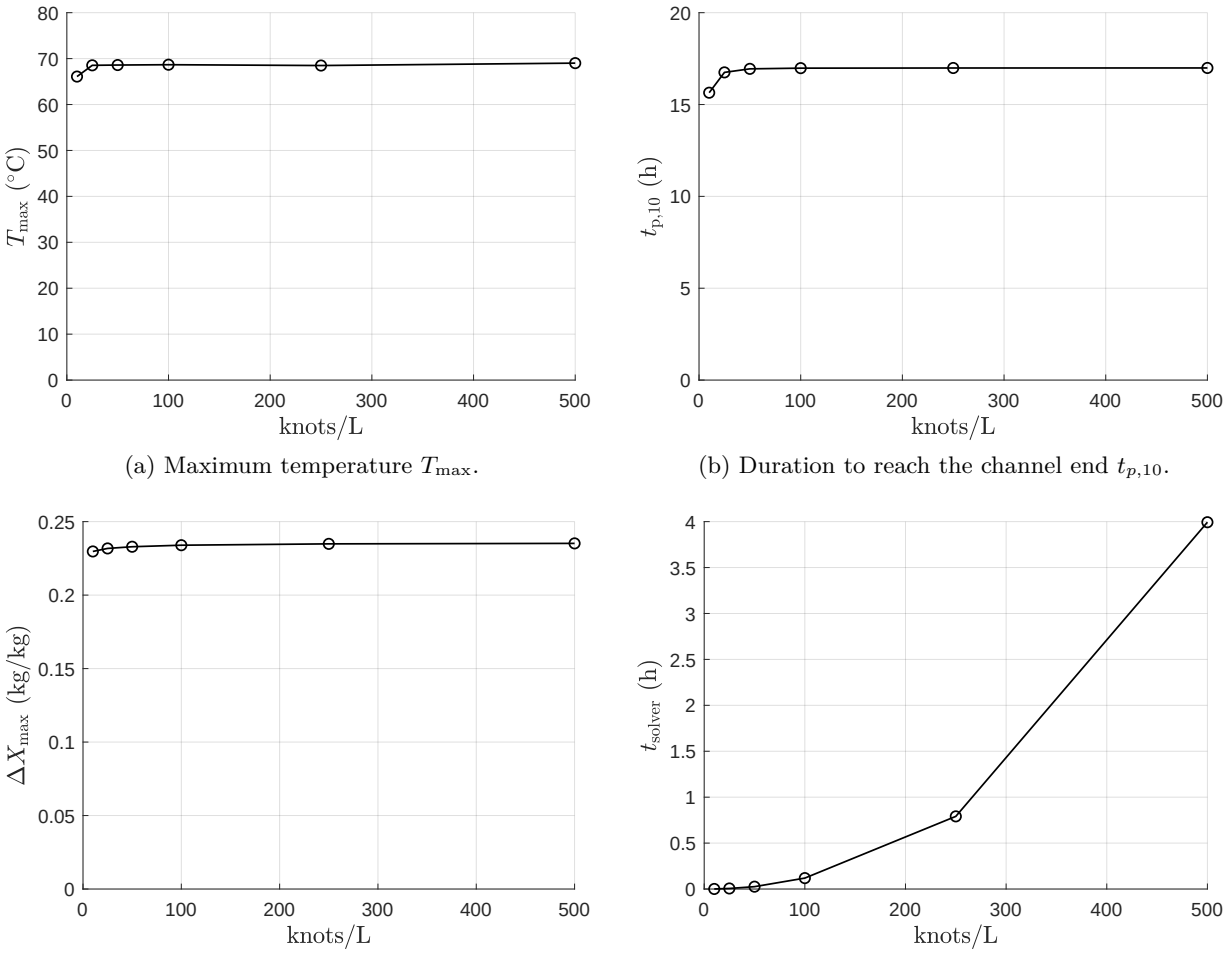

(a) Maximum temperature $T_{\max}$.

(b) Duration to reach the channel end $t_{p,10}$.

(c) Maximum variation of the water uptake $\Delta X_{\max}$.

(d) Solver duration t_{solver}.

Figure C.1.: Dependency of the maximum temperature $T_{\max}$, the time required for the vapor to reach the closed end of the adsorber $t_{p,10}$, the maximum variation of the water uptake $\Delta X_{\max}$ in the adsorber and the solver duration t_{solver} on the number of knots per length $N_z = \text{knots}/L$ for the reference case of the MCM, see Tab. 6.2 .

General Continuum Model (GCM)

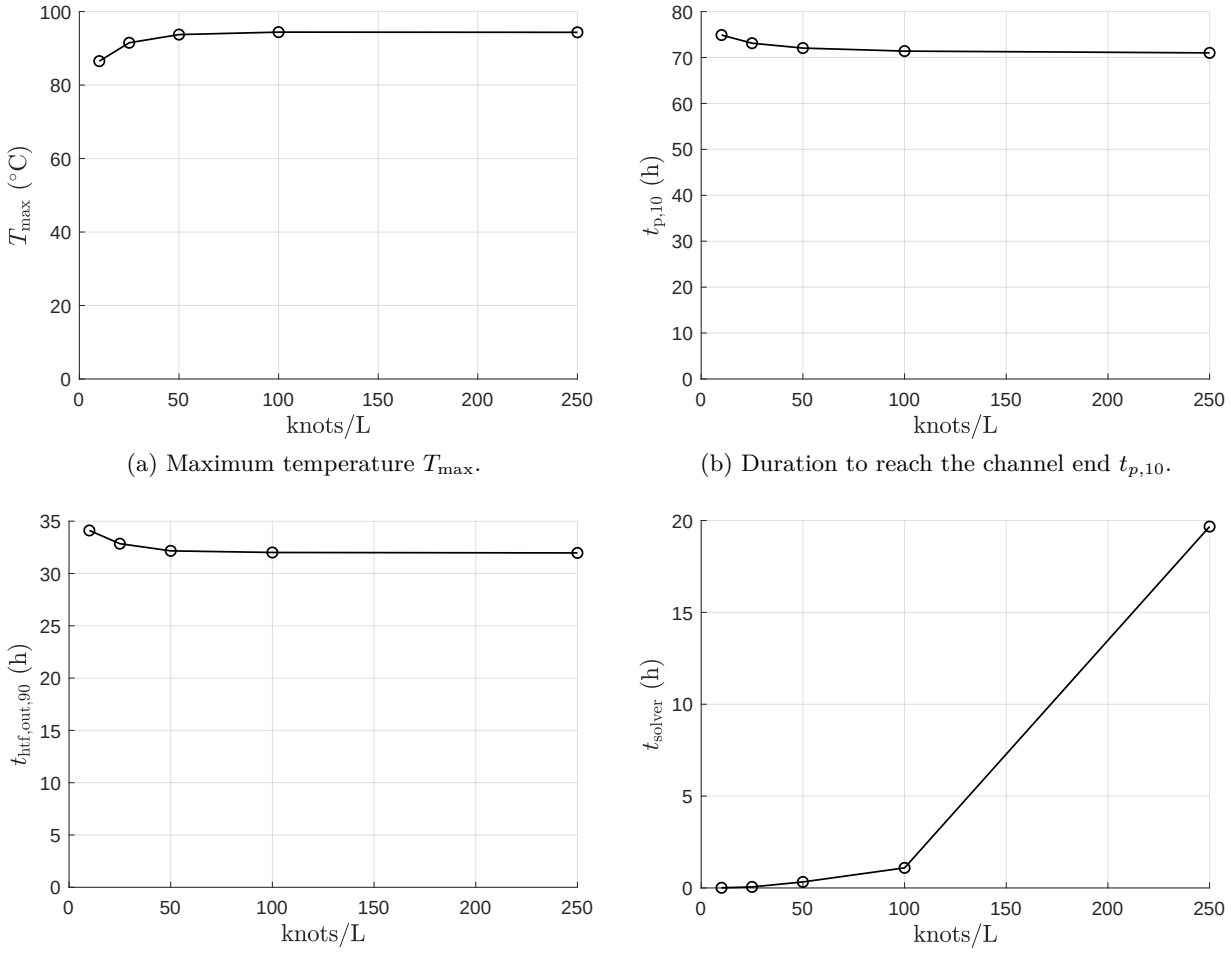

(a) Maximum temperature $T_{\max}$.

(b) Duration to reach the channel end $t_{p,10}$.

(c) Duration for cool-down of heat transfer fluid $t_{\mathrm{htf,out,90}}$.

(d) Solver duration t_{solver}.

Figure C.2.: Dependency of the maximum temperature $T_{\max}$, the time required for the vapor to reach the closed end of the adsorber $t_{p,10}$, the time required for the heat transfer fluid to cool down to 90% of the set discharging temperature $t_{\mathrm{htf,out,90}}$ and the solver duration t_{solver} on the number of knots per length $N_z = \mathrm{knots}/L$ for the reference case of the GCM, see Tab. 6.3 .

General Continuum Model (GCM)

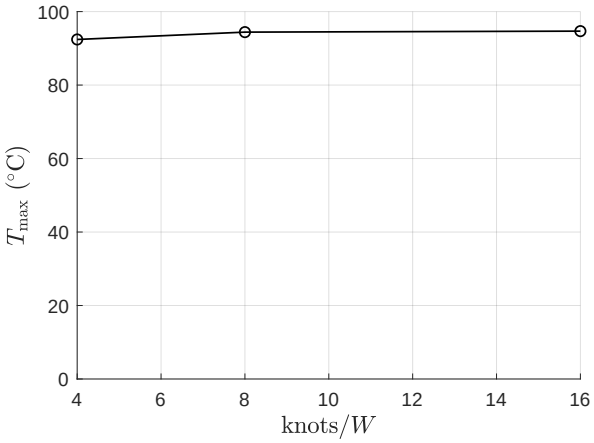

(a) Maximum temperature $T_{\max}$.

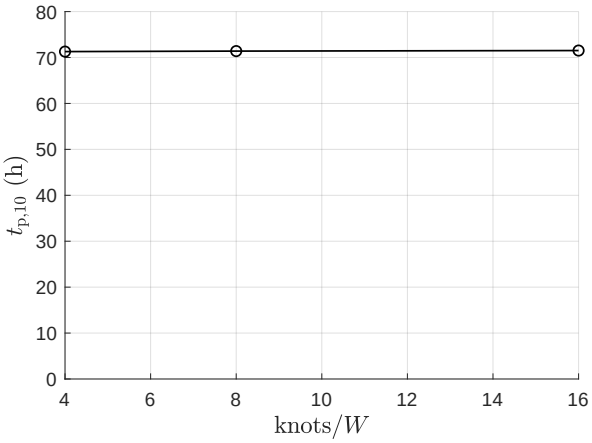

(b) Duration to reach the channel end $t_{p,10}$.

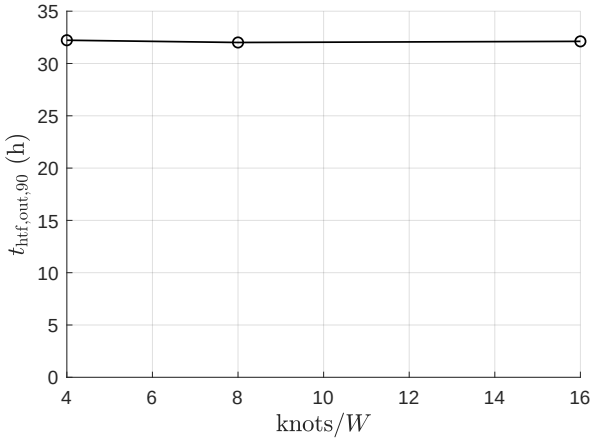

(c) Duration for cool-down of heat transfer fluid $t_{\text{htf,out,90}}$.

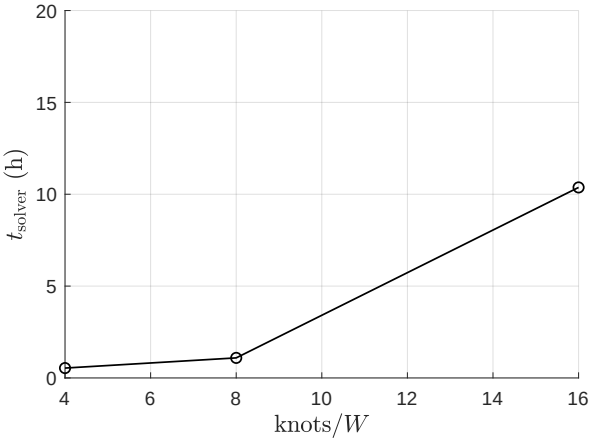

(d) Solver duration t_{solver}.

Figure C.3.: Dependency of the maximum temperature $T_{\max}$, the time required for the vapor to reach the closed end of the adsorber $t_{p,10}$, the time required for the heat transfer fluid to cool down to 90% of the set discharging temperature $t_{\text{htf,out,90}}$ and the solver duration t_{solver} on the transversal number of knots per width $N_x = \text{knots}/W$ for the reference case of the GCM, see Tab. 6.3 .